The Dissertation Committee for Lingcheng Li Certifies that this is the approved version of the following Dissertation:

Multi-Scale Understanding and Modeling of Plant Hydraulics

Committee:

Zong-Liang Yang, Supervisor

Ashley Michelle Matheny, Co-Supervisor

Bridget R. Scanlon

Meinhard Bayani Cardenas

Jiafu Mao

Multi-Scale Understanding and Modeling of Plant Hydraulics

by

Lingcheng Li

Dissertation

Presented to the Faculty of the Graduate School of

The University of Texas at Austin

in Partial Fulfillment

of the Requirements

for the Degree of

Doctor of Philosophy

The University of Texas at Austin

August 2020

Dedication

This dissertation is dedicated to my parents, my sister and brother

who gave me endless love, constant encouragement and unwavering support

Acknowledgements

Upon this important milestone in my life, I would like to express my sincere thanks to a number of people who accompanied me during my memorable Ph.D. journey.

First and foremost, I must thank my supervisor Dr. Zong-Liang Yang, who made this journey possible. He was knowledgeable, patient, kind, and helpful to supervise me during the past five years. He gave me freedom and support to explore what I liked in the beginning years. We had many in-depth discussions on broad research topics, scientific methods, critical thinking, etc. To expand my research views, he helped me to establish collaborative relationships with scientists from other institutes over summers. Besides all this, he gave me valuable suggestions about various personal matters in my life. I was fortunate to meet such a fantastic Ph.D. advisor.

I want to thank Dr. Ashley M. Matheny. Even before she joined UT Austin as an assistant professor, she started to give me valuable research suggestions. After she became my co-supervisor, we worked closely to move my research forward. She was always helpful and energetic in quick response to my research questions. She was also like a friend to help relieve the pressure during this journey. I am so happy to have had such a cool advisor and feel proud to become her first Ph.D. student.

I want to thank Dr. Jiafu Mao. I first met Dr. Mao during the 2016 AGU meeting. I then visited the Oak Ridge National Laboratory and worked with him during the summers in 2017 and 2018. These two periods were among the best times of my Ph. D. journey, not just because of Tennessee's cool summer. Dr. Mao is always energetic and productive to

work with. He was very helpful and patient to guide me into new research fields, and always quickly gave me help when I had research questions. I was delighted and greatly benefitted from working with him.

I want to thank my committee members, Dr. M. Bayani Cardenas and Dr. Bridget R. Scanlon. During Bayani's course, besides his lucid explanations of the fundamental concepts and equations, he also stimulated me to think about "hypothesis, critical thinking, and scientific thoughts." He is always very kind to give me suggestions on my research during our discussions. Bridget was always energetic, could quickly grasp my research content, and gave many beneficial comments. She was strict with scientific research, but also very kind with a "big smile" to guide and encourage me from my Ph.D. qualifying exam to defense. In the future, I wish to have more collaborations with them and learn more from them.

I want to thank the scientists from the National Center for Atmospheric Research, Dr. Sean Swenson, Dr. David Lawrence, Dr. Michael Barlage, and Dr. Gordon Bonan. I visited NCAR during the 2019 summer. Sean, David, and Mike took their time to give me useful suggestions for my model development and evaluation. Gordon also gave me lots of insightful suggestions during our discussion to guide my research.

I want to thank all members of the Land Environment and Atmospheric Dynamics (LEAD) group at UT. I benefited greatly from discussions with previous group members, including Dr. Peirong Lin & Dr. Kai Zhang, Dr. Hui Zheng, Dr. Long Zhao, Dr. Jiangfeng Wei, Dr. Armaghan Abed Elmdoust, Dr. Maryia Halubok, Dr. Binyan Yan, Dr. Jingjing Liang, Dr. Qinyun Bian, and more. I would also thank the visiting scholars, including Dr.

Xiaofeng Li, Dr. Jianguo Liu, Dr. Yonghe Liu, Dr. Chunlin Huang, Dr. Bolun Li, Dr. Fang Wang, Dr. Ye Tian, Dr. Mengjie Jin, De Xing, and more. Current group members are also greatly appreciated, including Wen-Ying Wu, Seungwon Chung, Samuel Fung, Sabiha Tabassum, Wei Hu, Dr. Weijing Chen, Wenli Fei, and Mengyao Guo. I want to thank Dr. David Arctur, a very kind and generous person who was always there to help me.

I want to thank Matheny's group, Ana María Restrepo Acevedo, Suvan A. Cabraal, and Austin F. Rechner, for their help.

I want to thank Dr. Robert E. Dickinson, for all the advice he provided for my research work. He was very kind and quickly pointed out the critical points in my model development. I also want to thank Dr. Rong Fu and Dr. Muhammad Shaikh for their help.

I want to thank the Jackson School of Geoscience and the capable staff members. JSG provided enough funding to support my Ph.D. research. Philip A. Guerrero has always been responsive in solving my problems. Adam Papendieck helped me a lot with my English writing. I want to thank Dr. Kerry Cook and Dr. Ginny Catania, and I learned a lot from their courses.

I want to thank the friends I met during my UT time, Dr. Xian Wu, Dr. Xing Zheng, Xiwei Guo, Dr. Weiran Liu, Dr. Xiaolei Peng, Dr. Suyu Fu, Dr. Li Liu, Chijun Sun, Tiannong Dong, Wei Wei, Pingping Wang, and more. I want to thank friends that I met at the 2016 Summer Institute of the National Flood Interoperability Experiment (NFIE) at the National Water Center (NWC), Jiaqi Zhang, Ryan McGehee, and more. I want to thank the

friends I met at ORNL, who organized the Nipping Science Forum (NSF) for a beautiful summer. I also want to thank the friends that I met at NCAR.

I want to thank my advisors, teachers, and friends in China and US for their constant encouragement and support.

I am indebted to my family, giving me endless love, constant encouragement and unwavering support. I couldn't have done it without them! I also want to thank myself for keeping growing up.

Finally, best wishes to this exceptional 2020 with challenges related to and beyond the COVID-19!

Abstract

Multi-Scale Understanding and Modeling of Plant Hydraulics

Lingcheng Li, Ph.D.

The University of Texas at Austin, 2020

Supervisor: Zong-Liang Yang

Co-Supervisor: Ashley Michelle Matheny

Plant hydraulics describes the mechanisms of water uptake from the soil to roots, water transport through the xylem to leaves, and water loss via stomata. Mechanistic modeling of plant hydraulics has advanced in recent decades with a demonstrated capability to simulate evapotranspiration and gross primary production, especially under water stress conditions. As these water stress conditions are likely to intensify in a warming climate, it is crucial to ensure land surface models (LSMs) for use in Earth system models (ESMs) are equipped with appropriate parameterizations of plant hydraulics. Most LSMs employ an idealized "big-leaf" concept to regulate water and carbon fluxes in response to soil moisture stress through empirical soil hydraulics schemes (SHSs). Such schemes have been shown to cause significant uncertainties in water and carbon simulations. This dissertation aims to better understand and simulate the role of plant hydraulics in regulating the terrestrial water and carbon cycles through observational data analysis, numerical model development, and continental-scale applications.

Chapter 2 analyzes the impacts of plant hydraulics-related properties on the sensitivity of vegetation interannual variability to hydroclimatic factors such as

precipitation and atmospheric water vapor pressure deficit (VPD) in North America. Compared to isohydric plants, anisohydric plants are more negatively affected by VPD and would suffer more from increasing atmospheric moisture stress under climate change. Focusing on the Noah-MP land surface model, Chapter 3 presents a novel plant hydraulics scheme (PHS) (hereafter referred to as Noah-MP-PHS), which employs a big-tree concept by considering the whole-plant hydraulic strategy. Noah-MP-PHS is evaluated using plot-level observations from UMBS, and improves water and carbon simulations, especially during dry soil conditions. Noah-MP-PHS can reproduce contrasting plant hydraulic behaviors for two species, i.e., isohydric 'risk-averse' red maple and anisohydric 'risk-prone' red oak. The stem water storage in PHS enables nocturnal plant water recharge and provides an important buffer to relieve xylem hydraulic stress during dry soil conditions. Chapter 4 extends the plot-level and tree-level PHS experiments to the forest regions in the continental United States (CONUS). Six experiments are conducted, including three SHS experiments and three PHS experiments. PHS_plot, PHS risk-averse, and risk-prone experiments use calibrated PHS parameters, respectively, from the plot-level, maple tree-level, and oak tree-level simulations as described in Chapter 3. The spatial sapwood area and volume indexes over the CONUS forest regions are estimated for the first time for use in land surface modeling. PHS impacts the ET partitioning to transpiration and the total water storage anomaly over the CONUS. Plant hydraulic traits play an essential role in PHS water simulations. Therefore, the implementation of plant hydraulics, along with more realistic representations of plant traits and hydraulic strategies, could reconcile observations and models of terrestrial water cycles. Noah-MP-PHS provides a useful platform to better understand the roles of terrestrial ecosystems on global carbon & water cycles and energy budget, including research of data assimilation, land-atmosphere interaction, extreme event prediction, climate projection, and so on.

Table of Contents

List of Tables

List of Figures

Chapter 1: Introduction

1.1 IMPORTANT ROLE OF TERRESTRIAL TRANSPIRATION

Terrestrial ecosystems play a critical role in the global carbon cycle and act as a natural buffer against rising atmospheric CO_2 (IPCC 2013; Shiga et al. 2018). Plants absorb more than one-fourth of fossil fuel emissions, and significantly slow down the rise in atmospheric CO_2 and thus global warming (Shevliakova et al., 2013; Le Quéré et al., 2013&2018). Transpiration by plants is the dominant component of total terrestrial evapotranspiration (Jasechko, 2013; Schlesinger et al., 2014; Good et al., 2015). This process couples the water and carbon cycles and controls surface energy partitioning, thus playing a principal role in land surface and atmosphere/climate feedbacks (Bonan et al., 2008; Matheny et al., 2014a).

A warming climate is expected to intensify the global hydrological cycle and likely induce more frequent and severe droughts over many regions (Dai 2013; Li et al., 2020). Rising temperatures will likewise cause an increase in atmospheric water vapor pressure deficit (VPD) (Grossiord et al., 2020). Plants, therefore, are expected to face more hydroclimatic stresses due to decreasing soil water supply alongside increasing atmospheric water demand (Figure 1.1) (McDowell et al., 2008; Anderegg et al., 2012; Anderegg et al., 2018). Numerous studies have shown the vital role of soil moisture or precipitation in controlling vegetation greenness (Wang et al., 2016; Wang et al., 2017; Jung et al., 2017; Zeng et al., 2005; Ahlstrom et al., 2015; Green et al., 2019), and emerging studies highlight the importance of VPD in playing a more significant role than precipitation/soil moisture (Konings et al., 2017; Novick et al., 2016; Liu et al., 2020; Yuan et al., 2019). It is crucial to understand and simulate the dynamics of transpiration in order to better predict ecosystem–atmosphere feedbacks in water, carbon, and energy exchange

under climate change with likely increasing water stress (Bonan et al., 2008; Allen et al., 2010; Choat et al., 2012; Sperry et al., 2016; Lemordant et al., 2018).

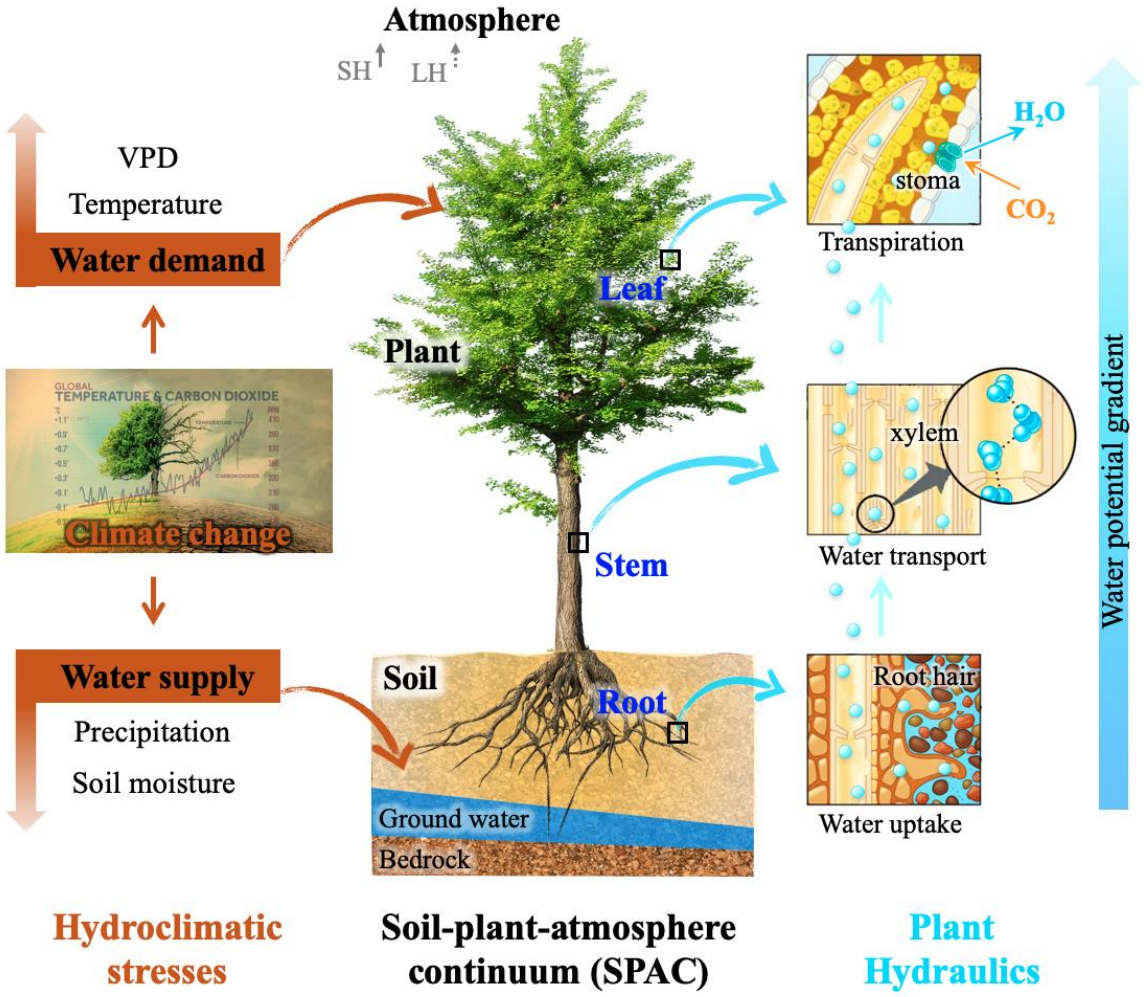

Figure 1.1: Diagram of hydroclimatic stresses, soil–plant–atmosphere–continuum (SPAC), and plant hydraulics. SH: sensible heat; LH: latent heat. Figure 1.1 was made based on figure materials from: https://www.nicepng.com/; https://www.iberdrola.com/environment/climate-change-mitigation-and-adaptation; http://www.bio.miami.edu/dana/226/226F08_9print.html; https://www.climatecentral.org/.

1.2 PLANT HYDRAULICS AND ITS MODELING

Water transport in plants enables the photosynthesis, and affects the terrestrial water and carbon cycles, and energy balance (Brodribb, 2009; Anderegg et al., 2015; Matheny et al., 2017; McCulloh et al., 2019). Plant hydraulics describes the fundamental mechanisms of how vascular plants acquire, transport, store and use water (Figure 1.1) (Dixon & Joly, 1895; McDowell et al., 2019; Matheny et al., 2017; Anderegg et al., 2018). Transpiration is regulated dynamically through the stomatal aperture, which, in many cases, is governed by water status and plant hydraulic properties (Sperry, 2000; Buckley 2005; Skelton et al., 2015; Matheny et al., 2017; Anderegg et al., 2018). Water movement through the plant vascular systems is regulated by the whole-plant hydraulic strategy, which is the culmination of emergent phenotypical hydraulic functional traits at the leaf, stem, and root levels (Matheny et al., 2017; McCulloh et al., 2019). At the leaf level, there are two opposing strategies for the regulation of stomatal openness in the face of water stress: isohydricity, in which plants readily close stomata to maintain a steady and high leaf water potential in order to conserve water; and anisohydricity, in which plants maintain open stomata longer while incurring highly negative leaf water potential (LWP) to maximize carbon uptake. Most plants operate along with a range of intermediate strategies between these two extremes (McDowell et al., 2008; Skelton et al., 2015; Blackman 2018; Zhu et al., 2018). At the stem level, plants differ in their xylem architecture, including ring-porous, diffuse-porous, and tracheid-based types (Oren et al., 1999; Matheny et al., 2017). The diversity of xylem architecture and physiology alongside numerous other vessel traits (e.g., vessel diameter, density and interconnectedness) determine xylem hydraulic functioning and its resistance to hydraulic impairment (cavitation) (Pockman & Sperry, 2000; Choat et al., 2012). The ability of a plant to store water, or its hydraulic capacitance, likewise plays a critical role in regulating the water status and tree function on time scales ranging from

diel to seasonal (Matheny et al., 2015; Matheny et al., 2017; Yan et al., 2020). Plant hydraulic control also results from the properties of root systems and the rhizosphere, such as rooting depth and vertical distribution, lateral extent and competitive dynamics, fine root area, water extraction efficiency, mycorrhizal interactions, and hydraulic redistribution (Canadell et al., 1996 & 2007; Allen, 2009; Reichstein et al., 2014; Wullschleger et al., 2014).

Mechanistic modeling of plant hydraulics has advanced in recent decades and shown clear evidence of providing a better representation of the vegetative regulation of global carbon and water fluxes (Anderegg and Martin, 2020; McDowell et al., 2019; Mencuccini et al., 2019; Anderegg et al., 2018; Mackay et al., 2015; Hunt et al., 1991). There are three broad categories of plant hydraulics models, although all vary in their parameterization and implementation (Table 1.1):

(1) The first category is the pipe model (PPM), which treats the water movement within vascular conduits as laminar flow through pipes (Shinozaki et al., 1964a & 1964b; McCulloh et al., 2003; Lehnebach et al., 2018). These idealized vertical, parallel pipes can be either connected or disconnected from adjacent pipes depending on model assumptions. The flow through each pipe is commonly simulated by the Hagen–Poiseuille law (Roderick and Berry, 2001; Mrad et al., 2018). Some of these models (e.g., the WBE model; West et al., 1999; Savage et al., 2008) use additional allometric scaling laws to describe the vascular architecture, such as conduit taper, and further consider hydraulic trade-offs (e.g., the Botanical Network Model; Savage et al., 2010). The network model proposed by Mrad et al. (2018) based on xylem anatomy and simulates lateral embolism spread, providing another solution to further explore xylem tissue hydraulic behavior and vulnerability to cavitation.

(2) The second category is the electrical analogy model (EAM), which conceptualizes water flow through plants as being analogous to the current through an electric circuit with a series of resistance and/or capacitance (Sperry et al., 1998). EAMs conceptualize water flow through plants as analogous to the current through an electric circuit with series of resistance and/or capacitance (Sperry et al., 1998). An EAM is based on an ordinary differential equation and has high computational efficiency. EAMs have two subcategories: resistor model (RMs) and resistance-capacitance models (RCMs). An RM regards plant hydraulics as a resistor (or a series of resistors) to transport water flow. Sellers et al. (1986) proposed an RM in the SiB model, which included two resistors: averaged plant vascular resistance and soil-root resistance. Other examples include the plant hydraulics schemes developed by Sperry et al. (1998), the SOX scheme developed by Eller et al. (2018), and the PHS scheme in CLM5 (Kennedy et al., 2019). Besides the resistor, RCMs also consider plant-water storage or capacitance, e.g., the schemes developed by Sperry et al. (1998), Steppe et al. (2006), Gentine et al. (2016), and Xu et al. (2016). The hydraulic capacitance, especially for tall trees, has been demonstrated by field observation to play a critical role in regulating transpiration at both short- and long-term scales (Matheny et al., 2015; Matheny et al., 2017; Yan et al., 2020).

(3) The third category is the porous media model (PMM), which assumes that water movement through interconnected tracheids or xylem vessels resembles porous media flow (Chuang et al., 2006; Bohrer et al., 2005). A PMM typically uses the Richards equation for non-saturated porous media flow, which combines the continuity equation with Darcy's law, leading to a nonlinear partial differential equation. Therefore, these models can describe the detailed spatiotemporal dynamics of a tree's hydraulic system, but at the cost of substantial computational and parametric demands. The architecture of PMMs ranges from single beam (stem only) models (Chuang et al., 2006; Mirfenderesgi et al., 2016 &

2019; Yan et al., 2020), to the FETCH model with a three-dimensional stem and branch structure (Bohrer et al., 2005), to the Xylem Water Flow (XWF) model including root, stem, and branches (Janott et al., 2011; Bittner et al., 2012).

	Plant hydraulics model type			
	Pipe model	Electric analogy model		Porous media model
		Resistor model	Resistor-capacitance model	
Vascular architecture assumption	Series of pipes	Electric circuit with resistance	Electric circuit with resistance and capacitance	Continuous porous media
Storage inclusion	Yes/No	No	Yes	Yes
Governing law or equation	Hagen–Poiseuille law, allometric scaling laws	Darcy's law		Richards equation
Typical model scale	Tissue level, tree level, ecosystem level	Tree level, cohort level, stand level, ecosystem level		Tree level, cohort level
Computational demand	Moderate to high	Low to moderate		High
Example of evaluation data	Tree-level measurements	Sap flux, flux-tower data, ecosystem-scale data		Sap flux
Parameterization required	Many parameters	Some parameters		Many parameters
Examples	1. Pipe Model (Shinozaki et al., 1964a & b) 2. WBE (West et al., 1999) 3. Stem Hydraulic Model (Roderick and Berry, 2001) 4. Botanical Network Model (Savage et al., 2010) 5. Network Model (Mrad et al., 2018) 6. Pipe Model in HOTTER (Trugman et al., 2019b)	1. SiB (Sellers et al., 1986) 2. SPA (Sperry et al., 1998) 3. TREES (Mackay et al., 2011) 4. SOX (Eller et al., 2018) 5. PHS in CLM5 (Kennedy et al., 2019)	1. SPA (Williams et al., 1996) 2. Dynamic Flow and Storage Model (Steppe et al., 2006) 3. VIC+ (Luo et al., 2013) 4. ED2-Hydro (Xu et al., 2016) 5. RCL Model (Zhuang et al., 2014)	1. PM (Chuang et al., 2006) 2. FETCH (Bohrer et al., 2005) 3. TFS v.1-Hydro (Christoffersen et al., 2016) 4. XWF (Janott et al., 2011)

Table 1.1: Commonly used plant hydraulics models and their key features.

1.3 PLANT WATER STRESS PARAMETERIZATION IN LAND SURFACE MODELS

As a key component of Earth system models (ESMs), land surface models (LSMs) simulate water, carbon and energy fluxes, and are used for drought/flood prediction, weather forecasts, and climate prediction (Yang et al., 2011; Bonan & Doney et al., 2018). The majority of LSMs use an idealized "big leaf" to represent all vegetation functions as a single leaf or a pair of leaves (sunlit and shaded) (Luo et al., 2018). Within the big-leaf framework, LSMs do not resolve water-state variables within plants and therefore do not have the ability to explicitly represent the plant water-stress status. Therefore, most LSMs typically parameterize the effects of soil water stress on vegetation and thus surface fluxes (i.e., water, carbon and energy fluxes) using empirical functions based on either soil water content or soil water potential (Egea et al., 2011; Verhoef & Egea, 2014; Powell et al., 2013; Sitch et al., 2015). These traditional schemes, which we refer to as soil hydraulics schemes (SHSs), depend on soil hydraulic properties and a few plant functional parameters (e.g., root distribution), but the role of plant traits (e.g., xylem conductivity) in controlling transpiration is largely ignored (Christoffersen et al., 2016). Many such models are satisfactory when soil moisture is adequate for transpiration, but most are unable to simulate water and carbon fluxes well under water-limited conditions (e.g., Calvet et al., 1998; Grant et al., 1999; Tuzet et al., 2003). Additionally, these LSMs fail to capture the asymmetry of daytime water and carbon fluxes under conditions of low soil moisture content, resulting in underestimation (overestimation) of fluxes in the morning (afternoon) (Matheny et al., 2014a; Tuzet et al., 2003). Therefore, SHS functions cannot well capture plants' response to water stress conditions and have been shown to contribute significant uncertainty to water and carbon simulations by LSMs (Dirmeyer et al., 2006; Powell et al., 2013; Matheny et al., 2014a; Niu et al., 2011; Trugman et al., 2018; Zheng et al., 2019).

Previous studies have shown that the incorporation of a holistic, whole-plant hydraulic strategy in place of the more traditional semi-empirical SHS approach, along with hydraulic trait-based vegetation representation, can serve to improve simulations of carbon and water fluxes, particularly in cases of drought and other disturbances (Christoffersen et al., 2016; Mirfenderesgi 2019; Kennedy et al., 2019; Liu et al., 2020).

1.4 MOTIVATING QUESTIONS

Based on the advancements in theory development, data availability (e.g., in-situ plant hydraulic traits and plant water status related remote sensing observations) and physical-based models of plant hydraulics, this dissertation thus aims to address the following questions.

Chapter 2: (1) How do hydroclimatic factors affect the interannual variability (IAV) of vegetation productivity for different ecosystems? (2) How do plant hydraulics-related properties affect the sensitivity of vegetation productivity IAV to hydroclimatic factors?

Chapter 3: (1) By implementing a plant hydraulics scheme (PHS) in Noah-MP LSM, can PHS improve water and carbon simulations? (2) Can PHS replicate different hydraulic behaviors for species with different hydraulic strategies (e.g., isohydric risk-averse vs. anisohydric risk-prone)?

Chapter 4: (1) How can different hydraulic strategies (i.e., risk-prone vs. risk-averse) influence ET partitioning and total water storage over the continental United States? (2) How do plant traits affect such PHS simulations?

1.5 ORGANIZATION OF THE DISSERTATION

Chapter 1 reviews the current progress in plant hydraulics and the limitations of traditional LSMs, pinpoints the need for better understanding the role of plant hydraulics

on water and carbon cycles, and the representation plant hydraulics in LSMs, followed by the overarching questions and research organization.

In Chapter 2, we used the large spatial scale datasets to examine how plant hydraulics-related properties affect the sensitivity of vegetation interannual variability to hydroclimatic factors, including the water supply (i.e., precipitation) and water demand (i.e., vapor pressure deficit). This study highlights the importance of plant hydraulics-related properties on the coupling strength between vegetation greenness and hydroclimatic factors, and implicates the potential benefits to represent PHS in ESMs and therefore could better simulate vegetation response, and carbon and water fluxes, particularly under water stress conditions.

In Chapter 3, we implemented a novel PHS for Noah-MP (hereafter, Noah-MP-PHS), which employs a big-tree rather than the big-leaf concept, wherein the whole-plant hydraulic strategy is considered including root-level soil water acquisition, stem-level hydraulic conductance and capacitance, and leaf-level isohydricity and hydraulic capacitance. We evaluated Noah-MP-PHS using observations from the University of Michigan Biological Station and compared it with the default Noah-MP. Noah-MP-PHS can also reproduce different patterns of transpiration, stem water storage and root water uptake during a two-week dry-down period for two species with contrasting plant hydraulic behaviors, i.e., the “cavitation risk-averse” red maple and the “cavitation risk-prone” red oak.

In Chapter 4, by using the parameters calibrated from plot-level and tree-level experiments in chapter 3, we extended our simulations to CONUS to better understand plant hydraulics at the large spatial scale. We examine the difference of water fluxes (1) between the default SHSs experiments and PHS experiments with plot-level configuration,

(2) between PHS experiments with different hydraulic strategies (i.e., risk-prone vs. risk-averse), and (3) how do the plant traits can affect these differences.

In Chapter 5, I summarize the conclusions and limitations & future research work.

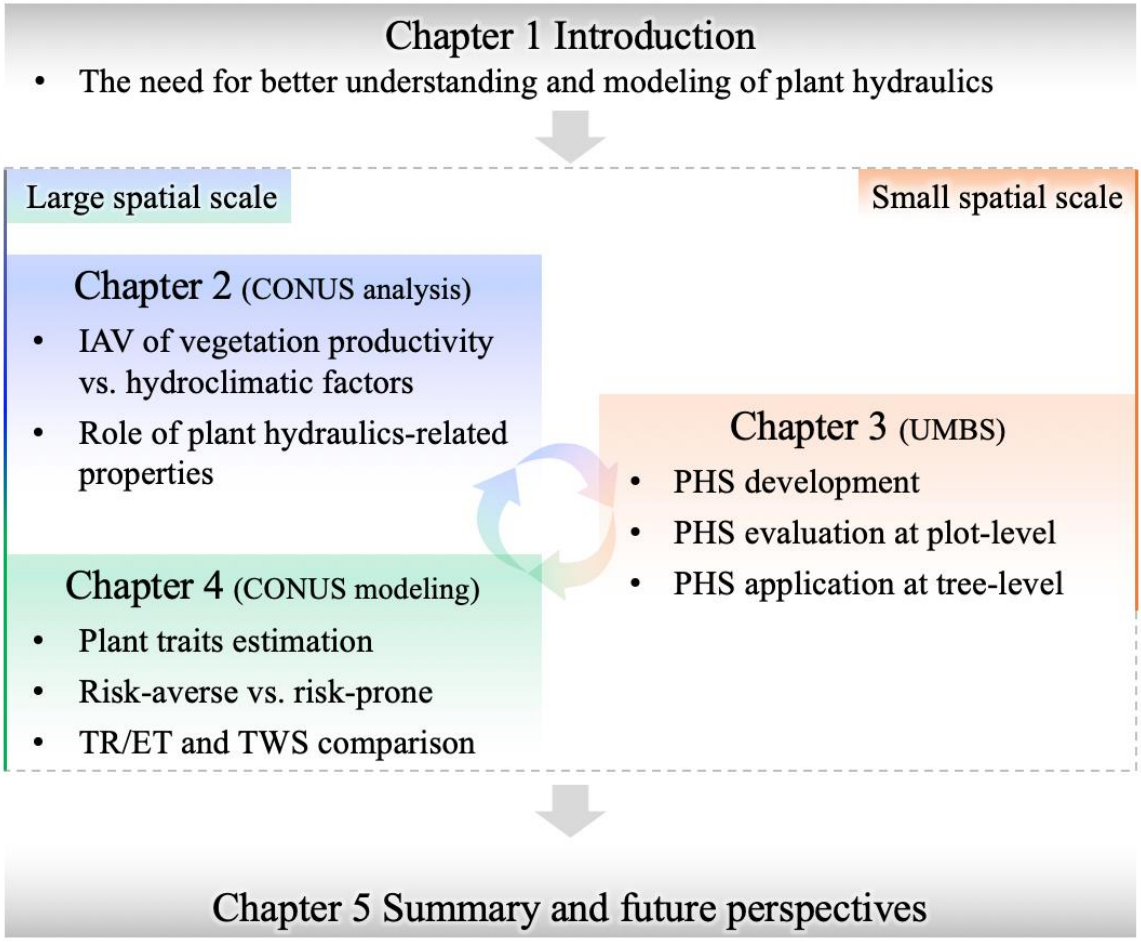

Figure 1.2: Diagram of dissertation structure: multi-scale understanding and modeling of plant hydraulics.

Chapter 2: Plant hydraulics-related properties Control the Sensitivity of Vegetation Productivity to Hydroclimatic Factors

ABSTRACT

Terrestrial ecosystems are likely expected to experience increasing moisture stress, with decreasing precipitation supply and rising atmospheric moisture demand under global warming. Plant hydraulics regulates a plant's ability to acquire, transport, and use water, and plays a critical role on water and carbon cycles. In this study, we examined how do plant hydraulics-related properties affect the sensitivity of interannual variability of vegetation productivity to hydroclimatic factors in North America. Our results show that precipitation has positive effects on vegetation productivity for arid ecosystems (aridity index < 0.65; e.g., grassland) and negative effects on humid ecosystems (aridity index ≥ 0.65; e.g., forests). VPD negatively correlates with vegetation productivity, while the temperature has positive effects on vegetation productivity. Generally, plants with higher canopy and larger biomass are less sensitive to precipitation and VPD. Anisohydric plants are more sensitive to VPD than the relatively isohydric plants. Furthermore, anisohydric humid ecosystems are more sensitive to VPD than precipitation, while anisohydric arid ecosystems are equally sensitive to precipitation and VPD. Given the projected rising VPD under climate change, anisohydric plants may suffer more from the atmospheric moisture stress. Our study highlights the importance of plant hydraulics-related properties on the coupling strength between vegetation productivity and hydroclimatic factors, indicating the implementation of plant hydraulics in Earth system models (ESMs) therefore could better simulate vegetation productivity, and carbon and water fluxes.

2.1 INTRODUCTION

Terrestrial ecosystems play a critical role in the global carbon cycle and act as a natural buffer against rising atmospheric CO_2 (IPCC 2013; Shiga et al. 2018). Plants absorb more than one-fourth of fossil fuel emissions, and significantly slow down the rise in atmospheric CO_2 and thus global warming (Shevliakova et al., 2013; Le Quéré et al., 2013&2018). There is a large interannual variability (IAV) of global atmospheric CO_2, which is primarily driven by terrestrial ecosystem processes (Cox et al., 2013; Poulter et al., 2014). Therefore, understanding the IAV of ecosystem productivity could help forecast long-term biosphere responses to climate change (Wang et al., 2014; Cox et al., 2015; Baldocchi et al., 2018; Piao et al., 2020).

Water stress influences the IAV of ecosystem productivity (Piao et al., 2020; Jung et al., 2020). Generally, ecosystems face two hydroclimatic stresses in the form of low water supply (e.g., precipitation or soil moisture) and high atmospheric water demand (i.e., vapor pressure deficit, VPD). Numerous studies have shown the vital role of soil moisture or precipitation on vegetation IAV (Wang et al., 2016; Wang et al., 2017; Jung et al., 2017; Zeng et al., 2005; Ahlstrom et al., 2015; Green et al., 2019), and emerging studies highlight the importance of VPD in playing a more significant role than precipitation/soil moisture (Konings et al., 2017; Novick et al., 2016; Liu et al., 2020; Yuan et al., 2019). With likely decreasing precipitation supply and increasing VPD under a warming climate, vegetation is expected to face increasing challenges from these two hydroclimatic stresses (Grossiord et al., 2020; Green et al., 2019; Yuan et al. 2019; Brodribb et al., 2020).

Water transport in plants is necessary for photosynthesis and influence the global carbon cycle (Brodribb, 2009; Anderegg et al., 2015; Matheny et al., 2017; McCulloh et al., 2019). Plants with different hydraulic traits, e.g., the sensitivity of stomata openness to leaf water potential, xylem conductivity and rooting depth, use different strategies to

regulate their abilities to acquire, transport, and use water (Sperry, 2000; Buckley 2005; Skelton et al., 2015; Anderegg et al., 2018). Isohydric plants exert tight stomatal regulation and maintain relatively constant plant water potential to minimize transpiration and avoid xylem cavitation, but at the cost of reduced carbon fixation. In contrast, anisohydric plants tend to tolerate low leaf water content and maintain transpiration longer to maximize carbon uptake (Matheny et al., 2017; Konings et al., 2017a; Feng et al., 2019; McDowell et al., 2008). Besides, stem traits, e.g., xylem architecture and water storages (Matheny et al., 2015; Yan et al., 2020), and root traits, e.g., root area and rooting depth (Allen, 2009; Reichstein et al., 2014) control water supply to the leaves.

Previous studies have explored the influence of plant hydraulics-related properties on ecosystems' sensitivity to the water supply and atmospheric demand at large spatial scale. Konings et al. (2017a) found that anisohydric grassland productivity is far more sensitive to variations in VPD than precipitation during drought years. Giardina et al. (2018) showed that IAV of photosynthesis of tall forests is less sensitive to precipitation variability than short forests in Amazonia. However, the influence of plant hydraulics on the relationships between IAV of vegetation productivity and hydroclimatic factors is still not fully understood. Therefore, this study aims to examine the role of hydraulic properties on the sensitivity of vegetation IAV to hydroclimatic factors, especially precipitation and VPD across diverse ecosystems in North America. Specifically, we will explore 1) How hydroclimatic factors affect the vegetation productivity IAV for different ecosystems? 2) How plant hydraulics-related properties affect the sensitivity of vegetation productivity IAV to hydroclimatic factors? Section 2 introduces the large-scale datasets and analysis method. Section 3 is the results followed by the discussion and conclusions in section 4.

2.2 METHODOLOGY

In this section, we present the dataset and analysis methods. We collected the vegetation productivity proxy data and climatic factors to conduct partial correlation analysis. Then, four plant hydraulics-related properties were used to examine how their influence on the partial correlation coefficients.

2.2.1 Data

We used satellite-derived Normalized Difference Vegetation Index (NDVI), which is the ratio of the difference between near-infrared reflectance and red visible reflection to their sum, as a proxy of vegetation productivity (Konings et al., 2017a; Wang et al., 2017). The NDVI was retrieved from the Advanced Very High Resolution Radiometer (AVHRR) instruments, which was produced by the Global Inventory Modeling and Mapping Studies (GIMMS) group (Pinzon & Tucker, 2014). The original 0.083° spatial and half-month interval NDVI was processed into a monthly 0.5° resolution (Table 2.1) from 1982–2015.

The major hydroclimatic factors that influence the IAV of vegetation productivity include VPD, precipitation, temperature. It should be noted that radiation can also affect vegetation productivity, e.g., at the tropical rainforests. Previous studies have shown that temperature is the dominant control factor in the Northern Hemisphere (Piao et al., 2020; Nemani et al., 2003). As our study region is located in North America, so we excluded the radiation in this study. The monthly daytime VPD was calculated based on the forcing from the North American Land Data Assimilation System (NLDAS) phase 2 (Mitchell et al., 2004; Xia et al., 2012). Daytime hourly VPD was first computed using NLDAS hourly data (i.e., specific humidity and air temperature) at 0.125° spatial resolution, which was processed as a monthly average with 0.5° resolution. The monthly 0.5° temperature and precipitation were also aggregated from the hourly 0.125° NLDAS dataset.

We collected four gridded plant properties that are related to plant hydraulic processes, including isohydricity (Konings et al., 2017b), forest canopy height (Simard et al., 2011), and above and below ground biomass (Spawn et al., 2020) (Figure 2.7). As mentioned in the introduction, the whole-plant hydraulic strategy is determined by the traits in the leaves, xylem, and roots. Isohydricity describes the degree of plants that controls their stomata in response to water stress. Konings et al. (2017b) developed a remote-sensing based ecosystem-scale anisohydricity using the satellite products of vegetation optical depth (VOD). Even though its calculation is based on a series of assumptions, these VOD-based datasets are generally consistent with the upscaled in situ species estimates (Li et al., 2017). Isohydricity is a comprehensive proxy of plant water use strategies. It is centered on leaf water potential, which in itself is an integration of a cascade of water potentials from the leaf, to the branch, to the trunk, to the root and ultimately the soil-to-root interface. The forest canopy height is another proxy of plant hydraulics. Canopy height relates to the rooting depth, the hydraulic path length and the volume available to store water. Besides, we also used the above and below ground biomass metrics. Generally, under a given climate, ecosystems with more abundant biomass may have more and deeper roots to access soil moisture, and could also have a larger plant capacitance to store water. All of these plant properties are processed from their original resolution to a 0.5° spatial resolution over 1982–2015.

The aridity index, the ratio of mean annual precipitation to mean annual potential evapotranspiration, is used to classify arid and humid ecosystems. The monthly precipitation and evapotranspiration from CRU TS v.4.0.4 were used to compute the aridity index.

Data type	Data name	Original spatial resolution	Original temporal resolution	Source
Vegetation	NDVI	0.083°	Half-month	Pinzon & Tucker, 2014
Climatic factor	Precipitation	0.125°	Hourly	Mitchell et al., 2004; Xia et al., 2012
	Temperature	0.125°	Hourly	
	VPD calculation	0.125°	Hourly	
Plant properties	Isohydricity	0.25°	Static	Konings et al., 2017b
	Canopy height	1 km	Static	Simard et al., 2011
	Above ground biomass	300 m	Static	Spawn et al., 2020
	Below ground biomass	300 m	Static	Spawn et al., 2020
Aridity index	Precipitation	0.5°	Monthly	Harris et al., 2020
	PET	0.5°	Monthly	

Table 2.1: Summary of datasets.

2.2.2 Analyses

This study was conducted in the domain covered by NLDAS (Figure 2.1), including the Contiguous United States and a part of Canada and Mexico. Our analysis focused on the growing season, which is defined as April–October (Piao et al., 2014). For example, the IAV of NDVI is computed as the annual variation of the NDVI mean during the growing season. To distinguish the role of hydroclimatic drives on the vegetation, we conducted partial correlation analysis between NDVI and one driver after statistically controlling other drivers' variations at the interannual timescale. All variables were detrended to isolate hydroclimatic factors' role from other potential drives that contribute to vegetation dynamics (e.g., CO_2 fertilization) (Wang et al., 2018a).

We then examined the relationships between partial correlation coefficients with plant hydraulics-related properties over different ecosystems. The MODIS IGBP land cover type (Table 2.2, Friedl et al., 2010 and 2015) and Köppen-Geiger climate classification were used to select out sub-region. To reduce the influence of human

activities (e.g., irrigation), croplands were excluded for all analysis. We selected seven regions with six land cover types that have sufficient pixels to support rigorous analysis (Figure 2.1). Based on the aridity category (UNEP 1997), grassland and open shrub are classified as arid ecosystems (aridity index < 0.65, Figure 2.8), and other four types were classified as humid ecosystems (aridity index ≥ 0.65) (see Figure 2.3d).

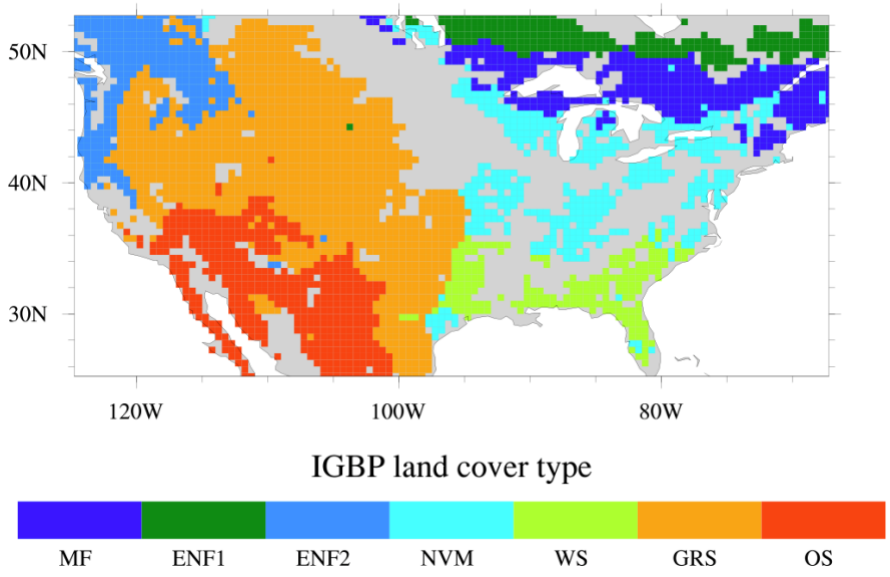

Figure 2.1: Major IGBP land cover types. Mixed forest (MF), evergreen needleleaf forest (ENF), natural vegetation mosaic (NVM), woody savannas (WS), grasslands (GRS), open shrublands (OS), see more in Table S1 for land covers' definition. It should be noted that both ENF1 and ENF2 are Evergreen Needleleaf forest but fall within different Köppen-Geiger climate zones. Grids shown with grey color were excluded in our analysis.

2.3 RESULTS

2.3.1 Hydroclimatic controls on vegetation greenness

Figure 2.2 shows the correlation coefficients between vegetation greenness (NDVI) and hydroclimatic factors over the period of 1982–2015. For NDVI-precipitation, 55.9% (44.1%) of pixels show a positive (negative) relationship (Figure 2.2a). Generally, the arid region with small aridity indicates positive partial correlation coefficients. The humid region with larger aridity indicates more negative correlation coefficients (Figure 2.2d). Most study regions show a negative correlation between VPD and NDVI. VPD has more negative effects on the regions with lower aridity and high temperature than the humid and cold regions (Figure 2.2e). 84.6% of study regions demonstrate a positive correlation between NDVI and temperature. Generally, cold regions with limited thermal conditions show larger positive sensitivity of NDVI to temperature (Figure 2.2f).

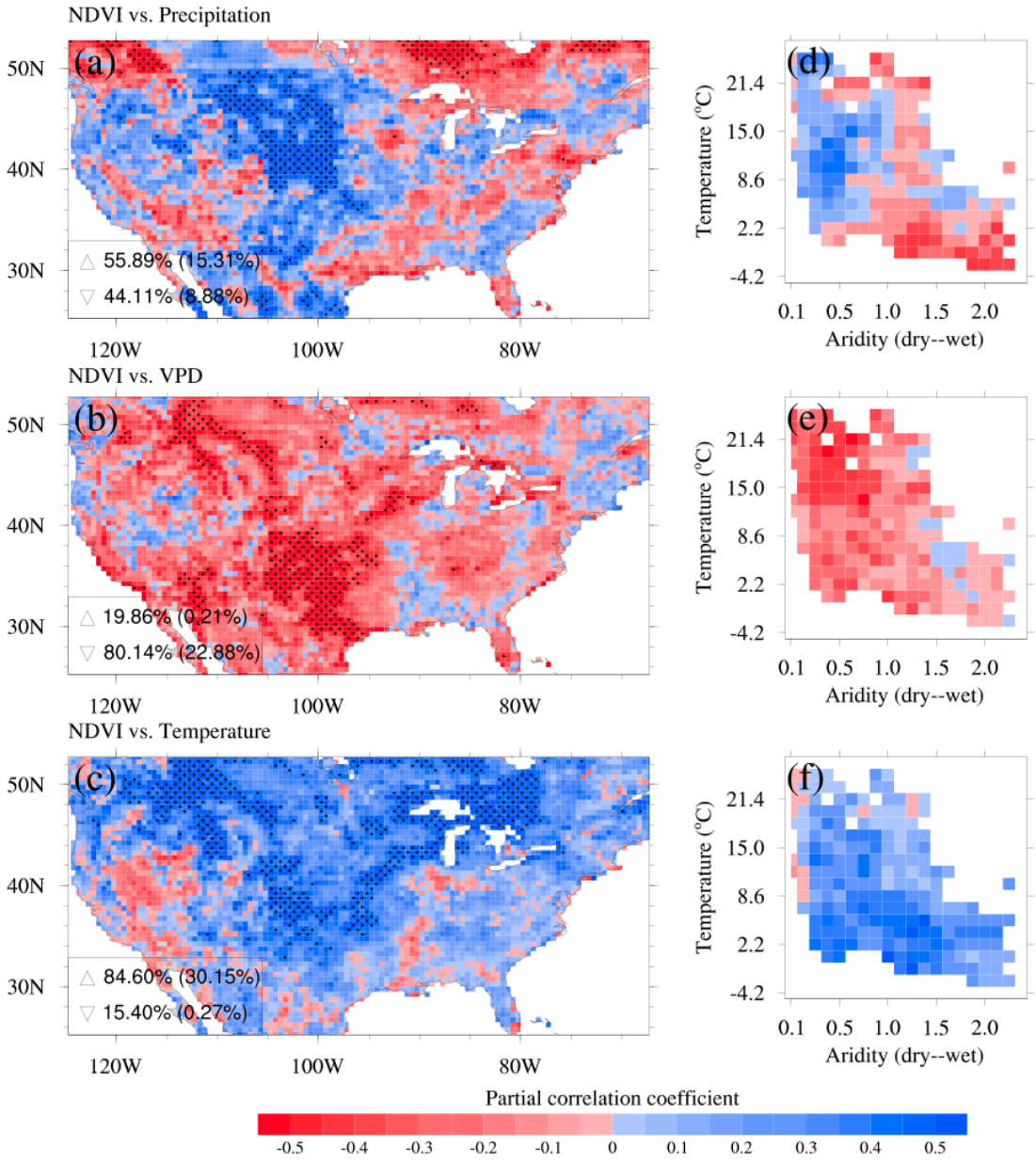

Figure 2.2: Spatial distributions of the partial correlation coefficients between NDVI and precipitation (a), VPD (b), and temperature (c), respectively. Distributions of averaged partial correlation coefficient in the aridity index – mean annual temperature domain for precipitation (d), VPD (e), and temperature (f), respectively. The distribution of aridity and temperature are shown in Figure S1. "Δ"/"∇" denote the percentage of grids with an increasing/decreasing pattern. The stippling indicates the regions with a significant partial correlation coefficient (Student's t-test, $p < 0.05$).

2.3.2 Comparison of partial correlation coefficients between different ecosystems

We further summarized the average of partial correlation coefficients over different ecosystems in Figure 2.3. For NDVI-precipitation, the forest ecosystems (i.e., mixed forest (MF) and evergreen needleleaf forest (ENF)) show overall negative correlation coefficients. While the grassland (GRS) and open shrub (OS) have positive correlation coefficients (Figure 2.3a). The natural vegetation mosaic (NVM) and woody savanna (WS) ecosystems show slight positive correlation coefficients between NDVI and precipitation overall. These correlation patterns are related to ecosystems' aridity (Figure 2.3d) that arid (humid) ecosystems have positive (negative) correlation. All ecosystems have negative correlation responses between NDVI and VPD, especially for grassland and open shrubs. Generally arid ecosystems show more negative impact of VPD on NDVI. All the ecosystems show a positive correlation between vegetation greenness and temperature, and generally, ecosystems with lower mean annual temperature have higher positive correlation coefficients.

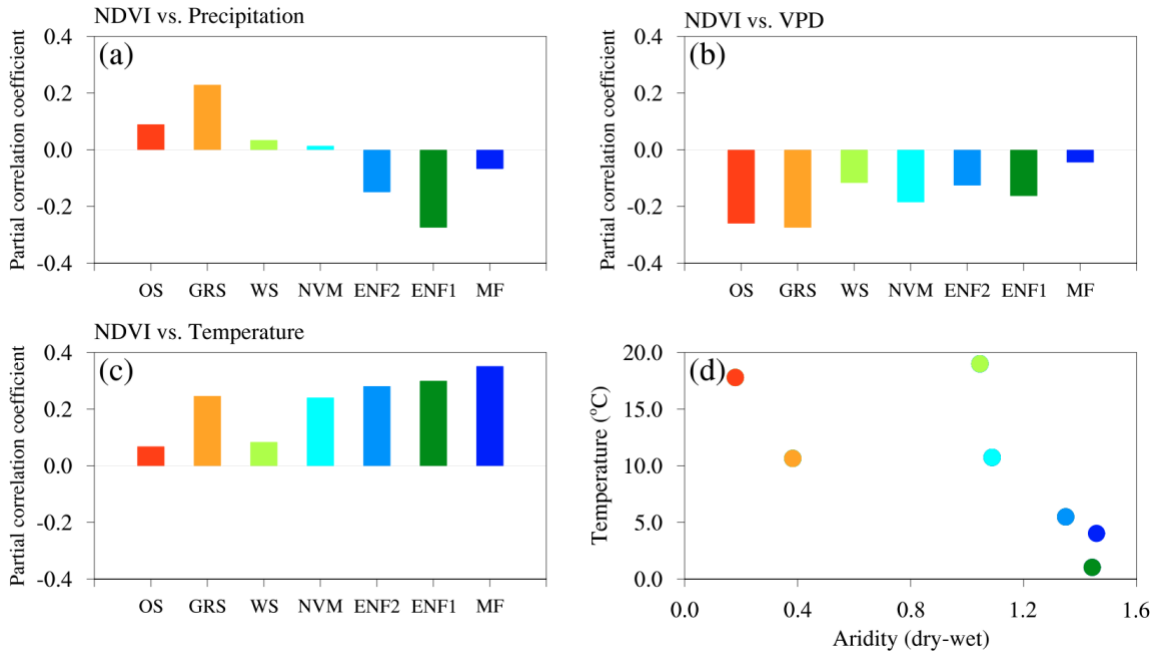

Figure 2.3: The average of partial correlation coefficients between vegetation and precipitation (a), VPD (b), and temperature (c) for different ecosystems. The mean annual temperature and aridity index for different land cover types (d). Warm–cold colors represent different ecosystems from arid (aridity index < 0.65) to humid (aridity index ≥ 0.65) regions, corresponding to the same colors in Figure 2.1.

2.3.3 Connection to plant hydraulics-related properties

In this section, we analyze the relationships between partial correlation coefficients (PCCs) and different plant hydraulics-related properties, including canopy height, above and below ground biomass, and isohydricity. There is a positive correlation between canopy height and above/below biomass. Therefore, the relationship between a given PCC and canopy height is similar to the relationship between that PCC and above/below ground biomass. In the following analysis, we compared the relationships of PCCs and plant hydraulics-related properties between the arid ecosystems (i.e., grass and open shrub) and the humid ecosystems (i.e., mixed forest, evergreen needleleaf forest, natural vegetation mosaic, woody savannas).

For NDVI-precipitation, the positive correlation coefficients of the arid grass ecosystem show a decreasing with above and below ground biomass (Figures 2.4a–2.4c). With larger values of these properties, the grass ecosystem potentially has more and deeper roots to access deeper soil moisture and hence tend to a less positive sensitivity to precipitation. Open shrub ecosystem shows slightly different patterns with the grass ecosystem, which could be due to the limitation of NDVI and biomass datasets as the vegetation here is very sparse. It should be noted that canopy height dataset is the measurements for tree height and is thus not proper descriptor for grasslands and open shrub ecosystems, but it still shows some similar patterns for precipitation correlations. However, the humid ecosystems have negative precipitation correlation coefficients, and also show increasing trends with canopy height, and above and below ground biomass.

Isohydricity in general have a different relationship with the NDVI-precipitation partial correlation coefficients for arid and humid ecosystems (Figure 2.4d). For arid grass ecosystem, the positive PCC increases with isohydricity. This is because larger isohydricity values (i.e., more anisohydric behavior) tends to open stoma longer under dry conditions,

requiring higher water consumption and hence illustrating more positive NDVI-precipitation correlations. For the humid ecosystems, there are no apparent patterns of the PCCs with isohydricity because these ecosystems are generally less water-limited. But for the relative short-term drought events when water is more limited, which is not our goal here, the precipitation correlation patterns may be different. Another possible reason is that the isohydricity dataset is computed based on the assumption of negligible plant water storage. This could lead to underestimation of isohydricity in ecosystems with high coverage of forest (Konings et al., 2017).

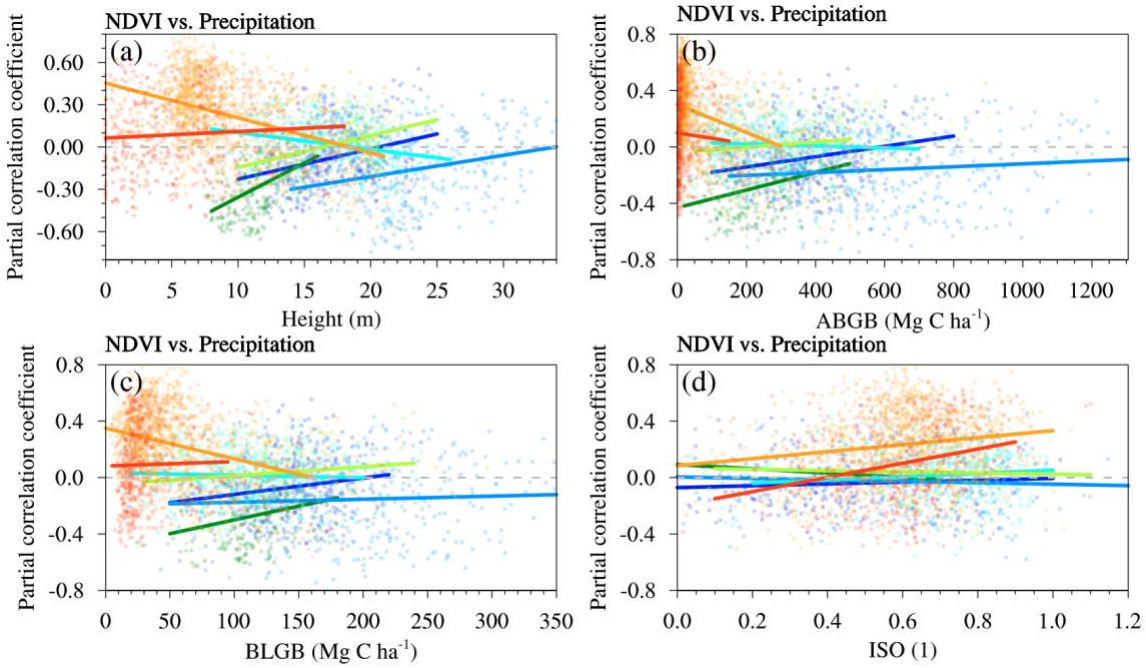

Figure 2.4: The relationships between partial correlation coefficients of NDVI-precipitation and plant hydraulics-related properties, (a) canopy height, (b) above ground biomass (ABGB), (c) below ground biomass (BLGB), and (d) isohydricity (ISO). The colored half-transparent dots and its regression line shows how partial correlation coefficients change with different plant hydraulics-related properties. Different colors are for different ecosystem, corresponding to the same colors in Figure 2.1.

Generally, both arid and humid ecosystems show similar patterns between PCCs of NDVI-VPD and plant hydraulics-related properties. There are overall increase patterns of negative correlation coefficients with the increase of canopy height and more above and below ground biomass. Ecosystems with larger vales of these properties potentially have more and deeper roots to access more available water and also have larger plant water storage, and hence have more water supply and less negative PCCs of NDVI-VPD. For the isohydricity (Figure 2.5d), the correlation coefficients show decreased patterns with isohydricity. Anisohydric plants tend to open the stoma longer under dry conditions, and hence are more negative impacted by VPD.

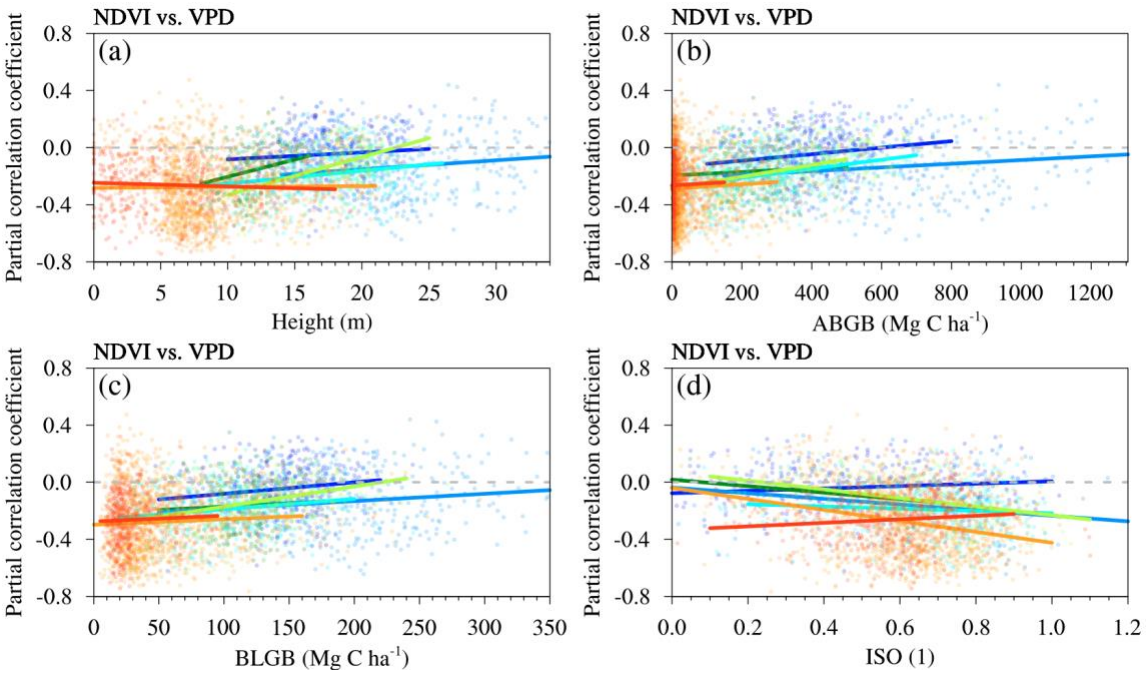

Figure 2.5: Similar to Figure 2.4 but for the PCCs of NDVI-VPD.

For the arid grass ecosystems, the PCC of NDVI-temperature shows increasing patterns with larger values of canopy height, above and below ground biomass (Figures 2.6). Grass with larger these properties could potentially access more soil moisture, and hence better use the thermal condition. Most of the ecosystems show the PCCs of NDVI-temperature increase with the isohydricity. This could be because anisohydric plant tends to open stoma longer under dry conditions and better utilize the thermal conditions.

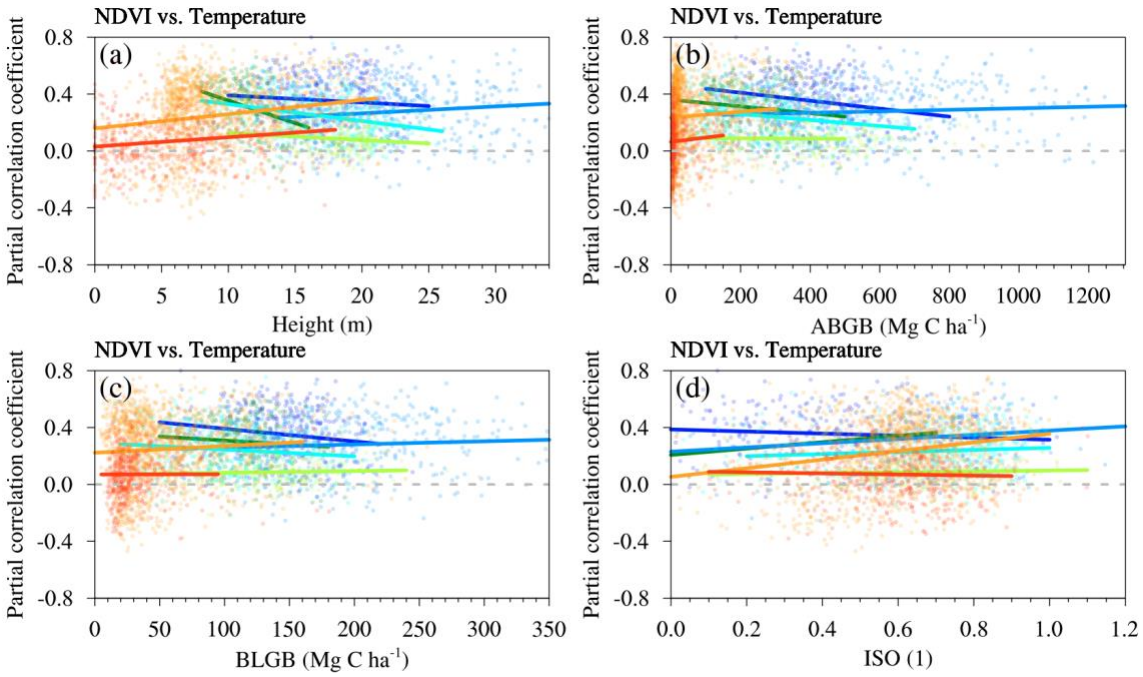

Figure 2.6: Similar to Figure 2.4 but for the PCCs of NDVI-temperature.

2.4 DISCUSSION AND CONCLUSIONS

Precipitation has positive effects on vegetation greenness (i.e., NDVI) for arid ecosystems (i.e., grass and open shrub) and negative effects on humid ecosystems (e.g., forests) in the study region. Overall, VPD has negative correlations with vegetation greenness, but the temperature has positive effects on vegetation greenness. These hydroclimatic factors are expected to impose more challenging conditions for vegetation greenness under climate change. The western US has experienced severe and persistent drought in the past decades (Williams et al., 2020). Future aridity and drought are expected to increase in the American Southwest and Central Plains (Cook et al., 2015; Ukkola et al., 2020). These arid ecosystems and humid forest ecosystems will be threatened by decreasing water supply. Besides, the sharp increase of VPD after the late 1990s induces the stalled or reversed vegetation growth (e.g., leaf area index) globally, and the rising projected VPD is expected to continuously impact the vegetation growth (Yuan et al., 2019) and crop yield (Rigden et al., 2020). Most ecosystems in North America are generally under their optimal temperature (Huang et al., 2019), and hence vegetation growth is positively related to temperature increase. Higher springtime temperatures start the growing season earlier and lead to larger vegetation productivity (Richardson et al., 2020; Zhang et al., 2020). However, these positive effects could decline with the increase of associated extreme events (e.g., extreme hot events, Piao et al., 2014).

Plant hydraulics-related properties affect vegetation's sensitivity to hydroclimatic factors, especially the water availability factor (e.g., precipitation) and the water demand factor (i.e., VPD). Generally, plants with higher values of height and biomass are less sensitive to precipitation and VPD. For the arid ecosystems (i.e., grass), larger biomass probably tends to have more & deeper roots to access more water and, therefore, decreases sensitivity to precipitation and VPD. For the humid ecosystems, larger biomass also

enables more available water access and plant water storage, reducing the VPD's adverse effects on vegetation greenness. Giardina et al. (2018) showed a similar finding that tall Amazonian forests are less sensitive to precipitation variability than shorter forests. But meanwhile, larger biomass of forest ecosystems probably needs more water consumption and consequently reduces the negative impact of precipitation.

Isohydricity is an indirect proxy for plant hydraulic strategy, and shows different influence on the sensitivity of vegetation greenness to hydroclimatic factors for arid and humid ecosystems. More anisohydric plants tend to open stoma longer under dry conditions and could consume more water if available. Therefore the vegetation greenness of the arid grass ecosystem is more positively correlated to precipitation. Meanwhile, anisohydric plants tend to expose longer under a dry atmosphere, and hence vegetation greenness is more negatively sensitive to VPD. Compared with the isohydric humid ecosystem, anisohydric humid ecosystems are more sensitive to VPD than to precipitation. Therefore, the projected rising VPD could have stronger effects than the precipitation on the humid anisohydric ecosystem. For the arid grass ecosystem, the vegetation greenness of anisohydric ecosystems is equally sensitive to precipitation and VPD. Instead, Konings et al. (2017a) found that the sensitivity of NDVI to precipitation is smaller than the sensitivity to VPD for more anisohydric grasslands. These different patterns for grass ecosystems could be because our analysis focuses on a longer and more general condition with both drought and wet years, but Konings et al. (2017) focused on drought years when water is more limited.

Our study highlights the importance of plant hydraulics-related properties on the coupling strength between vegetation greenness and hydroclimatic factors (i.e., VPD and precipitation). Most current Earth system models (ESMs) do not explicitly represent the plant hydraulic processes without considering the plant hydraulic strategies in leaves,

xylem, and roots (Li et al., 2020; Konings et al., 2017a). Liu et al. (2020) show that plant hydraulics can improve the response of evapotranspiration under the stress of VPD and soil moisture compared with approaches commonly used in Earth system models. Plant hydraulics are increasingly represented in large-scale models (e.g., the Noah-MP-PHS, Li et al., 2020; PHS in CLM5, Kennedy et al., 2019). Such models, along with hydraulic trait-based vegetation representation, can help improve carbon and water fluxes simulations, particularly in cases of water stress conditions.

2.5 SUPPLEMENTARY

Value	Name	Short name	Description
0	Water	WTR	At least 60% of area is covered by permanent water bodies.
1	Evergreen Needleleaf forest	ENF	Dominated by evergreen conifer trees (canopy >2m). Tree cover > 60%.
2	Evergreen Broadleaf forest	EBF	Dominated by evergreen broadleaf and palmate trees (canopy > 2m). Tree cover > 60%.
3	Deciduous Needleleaf forest	DNF	Dominated by deciduous needleleaf (larch) trees (canopy >2m). Tree cover > 60%.
4	Deciduous Broadleaf forest	DBF	Dominated by deciduous broadleaf trees (canopy >2m). Tree cover > 60%.
5	Mixed forest	MF	Dominated by neither deciduous nor evergreen (40–60% of each) tree type (canopy >2m). Tree cover > 60%.
6	Closed shrublands	CS	Dominated by woody perennials (1-2m height) > 60% cover.
7	Open shrublands	OS	Dominated by woody perennials (1-2m height) 10–60% cover.
8	Woody savannas	WS	Tree cover 30-60% (canopy > 2m).
9	Savannas	SAV	Tree cover 10-30% (canopy > 2m).
10	Grasslands	GRS	Dominated by herbaceous annuals (< 2m).
11	Permanent wetlands	PWT	Permanently inundated lands with 30-60% water cover and > 10% vegetated cover.
12	Croplands	CRP	At least 60% of area is cultivated cropland.
13	Urban and built-up	UBN	At least 30% impervious surface area including building materials, asphalt, and vehicles.
14	Cropland/Natural vegetation mosaic	NVM	Mosaics of small-scale cultivation 40-60% with natural tree, shrub, or herbaceous vegetation.
15	Snow and ice	SNW	At least 60% of area is covered by snow and ice for at least 10 months of the year.
16	Barren or sparsely vegetated	BRN	At least 60% of area is non-vegetated barren (sand, rock, soil) areas with less than 10% vegetation.

Table 2.2: MODIS-International Geosphere-Biosphere Programme (IGBP) legend and class descriptions (Sulla-Menashe and Friedl, 2018).

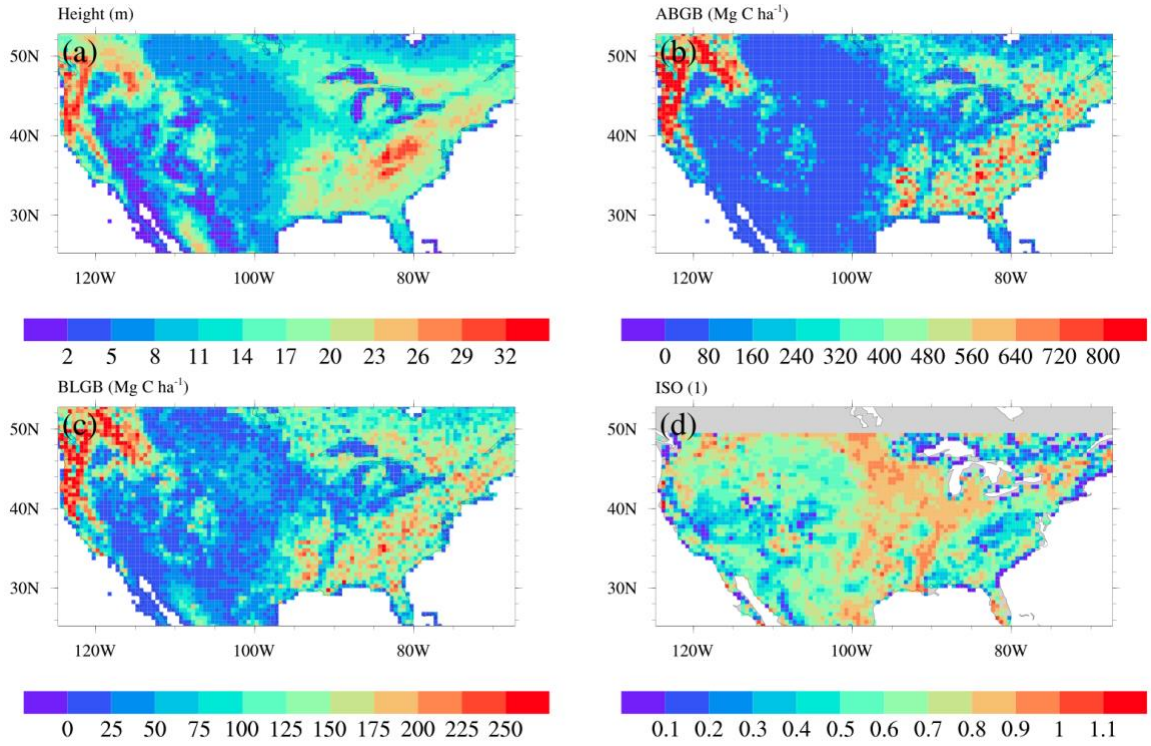

Figure 2.7: Plant hydraulics-related properties (a) canopy height, (b) above ground biomass, (c) below ground biomass, and (d) isohydricity.

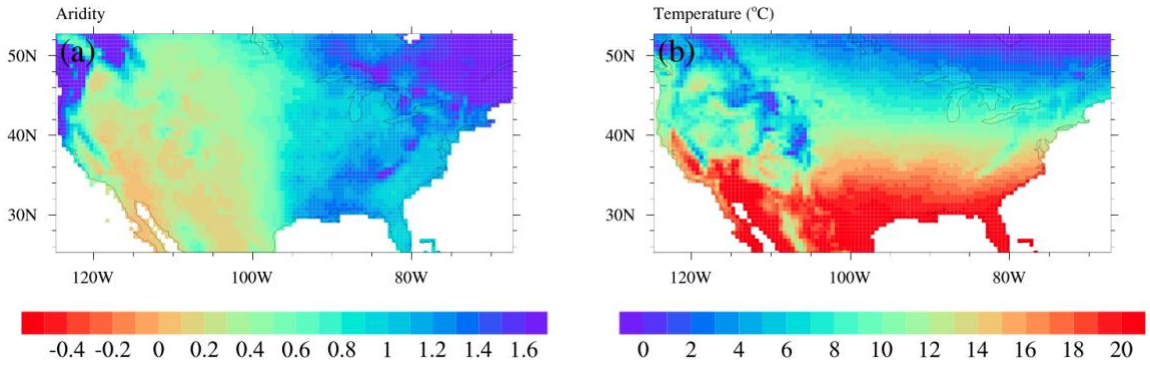

Figure 2.8: (a) Aridity index and (b) mean annual temperature.

Chapter 3: Development of Plant Hydraulics in the Noah-MP Land Surface Model

ABSTRACT

Plants are expected to face increasing water stress under future climate change. Most land surface models, including Noah-MP, employ an idealized "big-leaf" concept to regulate water and carbon fluxes in response to soil moisture stress through empirical soil hydraulics schemes (SHSs). However, such schemes have been shown to cause significant uncertainties in carbon and water simulations. In this paper, we present a novel plant hydraulics scheme (PHS) for Noah-MP (hereafter, Noah-MP-PHS), which employs a big-tree rather than big-leaf concept, wherein the whole-plant hydraulic strategy is considered including root-level soil water acquisition, stem-level hydraulic conductance and capacitance, and leaf-level isohydricity and hydraulic capacitance. Evaluated against plot-level observations from the University of Michigan Biological Station and compared with the default Noah-MP, Noah-MP-PHS better represents plant water stress and improves water and carbon simulations, especially during periods of dry soil conditions. Additional improvements include the simulation of the asymmetrical diel cycles of transpiration and gross primary production under low soil moisture conditions, with higher fluxes in the morning than in the afternoon. Noah-MP-PHS is able to reproduce different patterns of transpiration, stem water storage and root water uptake during a two-week dry-down period for two species with contrasting plant hydraulic behaviors, i.e., the "cavitation risk-averse" red maple and the "cavitation risk-prone" red oak. Sensitivity experiments with plant hydraulic capacitance show that the stem water storage enables nocturnal plant water recharge and provides an important buffer to relieve xylem hydraulic stress during dry soil conditions.

3.1 INTRODUCTION

Transpiration by plants is the dominant component of total terrestrial evapotranspiration (Jasechko, 2013; Schlesinger et al., 2014; Good et al., 2015). This process couples the water and carbon cycles and controls surface energy partitioning, thus playing a principal role in land surface and atmosphere/climate feedbacks (Bonan et al., 2008; Matheny et al., 2014a). A warming climate is expected to intensify the global hydrological cycle and induce more frequent and severe droughts (Dai 2013; Li et al., 2020). Rising temperatures will likewise cause an increase in atmospheric vapor pressure deficit (Grossiord et al., 2020). Plants, therefore, are expected to face more hydroclimatic stresses due to decreasing soil water supply alongside increasing atmospheric demand (McDowell et al., 2008; Anderegg et al., 2012; Anderegg et al., 2018). It is crucial to understand and simulate the dynamics of transpiration in order to better predict ecosystem–atmosphere feedbacks in water, carbon, and energy exchange (Bonan et al., 2008; Allen et al., 2010; Choat et al., 2012; Sperry et al., 2016; Lemordant et al., 2018).

As a key component of Earth system models (ESMs), land surface models (LSMs) simulate water, carbon and energy fluxes, and are used for drought/flood prediction, weather forecasts, and climate prediction (Yang et al., 2011; Bonan & Doney et al., 2018). The majority of LSMs use an idealized "big leaf" to represent all vegetation functions as a single leaf or a pair of leaves (sunlit and shaded) (Luo et al., 2018). Within the big-leaf framework, LSMs do not resolve water-state variables within plants and therefore do not have the ability to explicitly represent the plant water-stress status. Therefore, most LSMs typically parameterize the effects of soil water stress on vegetation and thus surface fluxes (i.e., water, carbon and energy fluxes) using empirical functions based on either soil water content or soil water potential (Egea et al., 2011; Verhoef & Egea, 2014; Powell et al., 2013; Sitch et al., 2015). These traditional schemes, which we refer to as soil hydraulics

schemes (SHSs), depend on soil hydraulic properties and a few plant functional related parameters (e.g., root distribution), but the role of plant traits (e.g., xylem conductivity) in controlling transpiration is largely ignored (Christoffersen et al., 2016). Many such models are satisfactory when soil moisture is adequate for transpiration, but most are unable to simulate water and carbon fluxes well under water-limited conditions (e.g., Calvet et al., 1998; Grant et al., 1999; Tuzet et al., 2003). Additionally, these LSMs fail to capture the asymmetry of daytime water and carbon fluxes under conditions of low soil moisture content, resulting in underestimation (overestimation) of fluxes in the morning (afternoon) (Matheny et al., 2014a; Tuzet et al., 2003). Therefore, SHS functions have been shown to contribute significant uncertainty to water and carbon simulations by LSMs (Dirmeyer et al., 2006; Niu et al., 2011; Trugman et al., 2019a; Kennedy et al., 2019).

Transpiration is regulated dynamically through the stomatal aperture, which, in many cases, is governed by water status and plant hydraulic properties (Sperry, 2000; Buckley 2005; Skelton et al., 2015; Matheny et al., 2017; Anderegg et al., 2018). Water movement through plant vascular systems is regulated by the whole-plant hydraulic strategy, which is the culmination of emergent phenotypical hydraulic functional traits at the leaf, stem, and root levels (Matheny et al., 2017; McCulloh et al., 2019). At the leaf level, there are two opposing strategies for the regulation of stomatal openness in facing water stress: isohydricity, in which plants readily close stomata to maintain a steady and high leaf water potential (LWP) and conserve water; and anisohydricity, in which plants maintain open stomata longer while incurring highly negative LWP to maximize carbon uptake. Most plants operate along a range of intermediate strategies between these two extremes (McDowell et al., 2008; Skelton et al., 2015; Blackman 2018; Zhu et al., 2018). At the stem level, plants differ in their xylem architecture, including ring-porous, diffuse-porous, and tracheid-based types (Oren et al., 1999; Matheny et al., 2017). The diversity of

xylem architecture and physiology alongside numerous other vessel traits (e.g., vessel diameter, density and interconnectedness) determine xylem hydraulic functioning and its resistance to hydraulic impairment (cavitation) (Pockman & Sperry, 2000; Choat et al., 2012). The ability of a plant to store water, or its hydraulic capacitance, likewise plays a critical role in regulating the water status and tree function on time scales ranging from diel to seasonal (Matheny et al., 2015; Matheny et al., 2017; Yan et al., 2020). Plant hydraulic control also results from the properties of root systems and the rhizosphere, such as rooting depth and vertical distribution, lateral extent and competitive dynamics, fine root area, water extraction efficiency, mycorrhizal interactions, and hydraulic redistribution (Canadell et al., 1996 & 2007; Allen, 2009; Reichstein et al., 2014; Wullschleger et al., 2014). The incorporation of a holistic, whole-plant hydraulic strategy in place of the more traditional semi-empirical SHS approach, along with hydraulic trait-based vegetation representation, can serve to improve simulations of carbon and water fluxes, particularly in cases of drought and other disturbances (Christoffersen et al., 2016; Mirfenderesgi 2019; Kennedy et al., 2019).

Mechanistic modeling of plant hydraulics has advanced in recent decades and shown clear evidence of providing a better representation of the vegetative regulation of global carbon and water fluxes (Anderegg and Martin, 2020; McDowell et al., 2019; Mencuccini et al., 2019; Anderegg et al., 2018; Mackay et al., 2015; Hunt et al., 1991). There are three broad categories of plant hydraulics models, although all vary in their parameterization and implementation (see section 2.2 for details). The first category of model is the pipe model (PPM), which treats the water movement within vascular conduits as laminar flow through pipes (Shinozaki et al., 1964a & 1964b; McCulloh et al., 2003; Lehnebach et al., 2018). A PPM commonly simulates water flow based on the Hagen–Poiseuille law and allometric scaling laws, and is typically applied in tree-level simulations

(Roderick and Berry, 2001; Savage et al., 2008; Mrad et al., 2018). The second category is the electrical analogy model (EAM), which conceptualizes water flow through plants as being analogous to the current through an electric circuit with series of resistance and/or capacitance (Sperry et al., 1998). The third category is the porous media model (PMM), which assumes that water movement through interconnected tracheids or xylem vessels resembles porous media flow (Chuang et al., 2006; Bohrer et al., 2005). PMMs can describe in detail the spatiotemporal dynamics of a tree's hydraulic system, but at the cost of substantial computational and parametric demands. Among these three types, EAMs require relatively few parameters and have low computational demands, making them easier to apply within large-scale simulations.

Given the advancements in theory development, physical-based models, and data availability (e.g., in-situ plant hydraulic traits and vegetation water status–related remote sensing observations), mechanistic representations of plant hydraulic process are increasingly being incorporated into LSMs to improve water and carbon simulations (Hickler et al., 2006; Luo et al., 2013; Christoffersen et al., 2016; Kennedy et al., 2019; Yan et al., 2020; Eller et al., 2020). It should be pointed out that one of the earliest examples for considering plant hydraulics in LSMs dates back to the work of Sellers et al. (1986); they employed the term "leaf water potential" in describing their Simple Biosphere (SiB) model for use within general circulation models, although SiB did not account for stem hydraulic capacitance. Recent examples include the Community Land Model, version 5 (CLM5; Kennedy et al., 2019) and the Joint UK Land Environment Simulator (Eller et al., 2020). However, relatively few new LSMs consider the whole-plant hydraulic strategy and include an explicit representation of plant hydraulic capacitance. In this paper, we present a novel EAM-type plant hydraulics scheme (PHS; Williams et al., 1996; Xu et al., 2016) for land surface modeling within the community Noah land surface model with

multiparameterization options (Noah-MP) (Niu et al., 2011; Yang et al., 2011). Noah-MP is a primary model employed in the NASA Land Information System (Kumar et al., 2006), the next phase North American Land Data Assimilation System (Xia et al., 2012), the Weather Research and Forecasting model (Skamarock et al., 2019), and the National Water Model (Cosgrove et al., 2016). Noah-MP is also widely used for operational weather and climate predictions (e.g., NOAA/National Centers for Environmental Prediction). In this paper, we hypothesize that:

1. By implementing plant hydraulics theory, the new PHS can better represent plant water stress during dry soil conditions and correspondingly improve water and carbon simulations.

2. PHS can capture the asymmetrical diel cycles, with higher fluxes in the morning than the afternoon, of transpiration and gross primary production under conditions of low soil moisture content.

3. Parameterization schemes used within PHS can replicate different hydraulic behaviors between species with different hydraulic strategies (i.e., isohydric vs. anisohydric).

4. Plant hydraulic capacitance within PHS will enable nocturnal plant water recharge and help relieve xylem hydraulic stress. Plant hydraulic capacitance also plays a vital role in water and carbon simulations during soil moisture dry-down periods.

Section 2 describes the default SHSs of the host model (i.e., Noah-MP), reviews commonly used plant hydraulics models, and introduces an appropriate PHS for use in Noah-MP. Section 3 presents the datasets and experimental design. Model simulation results are examined in Section 4, followed by conclusions and discussion in Section 5.

3.2 MODEL DESCRIPTION

3.2.1 Traditional soil hydraulics scheme in Noah-MP

Noah-MP is used as the baseline model, in which the plant water stress factor (β) represents the effect of water stress on plant water and carbon fluxes. There are three default β schemes available within Noah-MP. These schemes are all empirical functions based on either soil moisture or soil water potential (Niu et al., 2011). We reference these default schemes as SHSs (see Figure 3.1a). β is used to regulate the stomatal conductance, through net photosynthesis in the Ball–Berry-type stomatal resistance scheme (Niu et al., 2011). Transpiration is calculated, which is directly deducted from the root zone soil moisture.

Transpiration (TR in Eq. 3.1 and subsequent equations) water extraction is partitioned into the root water uptake (Q_i) from the ith root zone soil layer,

$$Q_i = \frac{r_i \cdot w_i}{\beta} \cdot \mathrm{TR}, \qquad \text{(Eq. 3.1)}$$

where β is calculated as the root ratio (r_i) weighted average of the soil layer wilting factor (w_i) among N_r soil layers:

$$\beta = \sum_{i=1}^{N_r} r_i \cdot w_i, \qquad \text{(Eq. 3.2)}$$

Three default SHSs have different parameterizations for w_i ($0 \le w_i \le 1$):

(1) The Noah-type SHS (Chen and Dudhia, 2011) is represented as a function using soil moisture ($\theta_{\mathrm{liq},i}$),

$$w_i = \frac{\theta_{\mathrm{liq},i} - \theta_{\mathrm{wilt}}}{\theta_{\mathrm{ref}} - \theta_{\mathrm{wilt}}}, \qquad \text{(Eq. 3.3)}$$

where θ_{wilt} and θ_{ref} (units: m3/m3) are soil moisture at the wilting point and a reference soil moisture at field capacity, respectively.

(2) The CLM-type SHS (Oleson et al., 2004; Yang and Dickinson, 1996) depends on a function using soil matric potential,

$$w_i = \frac{\psi_{\text{wilt}} - \psi_i}{\psi_{\text{wilt}} - \psi_{\text{sat}}} \quad \text{(Eq. 3.4)}$$

where $\psi_i = \psi_{\text{sat}} \cdot (\frac{\theta_{\text{liq},i}}{\theta_{\text{sat}}})^{-b}$ is the matric potential of the soil layer i, ψ_{sat} is the saturated matric potential, and ψ_{wilt} is the soil matric potential reaching the wilting point.

(3) The SSiB-type SHS (Xue et al., 1991) is also based on soil matric potential:

$$w_i = 1 - e^{-c_2 \ln(\psi_{\text{wilt}}/\psi_i)} \quad \text{(Eq. 3.5)}$$

where c_2 is a slope factor ranging from 4.36 for crops to 6.37 for broadleaf shrubs.

3.2.2 Plant hydraulics model

Here, we briefly introduce the commonly used models for plant hydraulics processes (Table 3.1). There are three broad categories of plant hydraulics modeling strategies (Mencuccini et al., 2019; McDowell et al., 2019):

(1) PPMs treat the water movement within vascular conduits as laminar flow through pipes (Shinozaki et al., 1964a & 1964b; McCulloh et al., 2003; Lehnebach et al., 2018). These idealized vertical, parallel pipes can be either connected or disconnected from adjacent pipes depending on model assumptions. The flow through each pipe is commonly simulated by the Hagen–Poiseuille law (Roderick and Berry, 2001; Mrad et al., 2018). Some of these models (e.g., the WBE model; West et al., 1999; Savage et al., 2008) use additional allometric scaling laws to describe vascular architecture, such as conduit taper, and further consider hydraulic trade-offs (e.g., the Botanical Network Model; Savage et al., 2010). The network model proposed by Mrad et al. (2018) based on xylem anatomy and simulates lateral embolism spread, providing another solution to further explore xylem tissue hydraulic behavior and vulnerability to cavitation.

(2) EAMs conceptualize water flow through plants as being analogous to the current through an electric circuit with series of resistance and/or capacitance (Sperry et al., 1998). An EAM is based on an ordinary differential equation and has high

computational efficiency. EAMs have two subcategories: resistor model (RMs) and resistance–capacitance models (RCMs). An RM regards plant hydraulics as a resistor (or a series of resistors) to transport water flow. Sellers et al. (1986) proposed an RM in the SiB model, which included two resistors: averaged plant vascular resistance and soil-root resistance. Other examples include the plant hydraulics schemes developed by Sperry et al. (1998), the SOX scheme developed by Eller et al. (2018), and the PHS scheme in CLM5 (Kennedy et al., 2019). Besides the resistor, RCMs also consider plant-water storage or capacitance, e.g., the schemes developed by Sperry et al. (1998), Steppe et al. (2006), Gentine et al. (2016), and Xu et al. (2016). The hydraulic capacitance, especially for large trees, has been demonstrated by field observation to play a critical role in regulating transpiration at both short- and long-term scales (Matheny et al., 2015; Matheny et al., 2017; Yan et al., 2020).

(3) PMMs assume that water movement through interconnected tracheids or the xylem resembles porous media flow (Chuang et al., 2006; Bohrer et al., 2005). A PMM typically uses the Richards equation for non-saturated porous media flow, which combines the continuity equation with Darcy's law, leading to a nonlinear partial differential equation. Therefore, these models can describe in detail the spatiotemporal dynamics of a tree's hydraulic system, but at the cost of substantial computational and parametric demands. The architecture of PMMs ranges from single beam (stem only) models (Chuang et al., 2006; Mirfenderesgi et al., 2016 & 2019; Yan et al., 2020), to the FETCH model with a three-dimensional stem and branch structure (Bohrer et al., 2005), to the Xylem Water Flow (XWF) model including root, stem, and branches (Janott et al., 2011; Bittner et al., 2012).

Compared with PPMs and PMMs, EAMs require relatively few parameters and low computational demand. Therefore, they are highly suitable for use within LSMs or ESMs

on a large spatial scale. In particular, RCMs consider the whole-plant hydraulic strategy as well as plant water storage, which is promising for use in LSMs.

	Plant hydraulics model type			
	Pipe model	Electric analogy model		Porous media model
		Resistor model	Resistor-capacitance model	
Vascular architecture assumption	Series of pipes	Electric circuit with resistance	Electric circuit with resistance and capacitance	Continuous porous media
Storage inclusion	Yes/No	No	Yes	Yes
Governing law or equation	Hagen–Poiseuille law, allometric scaling laws	Darcy's law		Richards equation
Typical model scale	Tissue level, tree level, ecosystem level	Tree level, cohort level, stand level, ecosystem level		Tree level, cohort level
Computational demand	Moderate to high	Low to moderate		High
Example of evaluation data	Tree-level measurements	Sap flux, flux-tower data, ecosystem-scale data		Sap flux
Parameterization required	Many parameters	Some parameters		Many parameters
Examples	1. Pipe Model (Shinozaki et al., 1964a & b) 2. WBE (West et al., 1999) 3. Stem Hydraulic Model (Roderick and Berry, 2001) 4. Botanical Network Model (Savage et al., 2010) 5. Network Model (Mrad et al., 2018) 6. Pipe Model in HOTTER (Trugman et al., 2019b)	1. SiB (Sellers et al., 1986) 2. SPA (Sperry et al., 1998) 3. TREES (Mackay et al., 2011) 4. SOX (Eller et al., 2018) 5. PHS in CLM5 (Kennedy et al., 2019)	1. SPA (Williams et al., 1996) 2. Dynamic Flow and Storage Model (Steppe et al., 2006) 3. VIC+ (Luo et al., 2013) 4. ED2-Hydro (Xu et al., 2016) 5. RCL Model (Zhuang et al., 2014)	1. PM (Chuang et al., 2006) 2. FETCH (Bohrer et al., 2005) 3. TFS v.1-Hydro (Christoffersen et al., 2016) 4. XWF (Janott et al., 2011)

Table 3.1: Commonly used plant hydraulics models and their key features.

3.2.3 Plant hydraulics scheme for Noah-MP

We present a novel RCM-type PHS for use in Noah-MP based primarily on the works of Xu et al. (2016) and Williams et al. (1996). Our PHS is an EAM and similar to those that have been shown to perform well in previous studies (Xu et al., 2016). In particular, this PHS considers plant water storage in the stem and leaves. The internal plant water storage plays key roles in regulating the water economy and tree function on time

scales ranging from diel to seasonal (Yan et al., 2020), by maintaining daily transpiration, buffering drought impacts on xylem embolism and consequent hydraulic failure, supporting leaf growth in the dry season for seasonally deciduous trees, and so on (Goldstein et al., 1998; Meinzer, 2003; Huang et al., 2017).

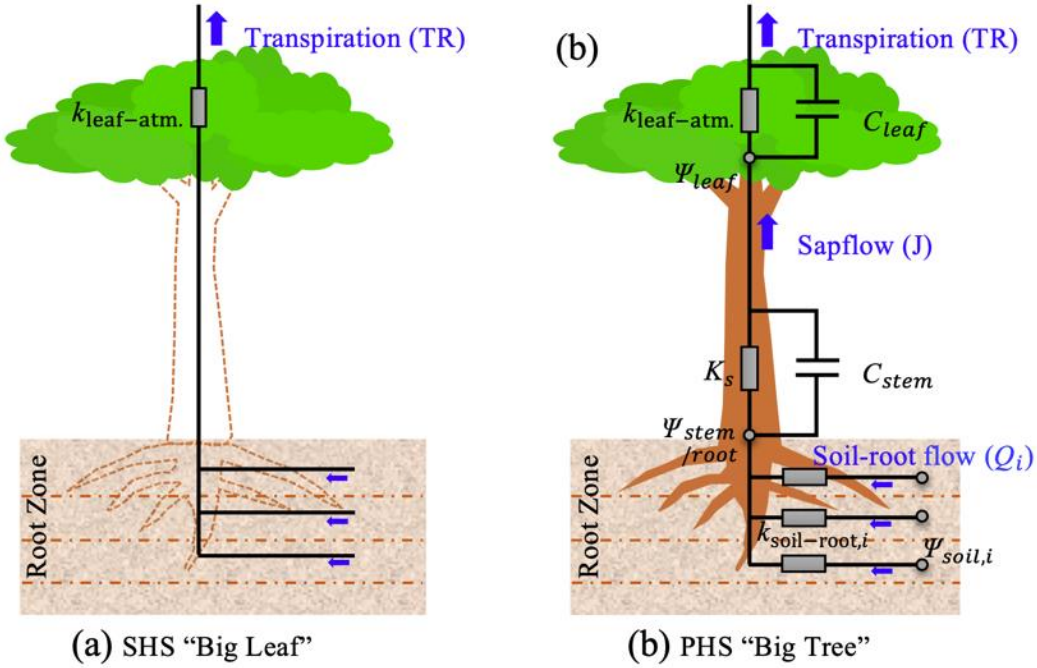

Figure 3.1: (a) Schematic representation of a traditional "big leaf" scheme. Such models assume leaves can directly access soil water from the root zone, distributing transpiration based on the wilting factor (Eq. 3.2) at each root zone layer. (b) Schematic representation of the plant hydraulics scheme, with physical representation of roots, stem, and leaf, separately. $k_{\text{leaf–atm.}}$ denotes the conductance from leaf to canopy air, consist of leaf boundary conductance and stomatal conductance.

The governing equations of the PHS are primarily based on the conservation of mass and Darcy's law, describing the relationships between plant water potential and plant water storage, plant water potential and hydraulic conductance, LWP, and plant water stress dynamics. Details are provided in the following subsections (2.3.1–2.3.4).

3.2.3.1 Water flux from soil to root

Water flux (Q_i, units: mm/s) from soil to root within each soil layer i of the root zone is driven by the water potential gradient between root water potential and soil matric potential ($\Psi_{\text{soil},i}$, units: mm). For simplicity, the roots and stem are directly linked as one component at the base of the stem (Figure 3.1b). Root water potential within each soil layer drives the stem water potential (Ψ_{stem}, units: mm) at the ground surface. Soil-to-root water flux in the ith layer is calculated following Darcy's law:

$$Q_i = k_{\text{soil-root},i} \times (\Psi_{\text{soil},i} - \Psi_{\text{stem}} - \Psi_{s,i}) \quad \text{(Eq. 3.6)}$$

$$Q = \sum Q_i \quad \text{(Eq. 3.7)}$$

where Q is the total water flux calculated as the sum of water flux at each layer Q_i (units: mm/s); and $\Psi_{s,i}$ (units: mm) represents the specific gravitational water potential drop from soil layer i to the base of the stem, and is equals to the depth from the center of the soil layer i to the ground ($h_{s,i}$, units: mm). Symbol $k_{\text{soil-root},i}$ (units: s^{-1}) is the hydraulic conductance from soil to root at layer i and is calculated following Katul et al. (2003):

$$k_{\text{soil-root},i} = K_{\text{soil,sat}} \times \left(\frac{\theta_{\text{liq},i}}{\theta_{\text{sat}}}\right)^{2b+3} \times \frac{\sqrt{\text{RAI}_i}}{\pi \times d_i} \quad \text{(Eq. 3.8)}$$

where $K_{\text{soil,sat}}$ is the hydraulic conductance at saturation, $\theta_{\text{liq},i}$ represents the volumetric soil moisture in the ith layer, θ_{sat} is the volumetric soil moisture at saturation, and d_i is the depth of the ith soil layer.

Soil water potential $\Psi_{\text{soil},i}$ (units: mm) is calculated based on Clapp & Hornberger (1978):

$$\Psi_{\text{soil},i} = \Psi_{\text{soil},sat} \times \left(\frac{\theta_{\text{liq},i}}{\theta_{\text{sat}}}\right)^{-b} \quad \text{(Eq. 3.9)}$$

where b is an empirical factor determined by soil texture.

The root area index RAI_i in soil layer i is based on the root fraction r_i multiplied by the total root area (RAI) (Kennedy et al., 2019), which is the sum of the stem area index (SAI) and leaf area index (LAI), multiplied by the root-to-shoot ratio ($f_{\text{root-shoot}}$):

$$\mathrm{RAI}_i = f_{\mathrm{root-shoot}} \cdot (\mathrm{LAI} + \mathrm{SAI}) \cdot r_i. \quad \text{(Eq. 3.10)}$$

In this paper, hydraulic redistribution is prevented by setting Q_i as 0 if the soil water potential in the ith layer is lower than the root water potential.

3.2.3.2 Water flux from stem to leaf

Sap flux from the base of the stem to the leaf J (units: mm/s) is computed based on Darcy's law and is dependent on the xylem hydraulic conductivity K_s (units: mm/s), sapwood area index S_{sap} (sapwood area per ground area, units: m^2/m^2), and plant canopy height h_c (units: mm):

$$J = \frac{\mathrm{K}_s \times S_{\mathrm{sap}} \times (\Psi_{\mathrm{stem}} - \Psi_{\mathrm{leaf}} - \Psi_c)}{a_1 \cdot \mathrm{h}_c} \quad \text{(Eq. 3.11)}$$

where Ψ_{leaf} (units: mm) is the LWP, Ψ_c (units: mm) represents the specific gravitational water potential drop from the ground to the canopy (i.e., h_c), $a_1 \cdot h_c$ represents the length of the water flow route, and a_1 is an empirical parameter;

$$\mathrm{K}_s = \mathrm{K}_{s,\mathrm{sat}} \times \left[1 + \left(\frac{\Psi_{\mathrm{stem}}}{P_{50}}\right)^{a_2}\right]^{-1} \quad \text{(Eq. 3.12)}$$

where $K_{s,\mathrm{sat}}$ (units: mm/s) denotes the saturated xylem hydraulic conductivity, P_{50} is the stem water potential at 50% loss of conductivity, and a_2 is an empirical parameter.

3.2.3.3 Update of the water potential

The changes in the leaf and stem water storages leads to the changes of the leaf and stem water potentials,

$$\frac{d\Psi_{\mathrm{stem}}}{dt} = \frac{Q - J}{C_{\mathrm{stem}} \times V_{\mathrm{sap}}} \quad \text{(Eq. 3.13)}$$

$$\frac{d\Psi_{\mathrm{leaf}}}{dt} = \frac{J - \mathrm{TR}}{C_{\mathrm{leaf}} \times \mathrm{LAI}} \quad \text{(Eq. 3.14)}$$

where dt (units: s) is the calculation time step; C_{leaf} (unitless) and C_{stem} (units: m^{-1}) are the leaf and stem water capacitances, respectively; and LAI (units: m^2/m^2) and V_{sap} (units: m^3/m^2) are the leaf area index and sapwood volume index, respectively.

3.2.3.4 Calculation of plant water stress

LWP is used to formulate the plant water stress (β) with higher fidelity (Xu et al., 2016):

$$\beta = [1 + (\frac{\psi_{\text{leaf}}}{\text{TLP}})^{a_3}]^{-1} \quad \text{(Eq. 3.15)}$$

where TLP (units: mm) is the turgor loss point, i.e., the LWP when the photosynthetic capacity rate halves, and a_3 is an empirical parameter. These PHS parameters are summarized in Table 3.2. is a.

	Parameter	Description	Units
Leaf	TLP	Turgor loss point (LWP when photosynthetic capacity rate halves)	mm
	C_{leaf}	Leaf water capacitance	1
	a_3	Empirical parameter controlling plant water stress	unitless
Stem (xylem)	$K_{s,\text{sat}}$	Sapwood-area-specific saturated xylem hydraulic conductivity	mm/s
	P_{50}	Stem water potential at 50% loss of conductivity	mm
	C_{stem}	Stem water capacitance	m^{-1}
	S_{sap}	Specific sapwood area index	m^2/m^2
	V_{sap}	Specific sapwood volume index	m^3/m^2
	h_c	Canopy height	mm
	a_1	Empirical parameter controlling length of water flow route	unitless
	a_2	Empirical parameter controlling xylem hydraulic conductance	unitless
Root	$f_{\text{root-shoot}}$	Fine root area to shoot (i.e., leaf area + stem area) ratio	m^2/m^2
	Root depth	Fine rooting depth (also used in SHSs)	m
	Root ratio	Fine root distribution in root zone each layer (also used in SHSs)	unitless

Table 3.2: Parameters used in the plant hydraulics scheme.

3.3 METHODS

3.3.1 Data

Model evaluation was conducted based on observations from the University of Michigan Biological Station (UMBS) located in Northern Lower Michigan, USA. The annual average precipitation of this site is 805 mm, and its annual mean temperature is near 6.8°C (Matheny et al., 2014b). The soil texture at UMBS is dominated by extremely well-drained spodosols and contains 92% sand, 7% silt, and 1% clay (He et al., 2013). Mean canopy height is approximately 29 m. Fluxes, meteorological forcing, and tree-level and plot-level biological data are available from the AmeriFlux database (site-ID: US-UMB). Observations used in this study include soil moisture (units: $m^3 m^{-3}$; at the depths of 5, 15, 30, 60, 100, 200 and 300 cm), gross primary production (units: μmol CO_2 $m^{-2} s^{-1}$), and sap flux. Matheny et al. (2014b) scaled measured values of tree-level sap flux to the equivalent plot-level sap flux with good agreement. Here, we use the sap flux as a proxy of transpiration. It should be noted that, commonly, there is a time lag between sap flux and transpiration, typically on the order of 30 to 90 mins. We adjusted the sap flux time series to match its peak with the peak of the net radiation based on half-hourly data for each day.

Tree-level measurements were also used to evaluate our tree-level simulations. Matheny et al. (2016) found that during an inter-storm dry period (day of year (DOY) 211–224 in 2014), red maple (*Acer rubrum*) sap flux and stem water storage were strongly reduced, while red oak (*Quercus rubra*) water fluxes were only slightly affected. The diverging hydraulic strategies between red oak (deep root structure, large xylem vessels, anisohydric) and red maple (shallow root mat, small xylem vessels, isohydric) provide an ideal experiment to test our newly developed PHS. LWP was measured in canopy-top

leaves exposed to full sun of mature red oak and red maple trees using a pressure chamber (Model 600 PMS Instrument Co., Corvallis, OR, USA; see details in Matheny et al., 2016). LWP measurements were made at roughly 06:00 (dawn), 13:30 (noon), and 16:00 (afternoon) from June 23 to July 12, 2014 (DOY 174–193). Stem water storage and sap flux were continuously monitored in one mature, canopy-dominant individual of each species (i.e., one red oak and one red maple) in 2014 (Matheny et al., 2016). Sap flux was also adjusted to match the peak of net radiation. The canopy height, crown area, and sapwood area for the red maple (oak) tree are 27.4 (31.3) m, 40.1 (50.1) m^2, and 252.3 (342.3) cm^2, respectively.

The model soil hydraulic properties and root vertical distribution were set based on site observations. Soil hydraulic parameters were derived from pedotransfer functions (Saxton et al. 1986) using the percentages of sand, silt, and clay (92%, 7%, and 1%) for our plots (He et al., 2013). Specifically, we set the soil moisture at the wilting point as 0.033 m^3/m^3, the reference soil moisture at field capacity as 0.099 m^3/m^3, and the soil porosity as 0.265 m^3/m^3.

By default, the fine root ratio at each layer is proportional to the soil layer thickness (i.e., 10 cm, 30 cm, 60 cm, and 100 cm for the 1^{st}–4^{th} soil layer), i.e., evenly distributed fine root density at each layer (i.e., 0.05, 0.15, 0.3, 0.5 for the 1^{st}–4^{th} layer). Instead, we updated the fine root ratio based on the fine root biomass measurements at UMBS (He et al., 2013). The updated root ratios are 0.316, 0.465, 0.196 and 0.023 for the 1^{st} to 4^{th} layer, respectively (the oak simulation used a different set of root ratios; see details below).

3.3.2 Plot-level and tree-level experiments

We conducted plot-level simulations about 180 ha in area and comprising 99% of the flux footprint of the US-UMB flux tower, to evaluate the newly developed PHS (Table 3.3). The upscaled sap flux (i.e., transpiration) and flux tower GPP were used to evaluate model performance and explore whether PHS could improve water and carbon simulations. We focus on the growing season of 2013–2014 (DOY 153–262 in 2013 and 191–257 in 2014).

Red maple and red oak are two codominant mid-successional tree species at UMBS. Red maple favors a "cavitation risk-averse" hydraulic strategy, while red oak employs a "cavitation risk-prone" hydraulic strategy. These two species have different hydraulic traits within the roots, xylem, and leaves (Thomsen et al. 2013; Matheny et al., 2014b). Therefore, we have an ideal testbed to evaluate the capabilities of PHS for species with divergent hydraulic strategies. We conducted tree-level simulations for a red oak tree and a red maple tree based on tree-level measurements of transpiration and stem water storage. We focused only on the plant hydraulics process and constrained the simulations using observed soil moisture. Matheny et al. (2016) suggested that red maple predominantly uses shallow water sources, while red oak can use a deeper and less variable water source. Fan et al. (2007) summarized that the measured average rooting depth for maple and oak is 1.75 m and 5.23 m, respectively. Therefore, for the red maple simulation, we kept the same rooting depth and root ratios as the plot-level simulation. But for the oak simulation, we set a deeper rooting depth (as 10 m), and the root ratios were based on the vertical fine root measurements of mixed pedunculate oak and sessile oak from Bréda et al. (1995). To mimic the oak using deeper water sources, we calibrated a constant soil moisture for the 4_{th} soil layer, considering there was no substantial drought affecting the groundwater during our modeling period.

	Simulation		
	Plot-level	Red maple	Red oak
Period	Growing season in 2013 and 2014	Growing season in 2014	Growing season in 2014
Forcing	Flux tower	Flux tower	Flux tower
Soil moisture	Model simulation	1st–4th layer soil moisture observation constrain	1st–3rd layer soil moisture observation and virtual 4th layer soil water constrains
Soil layer thickness (1st–4th layer)	0.1 m, 0.3 m, 0.6 m, 1.0 m (total: 2 m)	0.1 m, 0.3 m, 0.6 m, 1.0 m (total: 2 m)	0.1 m, 0.3 m, 0.6 m, 9.0 m Totally 10 m
Fine root ratio (1st–4th layer)	0.33, 0.47, 0.18, 0.02 (He et al., 2013)	0.33, 0.47, 0.18, 0.02 (He et al., 2013)	0.22, 0.41, 0.28, 0.09 (Bréda et al., 1995)
Usage of groundwater	No	No	Yes Constant virtual soil moisture at the 4th soil layer

Table 3.3: Model setup for plot-level and tree-level simulations.

3.3.3 Sensitivity experiments of plant capacitance

As described in section 2.2, there are two types of EAM, i.e., RM and RCM, frequently employed for large-scale plant hydraulic modeling. The difference between them is whether they consider the plant hydraulic capacitance. To understand the role of plant water storage on the hydraulic process, we further conducted a series of tree-level sensitivity experiments during the 2014 dry-down period. These experiments applied the same experiment settings as the red maple simulation (see Section 3.3), i.e., the same calibrated parameters and boundary conditions (soil moisture and forcing), but by using a series of stem hydraulic capacitance.

3.3.4 Model calibration

We use the root-mean-square error (RMSE) and the modified Kling–Gupta Efficiency (KGE; Kling et al., 2012) to evaluate model performance. KEG computes the Euclidian distance between the ideal point and three components, including the correlation coefficient (CC), bias ratio (BR), and variability ratio (VR) (see details in Gupta et al., 2009 and Kling et al., 2012).

The key PHS parameters (Table 3.1) were calibrated for the above three experiments, i.e., one plot-level experiment, and two tree-level experiments (the red maple and red oak simulations). For each experiment calibration, we set an ensemble run to optimize the model outputs to match the observations, i.e., plot-level sap flux and GPP for the plot-level simulation, and sap flux and stem water storage of one red maple and one red oak for the tree-level simulation. The calibrated key parameters are shown in Table 3.6.

3.4 RESULTS

3.4.1 Plot-level evaluation

3.4.1.1 Overall model performance

We evaluated four configurations of Noah-MP with different water stress schemes, i.e., the Noah, CLM and SSiB SHS schemes, and the PHS scheme. The calibrated key parameters for PHS are listed in Table 3.6. Figure 3.2 compares the model simulations and observations at the daily time scale, and corresponding statistics are shown in Table 3.4. For the daily transpiration simulation, PHS shows the best performance compared with the three default SHSs, with the lowest RMSE (0.48 vs. 0.60, 0.57 and 0.60 10^{-5} mm/s) and the highest KGE (0.72 vs. 0.62, 0.54 and 0.48), and with particularly strong performance in terms of the CC and VR (see Table 3.7). For the daily GPP simulation, PHS performs better than the default SHSs, with a lower RMSE (2.10 vs. 2.96, 2.44 and 2.59 μmol CO_2

/m2/s) and a higher KGE (0.62 vs. 0.49, 0.54 and 0.48), and again with particularly strong performance in terms of the CC and VR (see Table 3.7). Similarly, PHS also has the best performance for transpiration and GPP at the hourly time scale (Table 3.7 and Figure 3.10). Besides the transpiration and GPP, the PHS-modeled daily soil moisture is better than that simulated

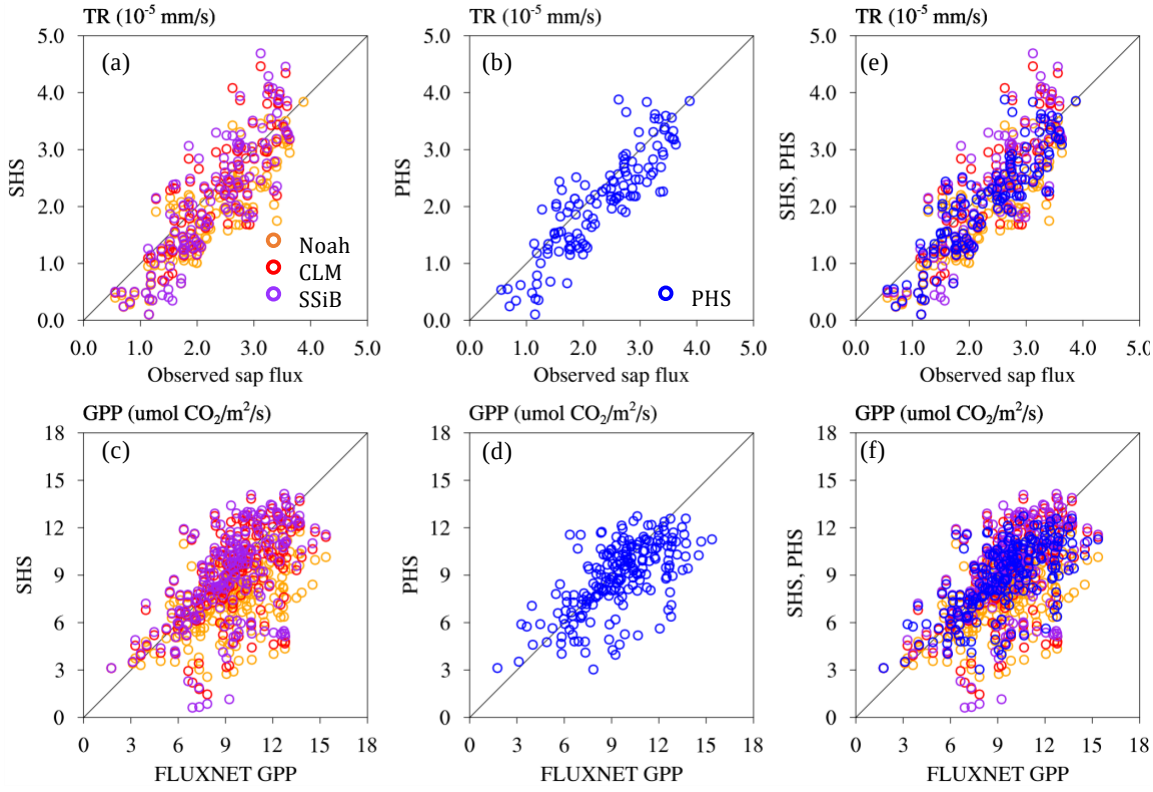

Figure 3.2: Comparison of daily transpiration (TR) (a, b) and GPP (c, d) simulations between SHSs and PHS.

Scheme	Transpiration		GPP	
	RMSE	KGE	RMSE	KGE
Noah	0.60	0.62	2.96	0.49
CLM	0.57	0.54	2.44	0.54
SSiB	0.61	0.48	2.59	0.48
PHS	**0.48**	**0.72**	**2.10**	**0.62**

Table 3.4: Statistics of model performance at the daily time scale (best values are written in bold type).

3.4.1.2 Model performance under different soil moisture

We further analyzed the performance of the models under different soil moisture conditions (Figure 3.3). On each day, we calculated the KGE of different schemes using the hourly data, and then computed the difference of KGE (ΔKGE) between the PHS and each default SHS (i.e., Noah, CLM, SSiB). Finally, we binned the ΔKGE using daily soil moisture observation into eight intervals (i.e., approximately 26 values of ΔKGE in each interval for each comparison between PHS with default SHS). Figure 3.3 shows the ΔKGE under different soil moisture conditions. Positive values indicate that PHS performs better (i.e., higher KGE) than the corresponding SHS. Compared with the Noah scheme, PHS shows better performance under different soil moisture for both transpiration and GPP simulations, and the drier the soil, the larger the improvement (except the driest condition for transpiration simulation). Compared with the CLM and SSiB schemes, PHS shows comparable performance for transpiration and GPP simulations under non-limiting conditions (i.e., soil moisture > 0.06 m^3/m^3), but outperforms the other schemes as soil moisture becomes drier.

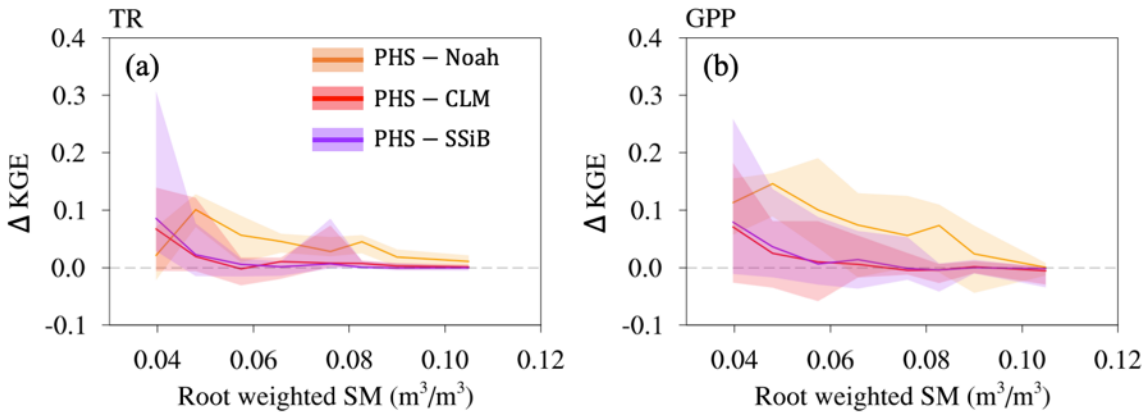

Figure 3.3: ΔKGE between PHS and SHSs for (a) transpiration (TR) and (b) GPP under different soil moisture (SM). The solid lines are the median of the ΔKGE in each SM interval, with the 25th and 75th percentiles shaded. Along the *x*-axis are eight SM observation bins. Root-weighted SM is the sum of root fraction–weighted SM at each layer, i.e., $\sum_1^4 \theta_{\mathrm{liq},i} \cdot r_i$.

3.4.1.3 Plant water stress dynamics

Figure 3.4 compares the daily averaged β between PHS and the SHSs under different soil moisture conditions. Compared with the CLM and SSiB schemes, PHS has similar β values when soil moisture is greater than 0.06 m3/m3, but larger values when the soil becomes dry. When PHS is compared with the Noah scheme, the relative difference in β becomes larger with soil dry-down. These dynamics of β under different soil moisture show similar patterns of model performance when comparing PHS with each SHS (Figure 3.3). By representing plant hydraulics in the Noah-MP model, PHS simulates larger β under dry soil conditions and hence improves model performance over the three default SHSs.

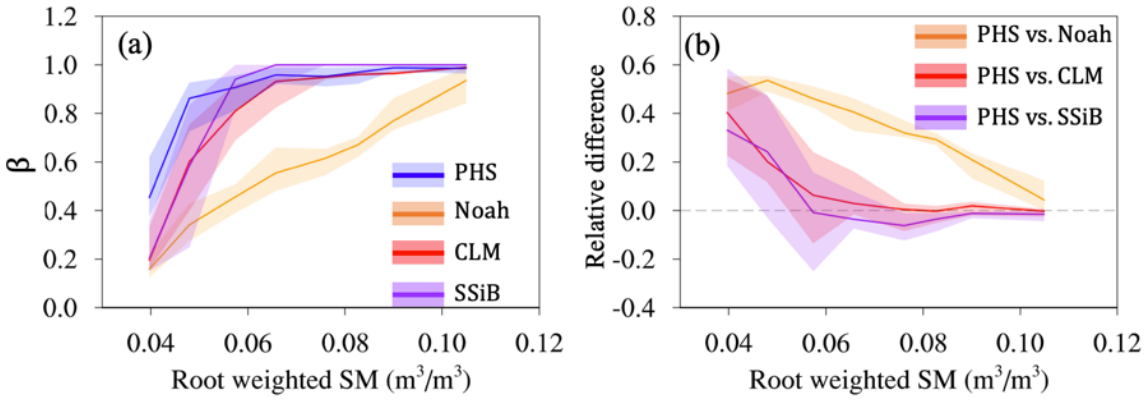

Figure 3.4: (a) β dynamics for four schemes and (b) the relative difference between PHS and three SHSs under different soil moisture (SM) conditions. Relative difference in (b) is computed as $(\beta_{\mathrm{PHS}} - \beta_{\mathrm{SHS}})/\beta_{\mathrm{PHS}}$.

3.4.1.4. Diel simulations demo under dry and wet soil moisture

We further analyzed the diel cycles of transpiration, GPP and β on a typical wet day (DOY 227 in 2013) and a dry day (DOY 235 in 2013). Compared with simulations on the wet day (Figures 3.5a and c), there are larger differences between PHS and the three SHSs for the transpiration and GPP simulations on the dry day (Figures 3.5b and d). Under the limited water condition, a small difference in β could induce a significant difference in the simulations of transpiration and GPP. In terms of β dynamics, the three SHSs show negligible diel variation (Figure 3.5e). These default schemes are based on the root zone soil moisture or soil matric potential, which varies slowly (on the order of days and weeks). On the other hand, PHS shows an apparent diel variation of β, with the maximum value at predawn and minimum value at midday (Figures 3.5e and f), following the diel cycle of LWP. Additionally, PHS captures the asymmetrical daytime fluxes of transpiration and GPP, i.e., higher fluxes in the morning than the afternoon, especially under conditions of low soil moisture content (Figures 3.5b, d and f).

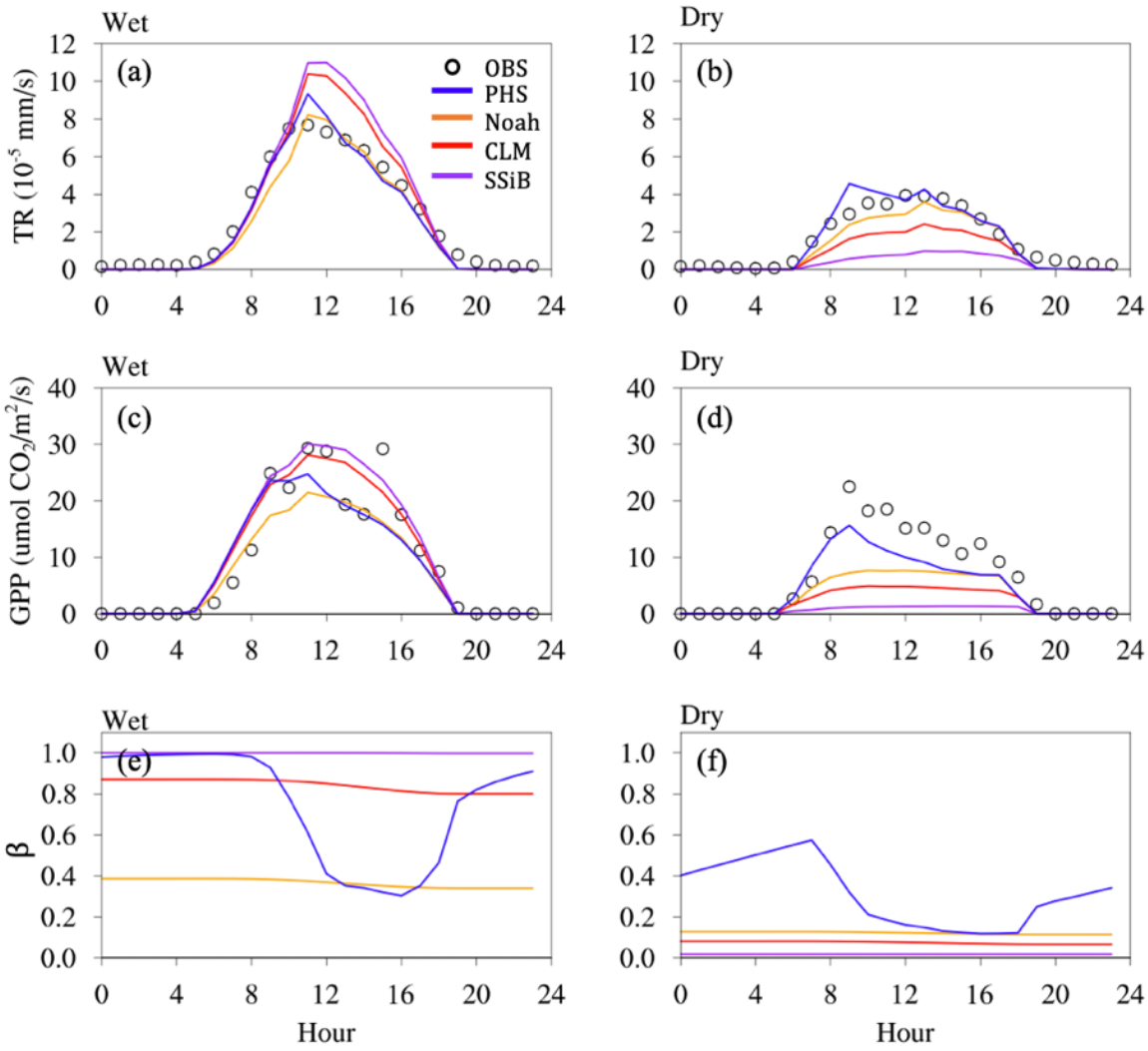

Figure 3.5: Diel cycles for (a, b) transpiration (TR), (c, d) GPP, and (e, f) β root water uptake on a typical (a, c, e) wet day (DOY 235 in 2013) and (b, d, f) sunny and dry day (DOY 227 in 2013).

3.4.2 Tree-level simulations

3.4.2.1 Overall PHS performance

We applied our PHS to simulate species with different hydraulic behaviors. The calibrated parameters for the red maple and red oak simulations are listed in Table 3.6 using observations of transpiration and stem water storage. Figure 3.6 shows their simulations at the daily time scale (DOY 195–254). It should be noted that PHS only simulates the variation of plant water storage instead of the absolute value of storage. Therefore, we adjusted the simulated stem water storage to match its average with the average of observed stem storage. During the soil moisture dry-down period (i.e., DOY 209–222; Figures S3.3 and S3.4), the red maple's transpiration and stem water storage were strongly affected by this decrease in soil water content, but this was not so for the red oak. Based on the observations, under the limited soil moisture, transpiration for the red maple gradually declined from a maximum of 0.60 g/s at DOY 2012 to 0.20 g/s at DOY 222, while oak maintained a relatively stable transpiration, with an average of around 0.33 g/s (Figure 3.6a). Concurrently, stem water storage in the red maple fell by 29% from 101.3 to 72.2 kg, but there was less of a change in stem water storage (between 107.4 and 103.1 kg) in the red oak (Figure 3.6b).

These divergent behaviors between red oak and red maple were well captured by PHS simulations, with overall high KGE and low RMSE values (Table 3.5) for both transpiration and stem water storage simulations (Figures 3.6a and b). It is important to note that our calibrated key parameters of $K_{s,\mathrm{sat}}$ and P_{50} are comparable with the *in-situ* measurements. The calibrated $K_{s,\mathrm{sat}}$ (P_{50}) is 1.00×10^{-2} mm/s and 1.50×10^{-2} mm/s (-2.00×10^{5} and -1.50×10^{5} mm) for the red maple and red oak, respectively, which are roughly consistent with the values of 0.55×10^{-2} and 1.33×10^{-2} mm/s (-1.97×10^{5} and

-1.61×10^5 mm) based on field measurements for the same species (Maherali et al., 2006). Red maple's lower $K_{s,\mathrm{sat}}$ and P_{50} than those of the red oak simulation are consistent with their different xylem architecture, i.e., diffuse-porous (red maple) and ring-porous (red oak). Oak's stem water storage simulation has a low KGE value of 0.27 over the whole period from DOY 195 to 254. However, the KGE increases to 0.77 without considering the period of DOY 195–205. This is because PHS failed to capture the increasing stem water storage in this period. Red maple's stem water storage observations show gradual recharge after a rain event at DOY 224, while the model shows immediate full recharge after soil moisture enhances. This discrepancy occurs because the model has no mechanism to reproduce the time lag associated with vessels refilling after drought.

Compared with the LWP of red oak, the red maple's LWP is more stable and less negative (Figure 3.6c), as is characteristic of its isohydric strategy. The averages of LWP measurements at noon for red maple and red oak are −0.51 and −1.3 MPa, respectively, over DOY 174–193. PHS simulated a comparable LWP of −0.74 MPa for the red maple and −2.1 MPa for the red oak. The β dynamics also show a notable difference between red maple and red oak during the dry-down period. Red oak maintains a relatively larger β, keeps stomatal openness, and supports stable transpiration. However, the red maple's β gradually declines, as the stomata closes and transpiration is reduced.

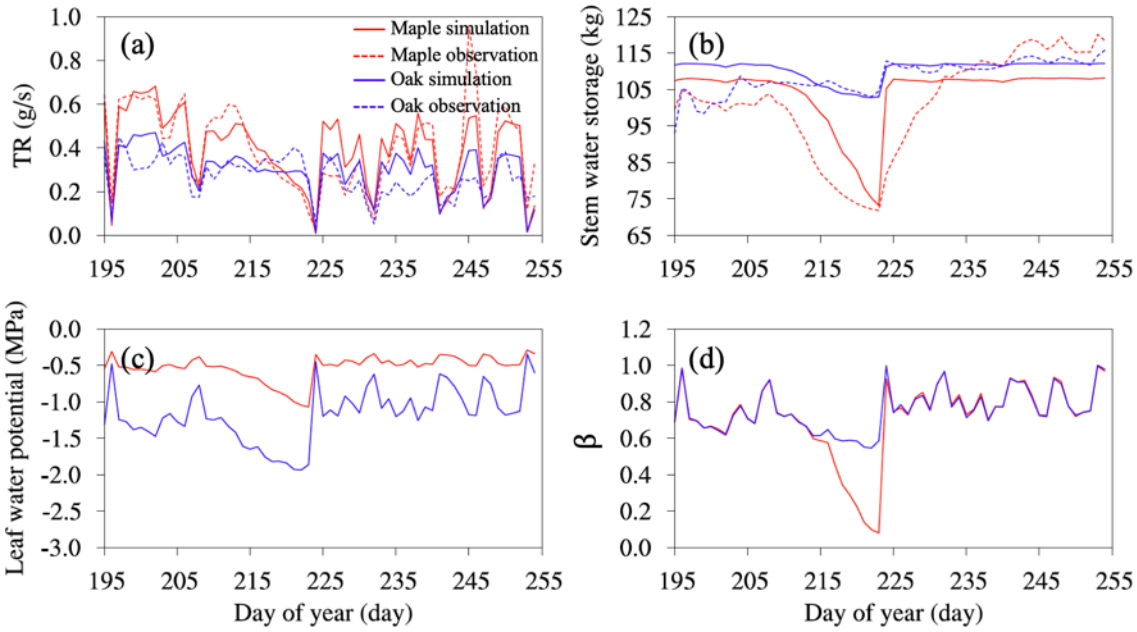

Figure 3.6: Daily simulations for red maple and red oak.

Species	TR		Stem water storage	
	RMSE	KGE	RMSE	KGE
Maple	0.10	0.82	9.76	0.54
Oak	0.08	0.70	4.96	0.27 (0.77*)

*KGE is calculated over DOY 205–254

Table 3.5: Statistics of model performance at the daily time scale over DOY 195–254.

3.4.2.2 Dynamics during the dry-down period

Figure 3.7 shows the hourly time series over the dry-down period (DOY 209–222). The diel withdrawal from stem storage of the red maple fell from 13.2 kg on DOY 209 to 0.73 kg on DOY 222, while the red oak shows opposite patterns, with storage withdrawal slightly rising from around 4.9 kg to 8.3 kg over the same period (Figure 3.7b). The stem water storage simulations capture their contrasting patterns. Simulated storage withdrawal of the red maple dropped from 15.1 kg on DOY 217 to 8.9 kg on DOY 222, and red oak's storage withdrawal slightly increased from 6.9 kg on DOY 213 to 8.1 kg on DOY 222.

For the simulation of LWP, the red maple has small diel amplitudes (around 0.5 MPa), the difference between daily maximum and minimum, and slightly dropped its daily maximum and minimum LWP over the dry-down period (Figure 3.7c). On the other hand, the LWP of the red oak has larger diel amplitudes as its anisohydric strategy allows for strongly negative daily minimum LWP. Similar patterns of stem water potential were simulated for these two trees (Figure 3.14). The water stress β, as a function of LWP, shows similar patterns for these two species. Red maple gradually decreased its daily maximum β in response to the soil drying-down period. Red oak, which uses steadier and deeper water sources, shows few changes in β dynamics. These behaviors are consistent with their different hydraulic strategies. Red maple is more isohydric, and it uses tight stomata regulations, maintaining a relatively stable and high LWP. Red oak is more anisohydric, and regularly tolerates highly negative LWP.

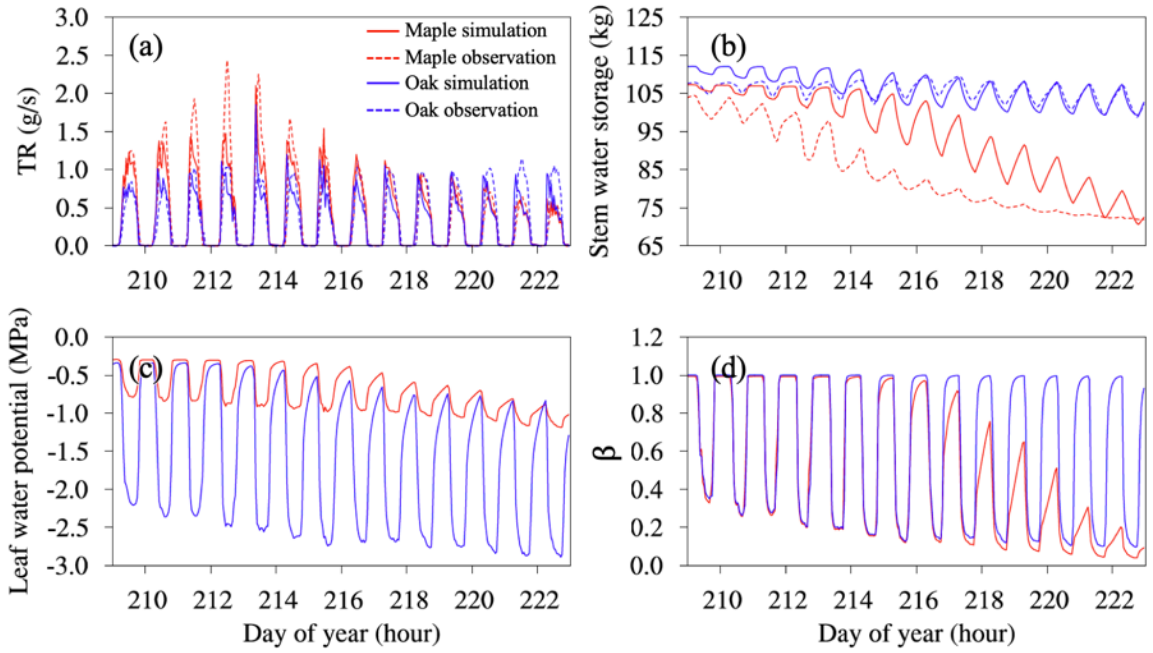

Figure 3.7: Hourly simulations for the red oak and red maple during the dry-down period. Panels (a) and (b) show comparisons between model output (solid lines) and observations (dotted lines). Observations were not available for LWP or β and are therefore omitted from panels (c) and (d).

3.4.2.3 Root water uptake

Figure 3.8 shows the root water uptake (Q) of the red oak and red maple during the dry-down period (DOY 209–222). With limited water in the top 2 m of soil, the red maple significantly reduced its Q from 0.45 g/s on DOY 209 to 0.17 g/s on DOY 222 (decrease of 62%). Concurrently, the red oak reduced its Q from 0.32 g/s to 0.25 g/s (reduction of 22%). Red maple obtained most of its water from the second soil layer, accounting for 95% of the total Q on DOY 209 and 81% on DOY 222 (Figures 8a and S6), because about half (47%) of maple's fine roots live in this layer. For the red oak, during non-water-limited conditions, most water also came from the second soil layer, accounting for 82% on DOY 209. As the upper three soil layers dried, the red oak started using more water from the wet

fourth layer, increasing from only 1% on DOY 209 to 91% on DOY 222 (Figures 3.8a and S6).

Additionally, under the relatively wet soil conditions, the red maple and red oak absorbed the most water during the daytime (i.e., 06:00–18:00; Figures 3.8b and c), which accounts for 92% and 86% of the daily total *Q* on DOY 209 for the red maple and red oak, respectively. As the soil dried, these two species started taking up more water during the nighttime (i.e., 00:00–05:00 and 19:00–23:00), which accounts for 48% and 43% of the daily total *Q* on DOY 222 for the red maple and red oak, respectively.

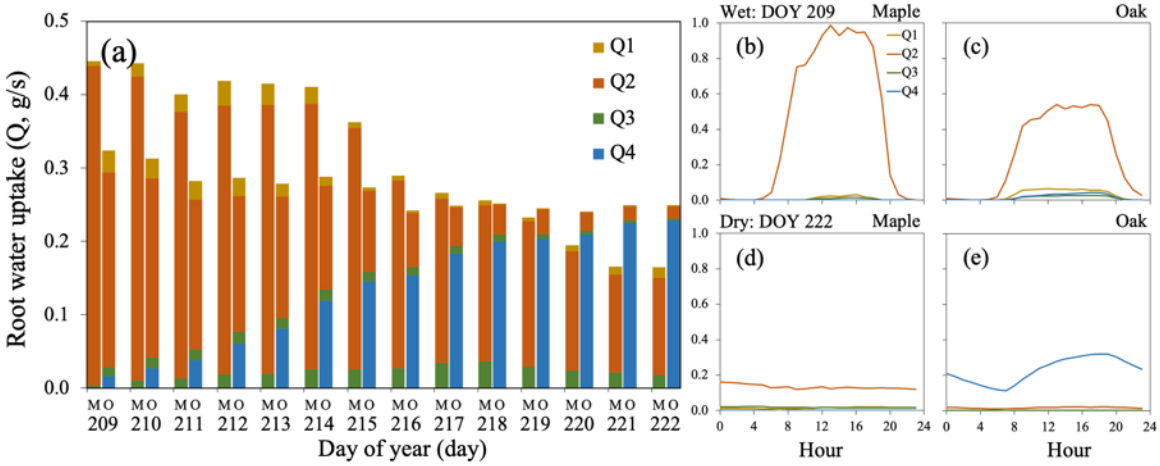

Figure 3.8: Root water uptake (*Q*) for red maple (M, left bars) and red oak (O, right bars) during dry-down period: (a) daily *Q* from the 1st to 4th soil layer (i.e., Q1 to Q4); (b–e) diel variation of *Q* under wet and dry conditions for these two trees.

3.4.3 Sensitivity simulations with different plant capacitance

Figure 3.9 shows the tree-level simulations of a series of sensitivity experiments with different stem hydraulic capacitance during the dry-down period (DOY 209–222). Overall, different hydraulic capacitance induced noticeable differences in simulations of water and carbon variables, and their difference become larger as the soil dried. Specifically, larger hydraulic capacitance has more readily available water in the stem and closer to the site of transpiration (Figure 3.9a), which enables larger stomatal openness (daytime β in Figure 3.9c) and hence can supply more transpiration (Figure 3.9d) and promote increased carbon gain (Figure 3.9f). Larger hydraulic capacitance also supports less-negative daily minimum stem water potential, which plays a vital role in relieving xylem hydraulic stress and reducing xylem vulnerability to cavitation (Figure 3.9b). For Q (Figure 3.9e), the overall larger hydraulic capacitance has a larger water reservoir to supply transpiration and hence requires less daily root water absorption. It should be noted that when hydraulic capacitance is less than 3.0E-4 m−1 (inset panel in Figure 3.9e), the plant absorbs slightly more water from soil with larger hydraulic capacitance on DOY 222. Although a larger hydraulic capacitance can supply more water, this increased water is smaller than the increased transpiration, and therefore more Q is needed.

Figure 3.16 shows the hourly simulations of these sensitivity experiments. Larger hydraulic capacitance shows a smaller daily fluctuation of stem water potential (Figure 3.16b), which can help relieve xylem hydraulic stress from frequent water potential variation. Stem capacitance also affects the timing of Q. Larger hydraulic capacitance promotes a longer period for Q during the night.

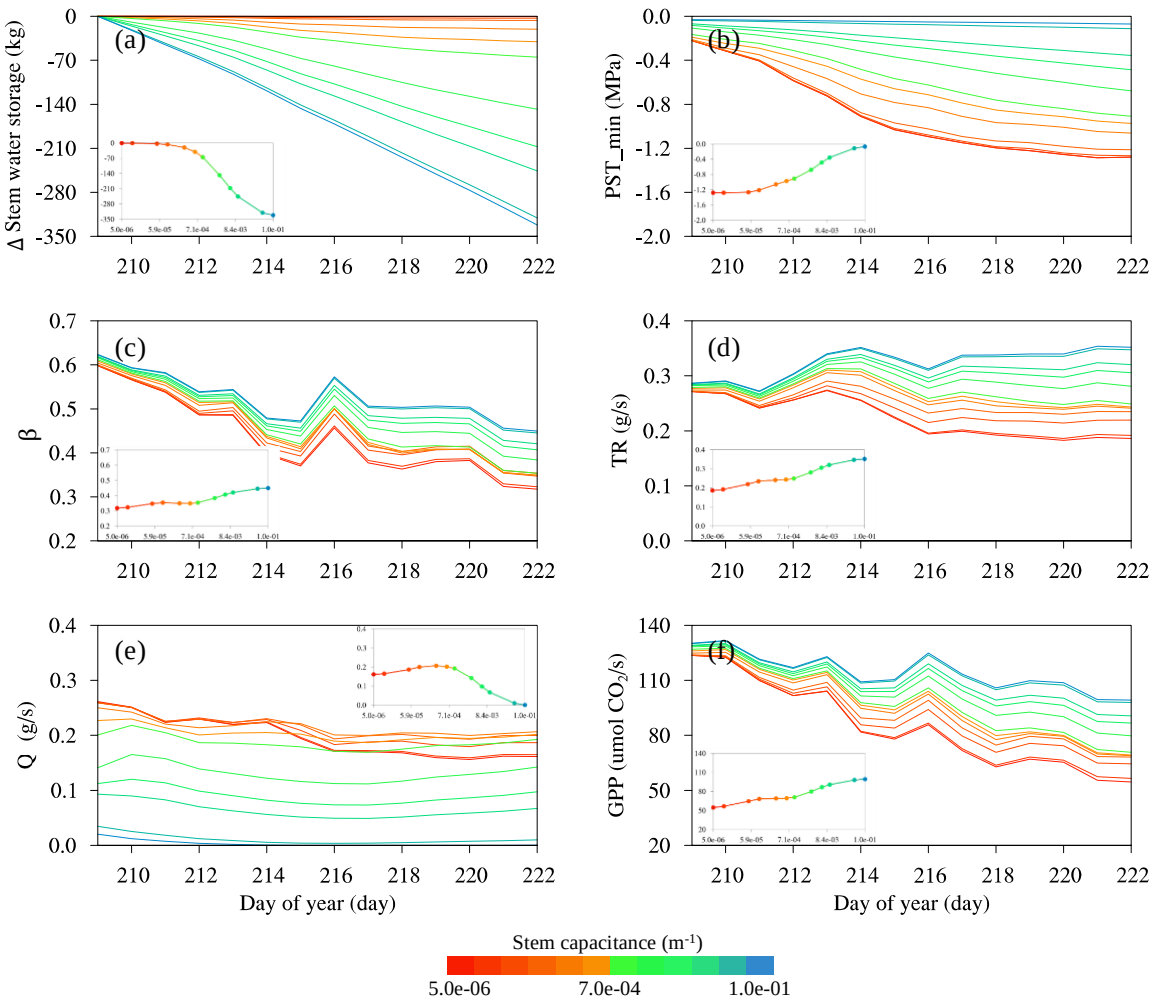

Figure 3.9: Daily simulations with different stem hydraulic capacitance: (a) stem water storage (values relative to storage on DOY 209); (b) minimum stem water potential (PST_min); (c) daytime plant water stress β; (d) transpiration; (e) daily total Q, and (f) GPP. The inset figures show the relationship between hydraulic capacitance and the corresponding *y*-axis value on DOY 222.

3.5 DISCUSSION AND CONCLUSIONS

In this paper, we present a PHS for use in Noah-MP. The PHS uses Darcy's law to describe the physical process of water movement from soil to root, from root to stem, and from stem to leaf, while explicitly representing water storage in the stem and canopy. The stem represents both the trunk and the branches. LWP is utilized to formulate the β and hence to regulate the stomatal openness more physically, instead of the commonly used SHS approach, which employs soil moisture or soil water potential, as is the case in the majority of LSMs, including Noah-MP. Additional physical and measurable state variables (i.e., leaf/stem water potential and the variations of stem/canopy water storage) and flux variables (i.e., water fluxes from soil to root/stem and from stem to leaf) are represented in PHS. As such, observational constraints can be more easily incorporated in PHS than in SHSs. Most of the introduced parameters in PHS are physically measurable (e.g., $K_{s,\mathrm{sat}}$) or can be derived from *in-situ* or remote-sensing measurements. The newly developed Noah-MP-PHS considers whole-plant hydraulic strategies, including hydraulic traits at leaf, stem, and root levels. Therefore, in terms of water transport and regulation, Noah-MP-PHS facilitates the transition of the soil–plant–atmosphere–continuum model from the traditional "big leaf" concept into a "big tree" concept.

Noah-MP-PHS was found to improve the simulation of water and carbon in plot-level experiments, especially under dry soil conditions. The inclusion of plant hydraulics in the Noah-MP model generates a larger β (i.e., less water stress) under dry soil conditions than in three conventional SHSs, thereby enabling more realistic simulations of transpiration and GPP that closely replicate observations (Figures 3.2–3.4). Compared with the negligible diel variation of β from the default SHSs, PHS' β shows an apparent diel cycle with a maximum value at predawn and a minimum value around midday (Figure 3.5). Plant water stress in the default SHSs is based on soil moisture or soil water potential,

which only represents the control of water supply from soil and varies slowly (on the order of days and weeks). Instead, PHS utilizes LWP for plant water stress calculations, which has been shown to be a more mechanistic indicator for stomatal regulation (Manzoni, 2014; Novick et al., 2016; Sperry et al., 2017). Therefore, PHS' β responds to not only the water supply from the stem (and ultimately from soil) but also the atmospheric demand, and hence enables more realistic dynamics of water and carbon fluxes at diurnal and potentially longer timescales (Denmead & Shaw 1962; Fisher et al., 2006; Xu et al. 2016; Kennedy et al., 2019). It should be noted that the function of hydraulic redistribution (HR) was disabled in our simulations because no evidence of this phenomenon has ever been observed at UMBS (He et al., 2003). However, Noah-MP-PHS does have the ability to simulate the HR process, which plays a vital role in terrestrial water and energy cycles for arid and semiarid regions (Ryel et al., 2002; Luo et al., 2016).

Noah-MP-PHS was found to successfully capture the different plant hydraulic behaviors between red maple and red oak. Overall, simulated transpiration and stem water storage were consistent with *in-situ* observations for these two species (Figure 3.6). During the dry-down period (DOY 209–222, 2014), Noah-MP-PHS successfully captured the obvious patterns of decreasing transpiration and stem water storage in red maple, and the stable transpiration and slightly reduced stem water storage in red oak (Figure 3.7). Additionally, the model also showed an ability to simulate the difference in Q between these two species. The red maple obtained most of its water from the second soil layer (30–60 cm), where about half of its roots exist (Figure 3.8). For the red oak, the majority of root–water uptake came from the second soil (30–60 cm) layer during non-water-limited conditions, transitioning to absorbing most of the water from the wetter fourth soil layer (1–10 m) as the upper three soil layers dried. These model-simulated dynamics agree well with field isotopic measurements of tree-water uptake (Matheny et al. 2016). Noah-MP-

PHS tree-level simulations also show the different timing of *Q* for these two species. Under relatively wet soil conditions, these two species absorb most of their water during the daytime (Figure 3.8). As the soil dries, they start taking up more water at nighttime, which accounts for up to 50% of the total daily water uptake.

The divergent hydraulic strategies of these two species are well characterized by the trait-based parameters in PHS at the leaf (e.g., TLP), stem (e.g., saturated hydraulic conductivity), and root (e.g., RAI and rooting depth) levels. For example, the calibrated parameters of $K_{s,\mathrm{sat}}$ and P_{50} for the red maple and red oak, are comparable to the observational results of Maherali et al. (2006), reflecting their different xylem architecture. Red maple has shallow roots and our study site's well drained soil regularly limits surface soil water resources, causing it to readily experience water stress. However, red maple is strongly isohydric, with tight stomatal regulation, and maintains a relatively stable and high LWP and, hence, conservatively controls transpiration (Figure 3.7). Red oak is more anisohydric, characterized by its lax stomatal regulation, and regularly tolerates strongly negative LWP, which allows restively liberal transpiration. This behavior of red oak is buffered by both its deep rooting depth and highly conductive xylem architecture (Matheny et al. 2017). PHS is unable to capture well the gradual recharge of stem water during the rewetting period (Figure 3.6). The hysteresis phenomenon occurs in the relationships between xylem water potential and conductivity during the refilling process if refilling does not, or is slow to, occur (Sperry et al., 2003; Hacke et al., 2003). Advancement of the PHS framework should further include the mechanism to reproduce the time lag associated with vessel refilling after drought (Mrad et al., 2018). It should be noted that the hormone abscisic acid (ABA) also contributes to regulating the stomatal aperture (Tuzet et al., 2003; Fatichi et al., 2016). Even though our PHS is capable of simulating the opposing hydraulic strategies without explicitly invoking ABA, this hormonal control could be crucial for

some species and is another direction for further PHS model development (Goldstein et al., 2002; Deans et al., 2017).

Our results demonstrate that it is essential to represent plant storage, or hydraulic capacitance, in plant hydraulics models. Sensitivity experiments with plant hydraulic capacitance show that a larger stem hydraulic capacitance with more available water in the stem enables larger stomatal openness, can supply more transpiration, and promote increased carbon gain (Figure 3.9). Stem capacitance also buffers against xylem hydraulic stress. A larger hydraulic capacitance supports a smaller daily fluctuation of stem water potential and has less-negative daily minimum stem water potential, which therefore helps relieve xylem hydraulic stress and reduce xylem vulnerability to cavitation during dry soil conditions (Tyree et al., 1989; Meinzer, 2003; Maherali et al., 2004 & 2006).

Additionally, plant water storage enables the simulation of nocturnal plant water recharge. Nocturnal water recharge has ecophysiological significance to plants, including refilling plant water storage, relieving xylem hydraulic stress, delivering nutrients, and so on (Scholz et al., 2007; McDonald et al. 2002; Snyder et al. 2003; Daley & Phillips 2006; Fang et al., 2016). Our tree-level simulations show that the nighttime recharge of red maple and red oak accounts for nearly 50% of the daily total soil to root water flux (Figure 3.8). This ratio is consistent with previous studies in which nighttime water recharge accounts for approximatly10%–50% of the total daily transpiration (Scholz et al., 2008; Wang et al., 2012; Carrasco et al., 2014; Zhao et al., 2017). The sensitivity experiments also showed that a larger stem hydraulic capacitance demands a longer period for Q during the night to supply transpiration in the following daytime (Figure 3.16).

With the implemented plant hydraulics model in LSMs, the ultimate goal is for use within ESMs or numerical weather prediction (NWP) models on large spatial scale simulations. One of the central challenges is how to properly represent the diversity of

plant hydraulic strategies on large spatial scales. LSMs commonly group plant species into broad categories, i.e., plant functional types (PFTs), by the phenological, environmental, leaf morphological traits, etc. (Running et al., 1994; Bonan et al., 2002). The PFT framework has offered a simple way to deal with plant diversity (albeit with limited plant traits considered) and allowed ESMs and NWP models to efficiently simulate vegetation–climate and –weather interactions on large spatial scales (Scheiter et al., 2013; Pappas et al., 2016). However, the current PFT framework does not explicitly incorporate the whole-plant hydraulic strategy nor does it consider plant hydraulic traits at the root-, stem- and leaf-levels (Matheny et al., 2017). There are commonly three approaches to facilitate the incorporation of plant hydraulics into large-scale models. The first approach is to represent plant hydraulic strategies under the existing PFTs. For example, Kennedy (2020) presented a set of plant hydraulic parameters for each PFT in CLM5 to conduct the global simulations. However, studies have shown that there is large divergence of plant traits within a given PFT (Konings et al., 2017; Wright et al., 2015). Alternatively, the second approach is to define new categories with similar plant hydraulic strategies either alongside or within the current PFTs. Xu et al. (2016) defined four new PFTs with discrete hydraulic traits to better reproduce vegetation dynamics in seasonally dry tropical forests. Mitchell et al. (2008) defined the "hydraulic functional types" (HFTs) to group species with different water use strategies using multiple-trait associations between sixteen traits relating to water transport, water use efficiency and response to water deficit. The first and second approach remain within or are an expansion to current PFT framework, and inevitably suffer similar underlying problems, including finite categories, coarse resolution, over-aggregation and fixed plant attributes (Matheny et al., 2017; Van Bodegom et al., 2012; Pappas et al., 2016). Such disadvantages have been shown to lead to errors in water and carbon simulations and do not flexibly consider vegetation adaptation

to the environment (Matthes et al., 2016; Scheiter et al., 2013; Poulter et al., 2011). Moving beyond the PFT paradigm, the third promising solution is a fully trait-based approach. Instead of classifying plants into limited categories, the calculations (e.g., water and carbon fluxes) in trait-based models are directly based on functional traits grounded by observable plant traits (Van Bodegom et al., 2014; Yang et al., 2015; Laughlin and Laughlin, 2013). These functional traits are allowed to vary in response to environmental drivers (e.g., water availability and nutrient availability) and habitat filtering/adaptation processes through the incorporation of mechanistic plant functional sub-models (Verheijen et al., 2013; Van Bodegom et al., 2014). The trait-based approach is becoming a necessity for constructing the next generation dynamic global vegetation models and has shown promising improvements in model simulations (Verheijen et al., 2013; Scheiter et al. 2013; Van Bodegom et al., 2014). Together with the emerging multi-source observations, including *in-situ* (e.g., the TRY database, Kattge et al., 2011) and remote sensing (e.g., vegetation optical depth, Konings et al., 2019), and new technologies like machine learning (e.g., Verrelst et al., 2012; Moreno-Martínez et al., 2018), the trait-based approach provides a promising future for the representation plant hydraulic and other functional traits in large spatial scale models. In our tree-level experiments, we calibrated two sets of PHS related parameters and hence defined two types of HFT for red maple and red oak, following the second approach outlined above. This strategy allowed us to represent the distinct plant hydraulic strategies within the existing model framework.

Overall, compared to the default Noah-MP, simulations using the newly developed Noah-MP-PHS show better agreement with observations at both the plot and tree level. Through this new representation of plant hydraulic strategies, Noah-MP-PHS provides the capability to better understand the role of vegetation in the water and carbon cycles, energy

budgets, land–atmosphere interaction, and climate feedbacks, especially under climate change conditions characterized by increased drought frequency.

3.6 SUPPLEMENTARY

Parameter	Source	Unit	Plot-level	Maple	Oak
TLP	Calibration	mm	-1.5E+5	-0.7E+5	-2.0E+5
C_{leaf}	Empirical determined	1	1.0E-7	1.0E-7	1.0E-7
$K_{s,sat}$	Calibration	$mm \cdot s^{-1}$	2.0E-2	1.0E-2	1.5E-2
P_{50}	Calibration	mm	-2.0E+5	-2.0E+5	1.5E+5
C_{stem}	Calibration	m^{-1}	4.0E-4	7.0E-4	1.0E-4
S_{sap}	Field data	$m^2 \cdot m^{-2}$	1.5E-3	6.3E-4	6.8E-4
V_{sap}	Empirical calculated ($S_{sap} \times h_c$)	$m^3 \cdot m^{-2}$	4.4E-2	1.7E-2	2.1E-2
h_c	Field data	mm	29.0E+03	27.4E+03	31.3E+03
a_1	Calibration	unitless	1.0E+0	4.0E-1	4.0E+0
a_2	Xu et al. (2016)	unitless	4.0E+0	4.0E+0	4.0E+0
a_3		unitless	6.0E+0	6.0E+0	6.0E+0
$f_{root-shoot}$	Field data	$m^2 \cdot m^{-2}$	1.0E+0	9.0E+0	1.0E-1
Rooting depth	Empirical determined	m	2.0E+0	2.0E+0	1.0E+1

Table 3.6: PHS parameter values for different simulations.

Variable	Scheme	Daily					Hourly				
		RMSE	KGE	CC	BR	VR	RMSE	KGE	CC	BR	VR
TR	Noah	0.60	0.62	0.86	0.82	1.30	1.06	0.66	0.93	0.82	1.28
	CLM	0.57	0.54	0.86	0.93	1.43	1.22	0.67	0.92	0.93	1.31
	SSiB	0.61	0.48	0.86	**0.94**	1.49	1.31	0.66	0.92	**0.94**	1.33
	PHS	**0.48**	**0.72**	**0.87**	0.91	**1.23**	**1.03**	**0.72**	**0.94**	0.90	**1.25**
GPP	Noah	2.96	0.49	0.55	0.79	1.11	5.02	0.77	0.92	0.79	0.99
	CLM	2.44	0.54	0.59	0.93	1.21	4.36	0.89	0.92	0.93	0.99
	SSiB	2.59	0.48	0.57	**0.95**	1.27	4.56	0.89	0.91	**0.95**	**1.01**
	PHS	**2.10**	**0.62**	**0.63**	0.93	**0.97**	**4.19**	**0.89**	**0.92**	0.93	0.96
SM1	Noah	0.014	0.80	0.85	1.12	0.93					
	CLM	0.016	0.51	0.84	0.90	1.46					
	SSiB	0.017	0.46	0.83	0.89	1.50					
	PHS	**0.012**	**0.81**	**0.85**	**1.07**	0.91					
SM2	Noah	0.013	**0.84**	0.91	0.89	**0.93**					
	CLM	0.030	0.26	0.87	0.65	1.64					
	SSiB	0.032	0.20	0.86	0.63	1.70					
	PHS	**0.013**	0.74	**0.91**	**0.92**	0.77					
SM3	Noah	0.014	**0.62**	0.73	1.11	0.75					
	CLM	0.024	0.11	0.51	0.81	1.72					
	SSiB	0.026	0.00	0.49	0.79	1.83					
	PHS	**0.013**	0.59	**0.76**	**1.11**	0.69					
SM4	Noah	0.044	-0.18	0.86	2.02	0.43					
	CLM	0.043	-0.17	0.80	2.01	0.44					
	SSiB	0.043	-0.17	0.80	2.01	0.44					
	PHS	**0.036**	**0.07**	**0.89**	**1.84**	**0.62**					

Table 3.7: Statistics of model performance at the daily and hourly time scales (best values are written in bold type).

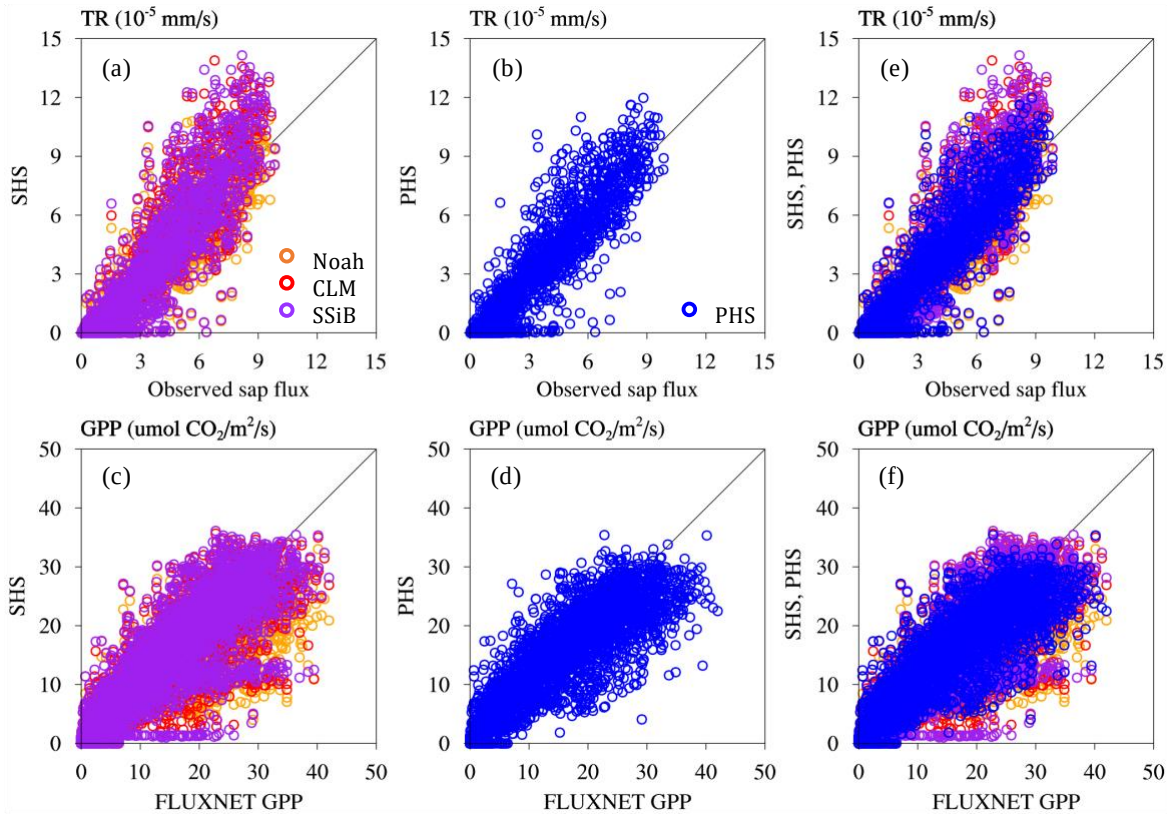

Figure 3.10: Comparison of transpiration (TR) and GPP at the hourly time scale.

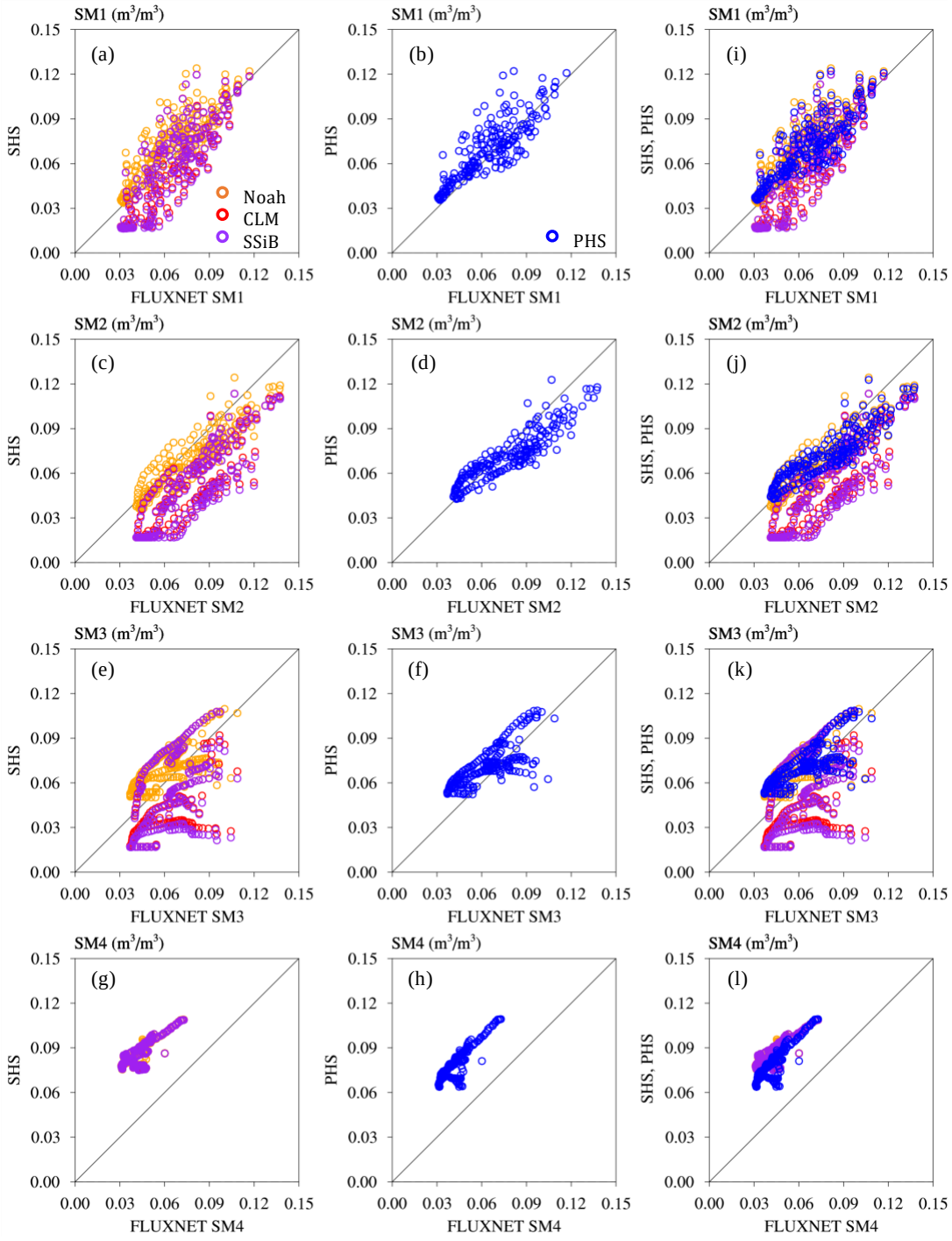

Figure 3.11: Comparison of soil moisture from 1st–4th layer (SM1–SM4) at the daily time scale.

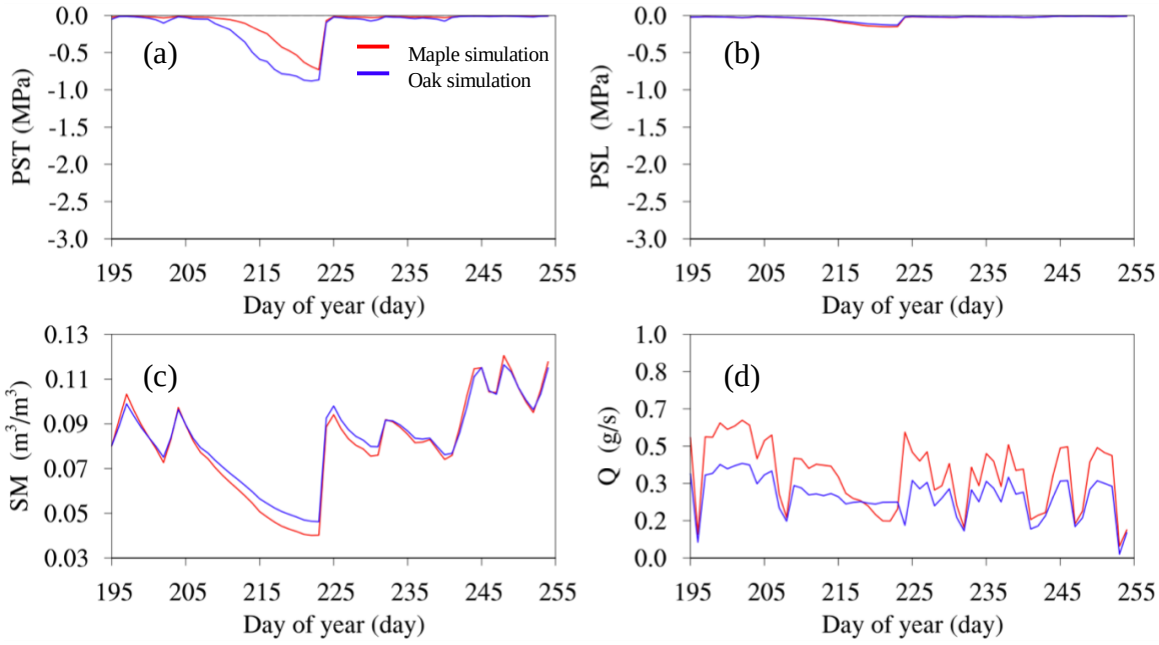

Figure 3.12: Daily simulations of stem water potential (PST), root-weighted soil water potential (PSL) and root-weighted SM, and total root water uptake (Q).

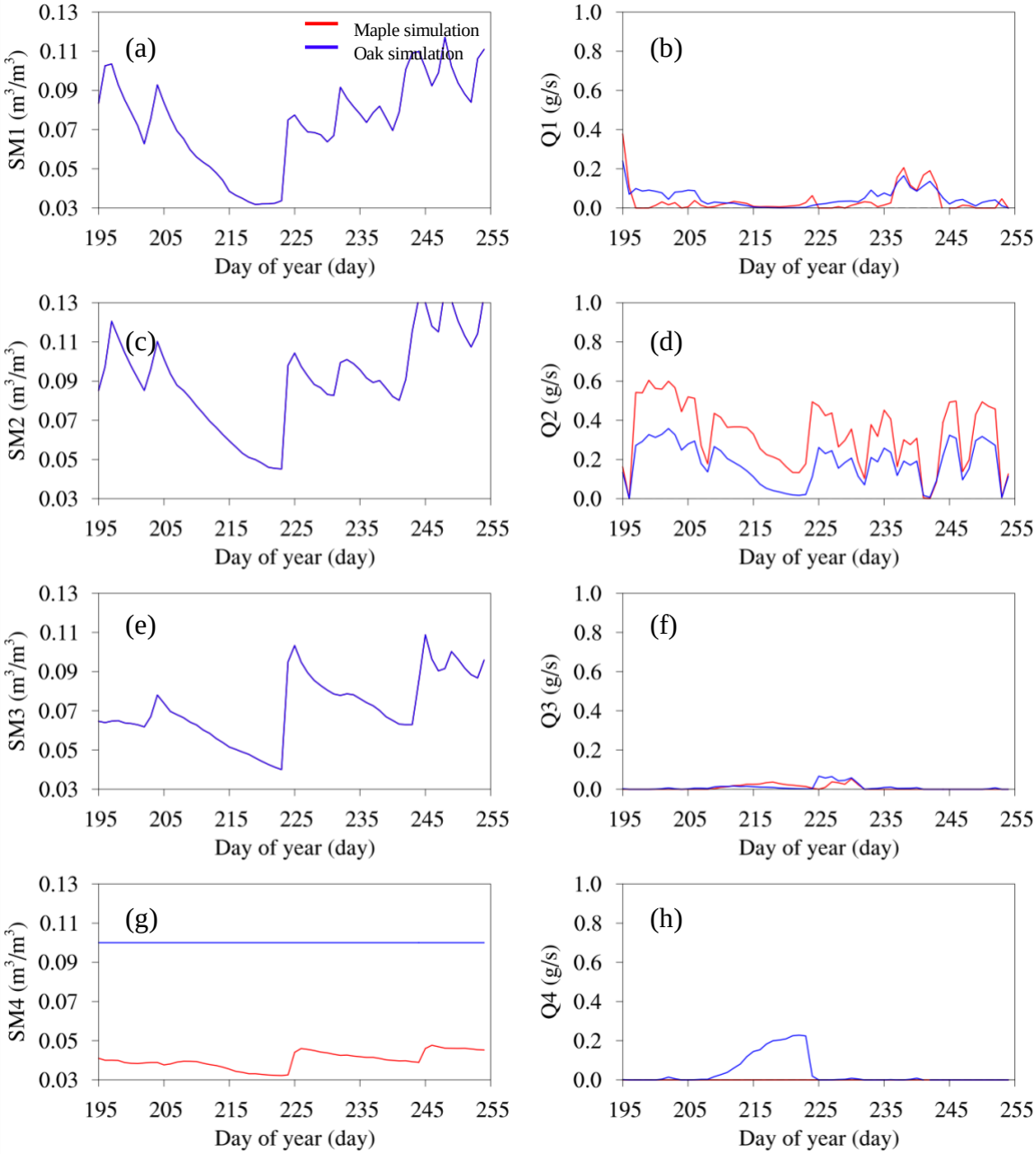

Figure 3.13: Daily SM from 1st–4th layer (SM1~SM4) and Q from 1st–4th layer (Q1~Q4).

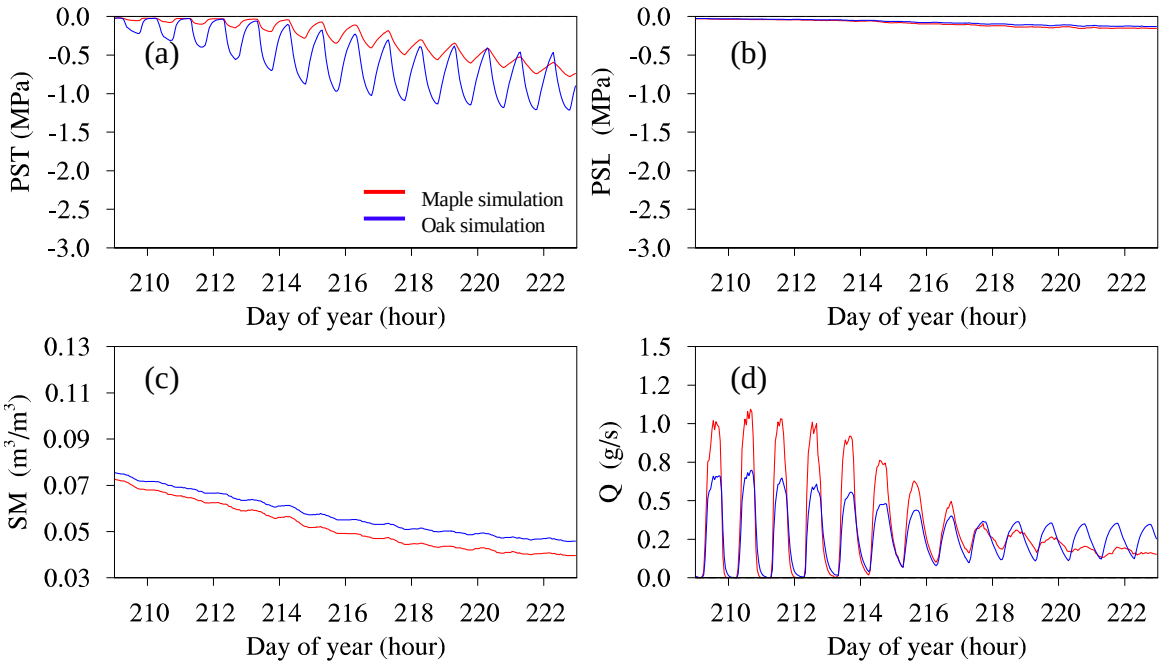

Figure 3.14: Hourly simulations of PST, root-weighted PSL and root-weighted SM, and total Q.

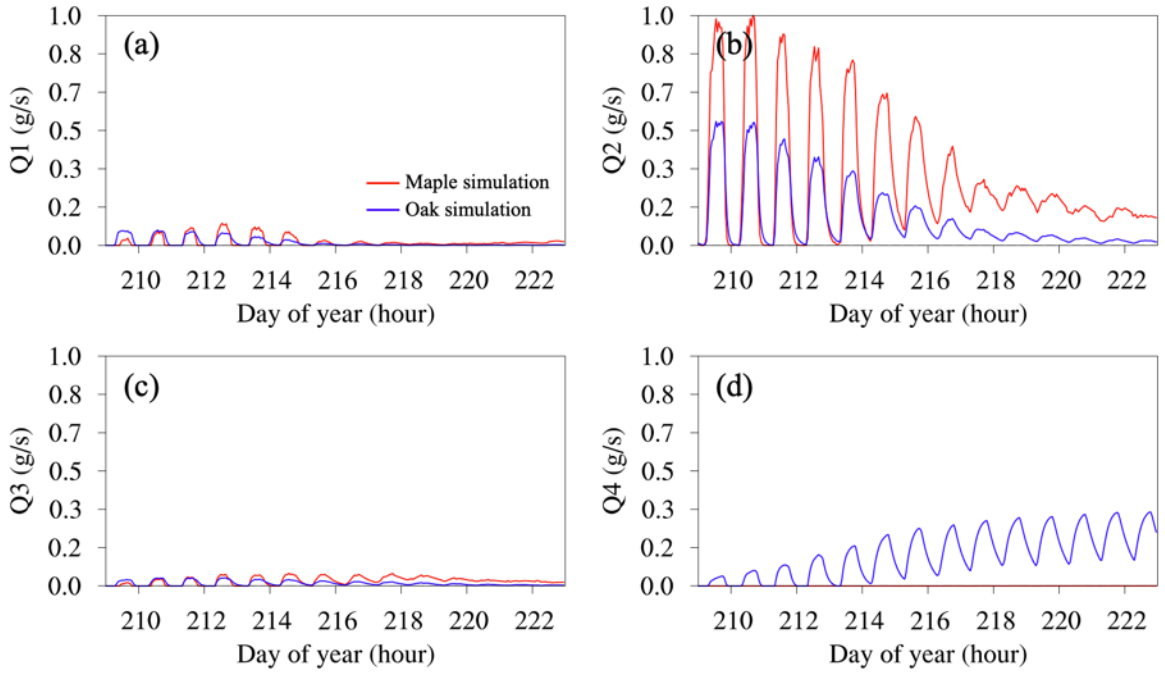

Figure 3.15: Hourly Q simulations from 1st–4th layer (Q1–Q4).

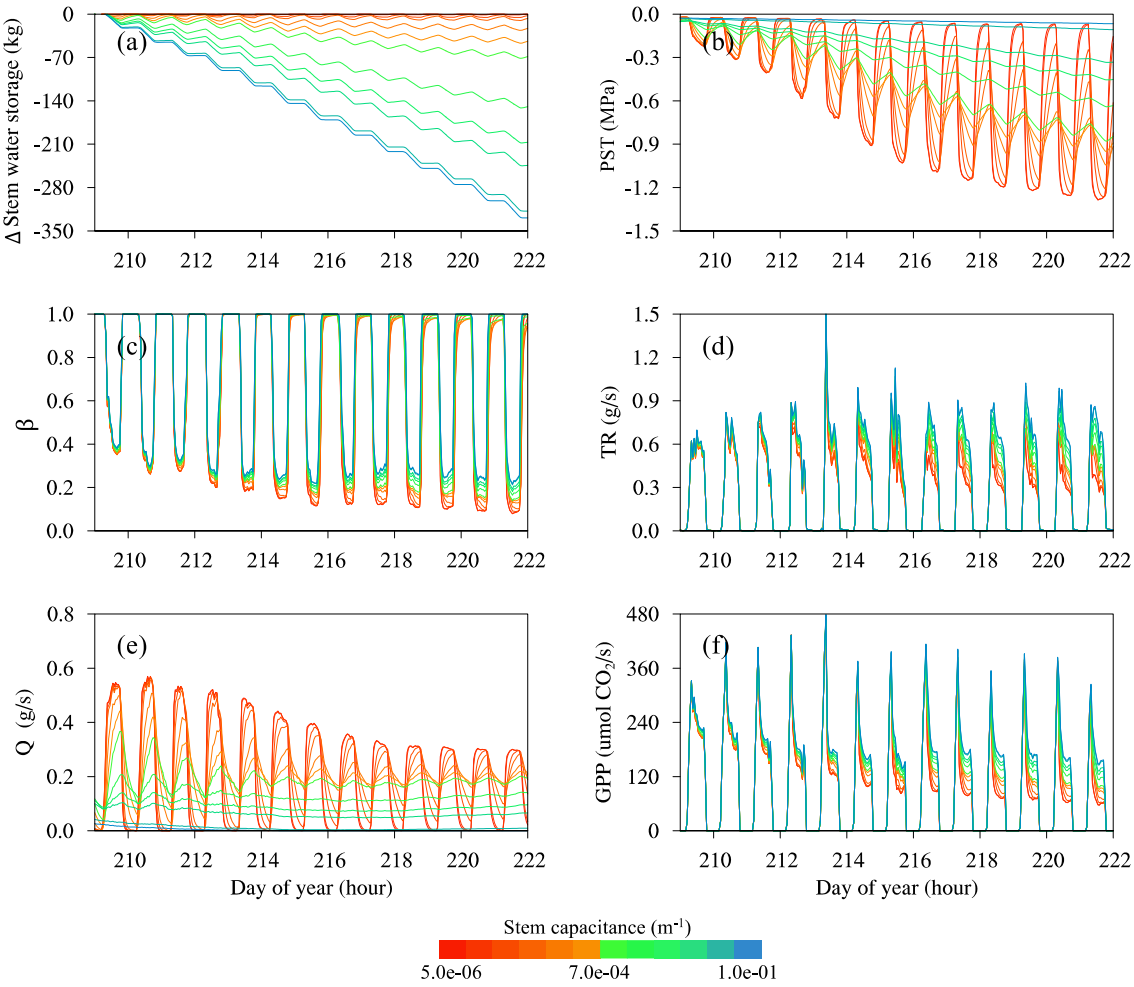

Figure 3.16: Hourly simulations with different stem capacitance. (a) stem water storage (values relative to the storage in DOY 209), (b) PST, (c) daytime plant water stress β, (d) transpiration, (e) total Q, and (f) gross primary production (GPP).

Chapter 4: Impacts of Plant Hydraulics on Transpiration Partitioning and Terrestrial Total Water Storage over CONUS

ABSTRACT

Plant hydraulics describes the mechanism of plant water uptake, transport, and use. Plant hydraulics scheme (PHS) can improve water and carbon simulations compared with the empirical soil hydraulics schemes (SHSs) that are widely used in land surface models. In this study, we extended the plot-level and tree-level PHS experiments to forest regions in the contiguous United States (CONUS). In addition to the default three SHS experiments, we designed three PHS experiments, including PHS_plot, PHS risk-averse, and risk-prone experiments based on the calibrated PHS parameters from UMBS plot-level, maple tree-level and oak tree-level simulations, respectively. For PHS simulations, we calculated the spatial sapwood area and volume indexes over CONUS forest regions innovatively using the datasets of forest canopy height and tree density based on species-specific allometric equations. We focus primarily on the ratio of transpiration to evapotranspiration (TR/ET) and the total water storage anomaly (TWSA). Results show roughly similar TR/ET patterns in both PHS and SHS experiments. Plant hydraulic traits affect the TR/ET of PHS experiments. Forests with larger tree density and canopy height, and hence larger sapwood area and volume indexes, tend to have larger TR/ET. This indicates that PHS, with more realistic representations of plant traits and hydraulic strategies, could improve the TR/ET simulation (e.g., improve the TR/ET underestimation over the deciduous broadleaf forest). Both PHS and SHS experiments show similar spatial patterns of TWSA amplitude over the CONUS. PHS with different hydraulic strategies have a large difference in the simulated TWSA amplitude, accounting for an overall average of 37.57% of GRACE TWS amplitude over the CONUS. From 2003 through 2016, TWSA of PHS experiments is slightly more consistent with GRACE TWSA than that of

SHS experiments average in terms of the difference in amplitude and timing of soil moisture anomaly. As for the 2011 Texas drought, PHS experiments, especially the risk-prone experiment, better capture the GRACE TWSA than the default SHS experiments. Our study highlights that plant hydraulics, which is generally excluded in Earth system models, could provide a vital link for reconciling observations and models of terrestrial water cycles.

4.1 INTRODUCTION

Terrestrial ecosystems play a crucial role in global water and carbon cycles. Plants are expected to suffer more hydroclimatic stresses with declining soil moisture and rising vapor pressure deficit (VPD) under climate change (Novick et al., 2016; Grossiord et al., 2020). Therefore, understanding and modeling climate change impacts on ecosystems are crucial for predicting future biosphere-atmosphere interactions (Anderegg and Venturas, 2020; Eller et al., 2020). As a critical component of Earth system models (ESMs), land surface models (LSMs) simulate water, carbon and energy fluxes, and are used for drought/flood prediction, weather forecasts, and climate prediction (Yang et al., 2011; Bonan and Doney 2018). However, most current LSMs use simplistic representations of the effects of soil water stress on vegetation employing empirical soil hydraulic schemes (SHSs), which are based on either soil water content or soil water potential (Li et al., 2020; Anderegg and Martin, 2020; Christoffersen et al., 2016; Sitch et al., 2015). SHSs cannot accurately capture the ecosystems' response to water stress conditions and contribute significant uncertainties in water and carbon simulations (Matheny et al., 2014a; Powell et al., 2013; Trugman et al., 2018).

Plant hydraulics describes the mechanism of plant water uptake from the soil, water transport to leaves, and water loss through stomata (Anderegg and Martin, 2020; McDowell et al., 2019; Mencuccini et al., 2019). Such plant water regulation is determined by the whole-plant hydraulic strategy with hydraulic functional traits at the leaf (e.g., isohydric vs. anisohydric behaviors), stem (e.g., ring-porous vs. diffuse-porous), and root (shallow vs. deep roots) levels (Matheny et al., 2017; McCulloh et al., 2019). For example, the “cavitation risk-averse” red maple (Acer rubrum) is more isohydric behavior with shallow roots and diffuse-porous xylem architecture. In contrast, the “cavitation risk-prone” red oak (Quercus rubra) is more anisohydric behavior with deep roots and ring-

porous xylem architecture (Li et al., 2020; Matheny et al., 2016). Emerging studies have implemented plant hydraulics scheme (PHS) to replace the traditional SHSs, and applied for experiments at different scales, including tree scale, flux tower scale and even regional/global scales (Li et al., 2020; Eller et al., 2020; Sabot et al. 2020; Liu et al., 2020; Kennedy 2020; Kennedy et al., 2019; Anderegg et al., 2017). These studies show that the plant hydraulics scheme (PHS) can improve water and carbon fluxes simulations, especially under dry soil moisture and/or high VPD conditions.

Li et al. (2020) implemented a novel PHS in the Noah-MP land surface model (hereafter Noah-MP-PHS). It employs a big-tree rather than a big-leaf concept, wherein the whole-plant hydraulic strategy is considered including root-level soil water acquisition, stem-level hydraulic conductance and capacitance, and leaf-level isohydricity and hydraulic capacitance. Noah-MP-PHS was evaluated using plot-level observations from the University of Michigan Biological Station. Compared with default SHSs, PHS improved both water and carbon simulations, especially during periods of dry soil conditions (Li et al., 2020). Noah-MP-PHS was also applied for tree-level simulations, and well captured the different plant hydraulic behaviors between the “cavitation risk-averse” red maple and the “cavitation risk-prone” red oak. These experiments provide three plant hydraulics scenarios, i.e., a comprehensive strategy with different species from the plot-level experiments, an isohydric ‘risk adverse’ hydraulic strategy from the red maple experiment, and an anisohydric ‘risk prone’ strategy from the red oak experiment. Therefore, Noah-MP-PHS and these experimental configurations provide ideal testbeds to understand the impacts of plant hydraulic strategies on water and carbon cycles at a large spatial scale.

In this study, we extended our analysis to the contiguous United States (CONUS). We conducted a series of experiments with default SHSs and PHS (see method section for details). Our overarching goal is to understand the impact of plant hydraulics on water cycles, specifically the partitioning of total evapotranspiration to transpiration and the total water storage. Specifically, we analyzed the comparison (1) between the default SHSs experiments and PHS experiments with a plot-level configuration, (2) between PHS experiments with different hydraulic strategies (i.e., risk-prone vs. risk-averse), and also examined (3) how plant traits affect water cycles. Section 2 describes the default SHSs and new PHS in the Noah-MP, experimental design, and large-scale parameter estimation. Results are examined in Section 3, followed by conclusions and discussion in Section 4.

4.2 METHODS

4.2.1 The default Noah-MP and Noah-MP-PHS

The Noah-MP LSM is enhanced over the Noah LSM e.g., vegetation canopy energy and layered snowpack (Chen & Dudhia, 2001; Niu et al., 2011; Yang et al., 2011). Noah-MP is a primary model employed in the NASA Land Information System (Kumar et al., 2006), the next phase North American Land Data Assimilation System (Xia et al., 2012), the Weather Research and Forecasting model (Skamarock et al., 2019), and the National Water Model (Cosgrove et al., 2016). This model has been comprehensively evaluated in various climate regimes, including CONUS and China (Cai et al., 2014a & 2014b; Liang et al., 2019). Noah-MP implements alternative physical parameterization schemes for several vital processes. One of these is the plant water stress factor (β). In the default Noah-MP, there are three β schemes that employ an idealized "big-leaf" concept to regulate water and carbon fluxes in response to soil moisture stress through empirical soil hydraulics schemes (SHSs).

Li et al. (2020) implemented a novel plant hydraulics scheme (PHS) in Noah-MP (i.e., Noah-MP-PHS), which employs a big-tree rather than big-leaf concept, wherein the whole-plant hydraulic strategy is considered. Noah-MP-PHS was evaluated using plot-level observations from UMBS. Compared with default Noah-MP with SHS, Noah-MP-PHS better represents plant water stress and improves water and carbon simulations, especially during periods of dry soil conditions.

4.2.2 Experimental design

We conducted six experiments with default SHSs experiments and three extended PHS experiments based on Li et al. (2020) over the CONUS (Table 4.1). The SHSs experiments include three β schemes, i.e., Noah, CLM, and SiB schemes. For the PHS experiments, Li et al. (2020) calibrated three sets of PHS related parameters for the plot-level simulation, isohydric red maple tree-level simulation, and anisohydric red oak tree-level simulation. The plot-level experiment parameters are used to conduct CONUS plant hydraulics simulation and to compare with the COUNS default SHSs simulations. The parameters of the red maple experiment represent the "cavitation risk-averse" hydraulic strategy (hereafter risk-averse). The parameters of the red oak experiment represent the "cavitation risk-prone" hydraulic strategy (hereafter risk-prone). With the exception of the PHS risk-prone experiment with rooting depth of 10 m (i.e., 0.1, 0.3, 0.6, 9.0 m for the 1st – 4th layer), all other experiments used 2 m rooting depths (i.e., 0.1, 0.3, 0.6, 1.0 m for the 1st – 4th layer). All these experiments are conducted over the CONUS forest land covers.

Name	β Scheme	Rooting depth	SHS	PHS	Plot-level	Risk-averse strategy	Risk-prone strategy
SHS_avg	SHS_Noah	2m	√				
	SHS_CLM	2m					
	SHS_SiB	2m					
PHS_plot	PHS_plot	2m			√		
Risk-averse	PHS_map	2m		√		√	
Risk-prone	PHS_oak	10m					√

Table 4.1: Experiment configuration.

The 0.125° hourly atmospheric forcing, and static data, including topography, vegetation type, and soil type are from the North American Land Data Assimilation System (NLDAS) phase 2 (Mitchell et al., 2004; Xia et al., 2012; Zheng et al., 2019). The model spin-up was conducted for each experimental configuration to provide the initial conditions. The atmospheric forcing of the year 1980–2016 was used to drive the model, and then following 6-year simulation from 1980–1986. With the initial conditions on 1 January 1987, all experiments were run 30 years of 1987–2016.

4.2.3 PHS parameter calculation

Li et al. (2020) calibrated most of PHS parameters for the red maple, red oak, and mixed experiments (Table 4.2). The static spatial parameters, i.e., the sapwood area index (S_{sap}), sapwood volume index (V_{sap}) and canopy height (H_c), are needed to prepare CONUS simulations. The PHS experiments use the same spatial values of canopy height, sapwood area index and sapwood volume index. H_c can directly use the global datasets of canopy height (Simard et al., 2011) as a proxy.

Parameter	Description	Unit	Source	Risk-averse (Maple)	Risk-prone (Oak)	Plot
TLP	Turgor loss point (LWP when photosynthetic capacity rate halves)	mm	Li et al. (2020)	-0.7E+5	-2.0E+5	-1.5E+5
C_{leaf}	Leaf water capacitance	1	Li et al. (2020)	1.0E-7	1.0E-7	1.0E-7
$K_{s,sat}$	Sapwood-area-specific saturated xylem hydraulic conductivity	mm/s	Li et al. (2020)	1.0E-2	1.5E-2	2.0E-2
P_{50}	Stem water potential at 50% loss of conductivity	mm	Li et al. (2020)	–2.0E+5	–1.5E+5	–2.0E+5
C_{stem}	Stem water capacitance	m^{-1}	Li et al. (2020)	7.0E-4	1.0E-4	4.0E-4
S_{sap}	Specific sapwood area index	m^2/m^2	Calculated in this study	Figure 4.1		
V_{sap}	Specific sapwood volume index	m^3/m^2	Calculated in this study	Figure 4.1		
H_c	Canopy height	m	Simard et al. (2011)	Figure 4.1		
a_1	Empirical parameter controlling length of water flow route	unitless	Li et al. (2020)	4.0E-1	4.0E+0	1.0E+0
a_2	Empirical parameter controlling xylem hydraulic conductance	unitless	Li et al. (2020)		4.0E+0	
a_3	Empirical parameter controlling plant water stress	unitless	Li et al. (2020)		6.0E+0	
$f_{root-shoot}$	Fine root area to shoot (i.e., leaf area + stem area) ratio	unitless	Li et al. (2020)	9.0E+0	1.0E-1	1.0E+0

Table 4.2: Parameters for PHS simulations.

The S_{sap} and V_{sap} are calculated based on the species-specific allometric equations as follows:

(1) Calculation of the diameter at breast height (DBH, m). Garrity et al. (2011) built an allometric equation based on the tree measurements on the University of Michigan Biological Station (UMBS).

$$DBH = \exp\left(\frac{H_c + 12.61}{9.97}\right) \quad \text{(Eq. 4.1)}$$

where, the unites of DBH and H_c are cm and m, respectively.

(2) Calculation of S_{sap} (units: m^2/m^2). Tree level sapwood area (TSA, units: m^2) is first calculated based on an allometric equation,

$$\text{TSA} = (\alpha_1 + \alpha_2 DBH^{\alpha 3}) \times 10^{-4} \quad \text{(Eq. 4.2)}$$

where, the species-specific parameters of α_1, α_2 and α_3, are -110.66, 17.04 and 1.00 for red maple (Bovard et al., 2005), and 0.00, 0.21, and 2.18 for red oak (Matheny et al., 2014b), respectively.

The computed TSA for red maple (TSA_m) and red oak (TSA_o) are averaged as $\overline{\mathrm{TSA}}$. Global tree density (TRD, units: m^{-2}; Crowther et al., 2015) is used to transfer the tree-level value into the ground-area specific value, i.e., S_{sap}

$$\overline{\mathrm{TSA}} = (\mathrm{TSA_m} + \mathrm{TSA\_o})/2 \quad \text{(Eq. 4.3)}$$

$$S_{sap} = \overline{\mathrm{TSA}} \times TRD \quad \text{(Eq. 4.4)}$$

(3) Calculation of V_{sap} (units: m^3/m^2). We assume that the sapwood is not change at each stem cross-section vertically. So,

$$V_{sap} = H_c \times S_{sap} \quad \text{(Eq. 4.5)}$$

These spatial plant traits are used in PHS experiments, and also can help to analyze how plant traits can affect the water and carbon fluxes, corresponding the goal (3).

4.2.4 Analysis

In this study, we focused two types of comparisons. The 1st is the difference between the default SHSs simulations and PHS_plot simulation, which corresponds to research goal (1); the 2nd is the difference between PHS simulations with different hydraulic strategies, which corresponds to research goal (2). Also, we analyzed the impacts of plant traits on these simulations, corresponding to research goal (3).

The analysis focuses on the climatology (i.e., 1987–2016) over CONUS. We also selected the forest regions experienced 2011 Texas drought. We used the 2-digit hydrologic unit code (HUC02) of United States Geological Survey (USGS) to help forest area selection (Figure 4.14). The Gravity Recovery and Climate Experiment (GRACE) satellite-derived terrestrial water storage anomaly (TWSA) data are used to examine the overall

model TWSA simulations. The simulated TWS is the sum of soil moisture, snow water equivalent (SWE), canopy water content, and plant water storage. The GRACE/GRACE-FO RL06 Mascon Solutions (version 02) was downloaded from the Center for Space Research (Save et al., 2016). All of these datasets are resampled to NLDAS resolution.

4.3 RESULTS

4.3.1 Spatial plant traits

Based on the assumptions and species-specific allometric equations above, we calculated sapwood area index (Figure 4.1c) and sapwood volume index (Figure 4.1d) on the basis of canopy height (Figure 4.1a) and tree density (Figure 4.1b). Generally, there are two hot spots with large value of these two indexes: the northwest and eastern US. These regions are characterized by large values of canopy height and/or tree density. The PHS experiments use the same spatial map of canopy height, sapwood area and sapwood volume indexes.

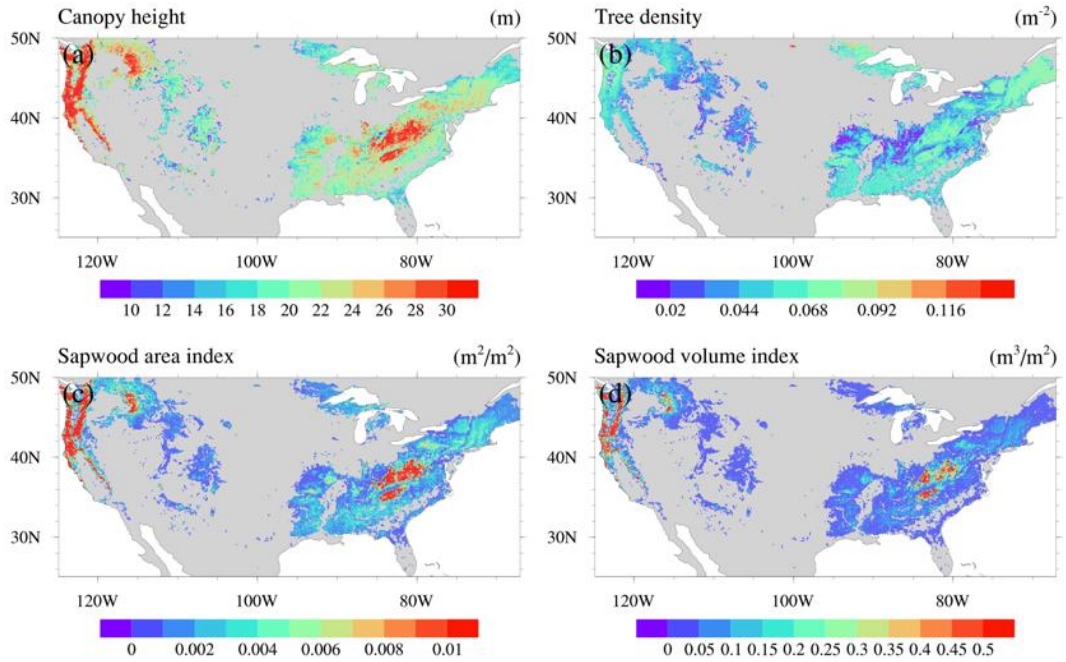

Figure 4.1: (a) Tree canopy height, (b) tree density, (c) calculated sapwood area index, and (d) calculated sapwood volume index over CONUS forest regions.

4.3.2 Climatology comparison

We calculated the climatology of water and carbon variables throughout 1987–2016 for different experiments. Considering transpiration mainly occurs during the growing season, the climatology was calculated based on each year's growing season, i.e., April–October. Specifically, we analyzed the comparisons (1) between the average of SHSs simulations (SHS_avg) and the PHS simulation with calibrated plot-level experiment parameters (PHS_plot), and (2) between the PHS simulation with "cavitation risk-averse" strategy using calibrated maple experiment parameters (Risk-averse) and the PHS simulation with "cavitation risk-prone" strategy using calibrated oak experiment parameters (Risk-prone).

4.3.2.1 ET partitioning

Figure 4.2 shows the climatology of TR/ET. PHS_plot experiment has similar spatial patterns of transpiration partitioning with the SHS_avg simulations, with larger TR/ET over the southeastern and northwestern forest regions. Even though the overall averages of TR/ET are the same as 0.55 for these two simulations, the PHS_plot experiment has a larger TR/ET for the majority of regions (Figures 4.2a–2c). Plant hydraulic traits are closely related to the difference between PHS_plot and SHS_avg experiments. PHS_plot simulation shows a higher ratio of transpiration over forest regions with larger values of tree density, canopy height, sapwood area, and volume indexes (Figures 4.3a–3d).

For the PHS experiment with different hydraulic strategies, the risk-averse and the risk-prone experiments show similar spatial patterns (Figures 4.2d and 4.2e). Even though the overall averages of TR/ET are quite identical, these two experiments show apparent disagreement in the spatial patterns of TR/ET over CONUS (Figures 4.2f). The risk-prone

strategy tends to have a larger transpiration ratio than the risk-averse strategy with canopy height taller than about 25 m (Figures 4.3e–3h).

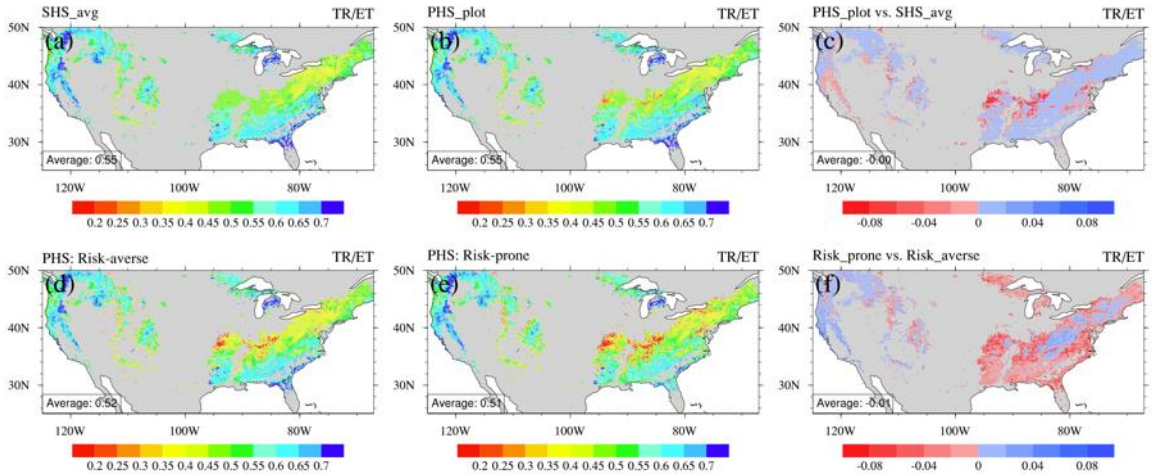

Figure 4.2: Comparisons of TR/ET for difference experiments. (a) the averaged SHS experiments, (b) the PHS_plot experiment, and (c) their difference (i.e., PHS_plot – SHS_avg); (d) the PHS risk-averse experiment, (e) the PHS risk-prone experiment, and (f) their difference (i.e., risk-prone – risk-averse).

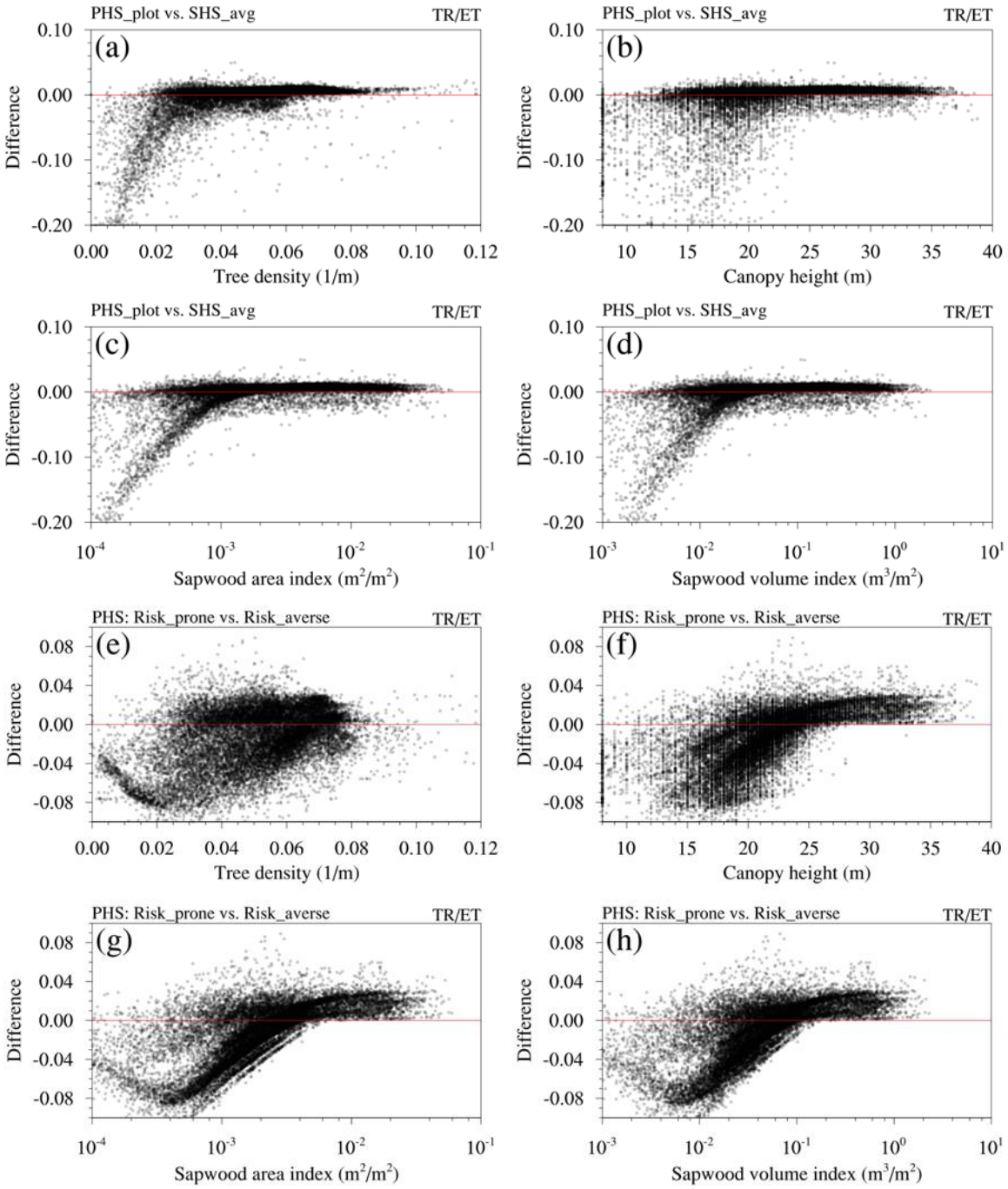

Figure 4.3: The relationships between TR/ET difference and plant traits. Figures (a) – (d) corresponds to the TR/ET difference between PHS_plot and SHS_avg experiments. Figures (e) – (h) corresponds to the TR/ET difference between PHS risk-prone and PHS risk-averse experiments.

4.3.2.2 Transpiration and plant water stress (β)

To better understand the TR/ET patterns, we further analyzed transpiration and β. The SHS_avg and PHS_plot have similar spatial patterns of transpiration. Overall, the plant hydraulics scheme has slightly larger transpiration than the transpiration average of the default soil hydraulics schemes (Figures 4.4a–4c). Plant traits affect the transpiration difference between these two experiments. The PHS_plot experiment tends to have smaller transpiration than the SHS_avg experiment over forest regions with low tree density, canopy height, sapwood area index, and sapwood volume index (Figures 4.5a–5d). The transpiration patterns are consistent with the plant water stress factor (β) (Figures 4.6a–6d), reflecting the influence of plant water stress on stomatal conductance. PHS experiments show overall larger β than the averaged SHS experiments except for regions with small values of plant traits (Figures 4.7e–7h).

For the PHS experiments with different hydraulic strategies, the risk-averse experiment has larger transpiration than the risk-prone experiment (Figures 4.4d–4f). Plant traits affect the transpiration difference between two different hydraulic strategies (Figures 4.5e–5h). The risk-prone strategy tends to have larger transpiration than the risk-averse strategy when canopy height is higher than approximately 25 m. These transpiration patterns are consistent with the patterns of plant water stress factor for two PHS experiments (Figures 4.6d–6f). The risk-prone experiment has larger β than the risk-averse experiment over regions with larger values of canopy height, sapwood area, and volume indexes (Figure 4.7f).

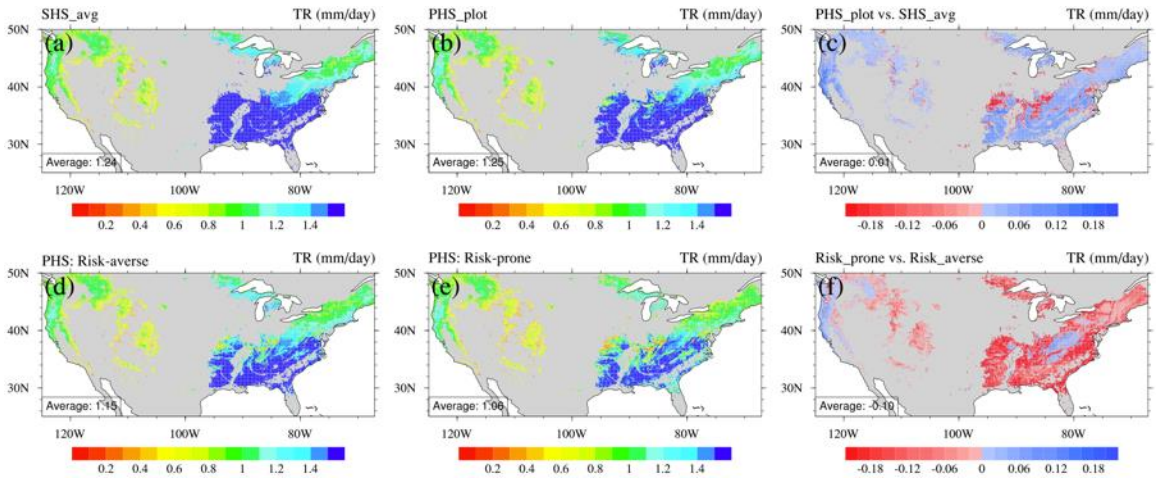

Figure 4.4: Similar to Figure 4.2 but for transpiration (TR).

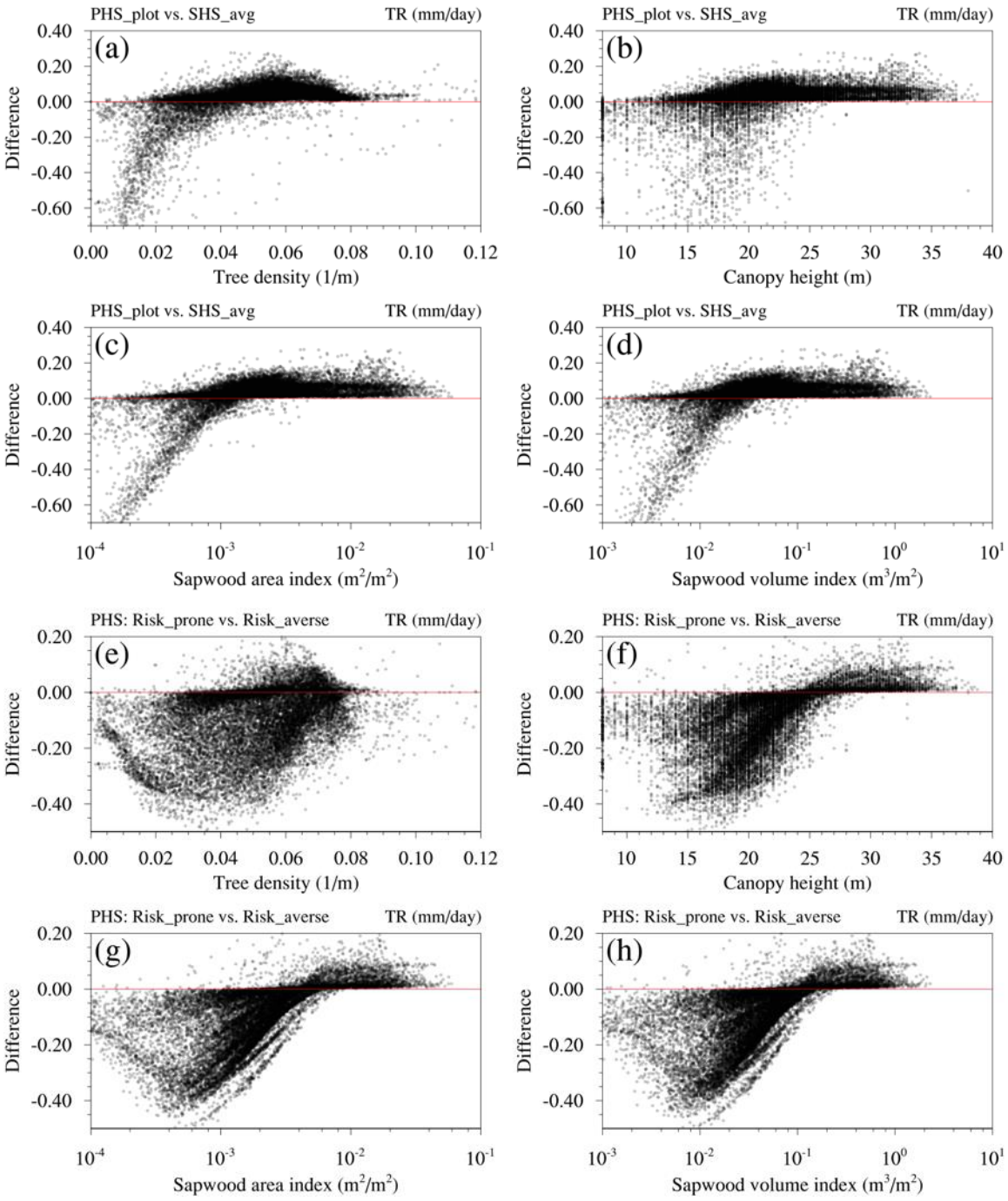

Figure 4.5: Similar to Figure 4.3 but for transpiration (TR).

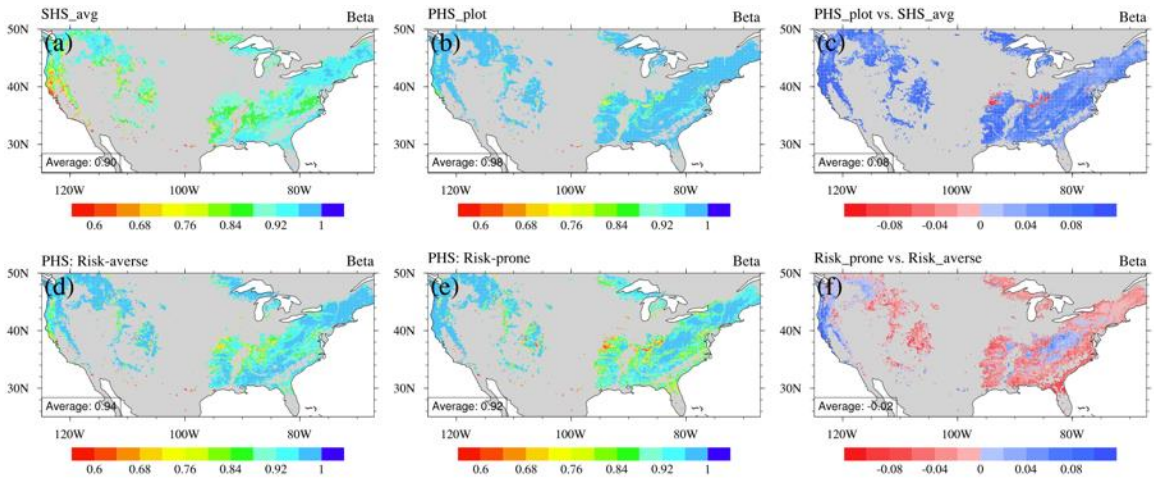

Figure 4.6: Similar to Figure 4.2 but for plant water stress (β).

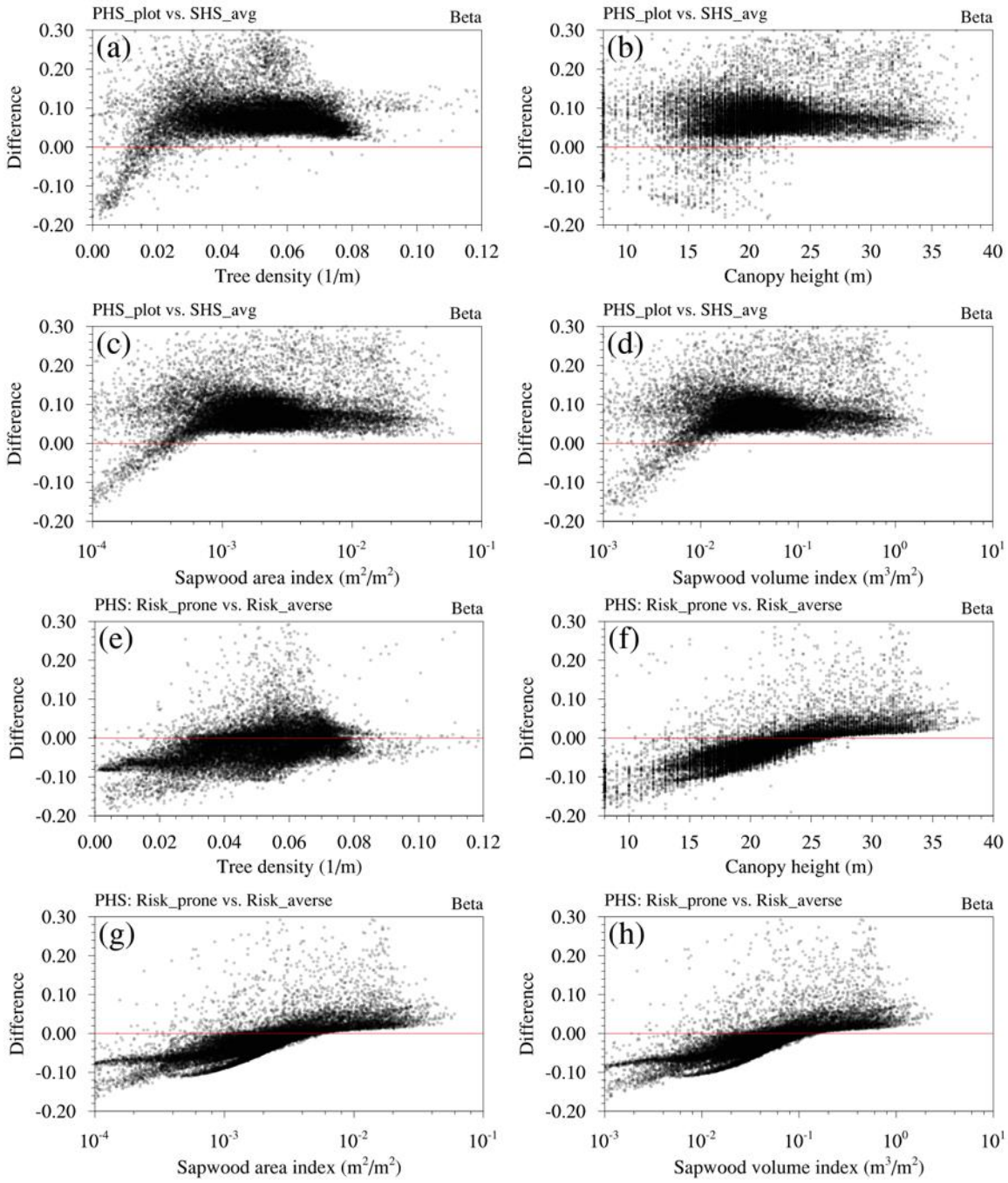

Figure 4.7: Similar to Figure 4.3 but for plant water stress (β).

4.3.2.3 Evapotranspiration

The SHS_avg and PHS_plot have similar spatial patterns of total evapotranspiration (ET). Overall, the plant hydraulics scheme has a slightly larger ET than the average of the default soil hydraulics schemes (Figures 4.8a–8c). PHS has smaller ET over regions with low values of plant traits, i.e., tree density, canopy height and sapwood area and volume indexes (Figure 4.9a–9d), which is consistent with the transpiration patterns. Another major component of ET is the soil evaporation (ES, Figure 4.15). Overall, PHS has larger ES than SHS average, especially for the regions with small values of plant traits (Figure 4.16). These patterns are consistent with the 1st layer soil moisture (Figures S4.4 and S4.5) that PHS experiment has wetter topmost layer soil moisture than the SHS experiments.

For the PHS experiments with different hydraulic strategies, the risk-averse experiment has a larger ET than the risk-prone experiment (Figures 4.8d–8f). Plant traits strongly affect the ET difference between different hydraulic strategies (Figures 4.9e–9h). The ET difference becomes smaller with canopy height increases, consistent with the patterns of transpiration. The risk-averse experiment has wetter top layer soil moisture (Figure 4.17 and S4.5) and hence has larger soil evaporation than those of the risk-prone experiment (Figures S4.2–S4.3).

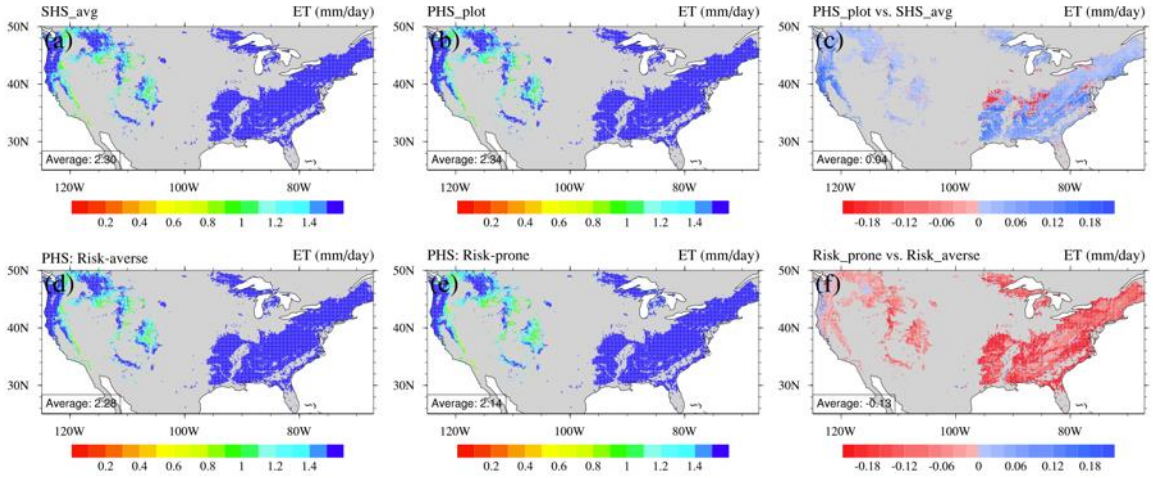

Figure 4.8: Similar to Figure 4.2 but for total evapotranspiration (ET).

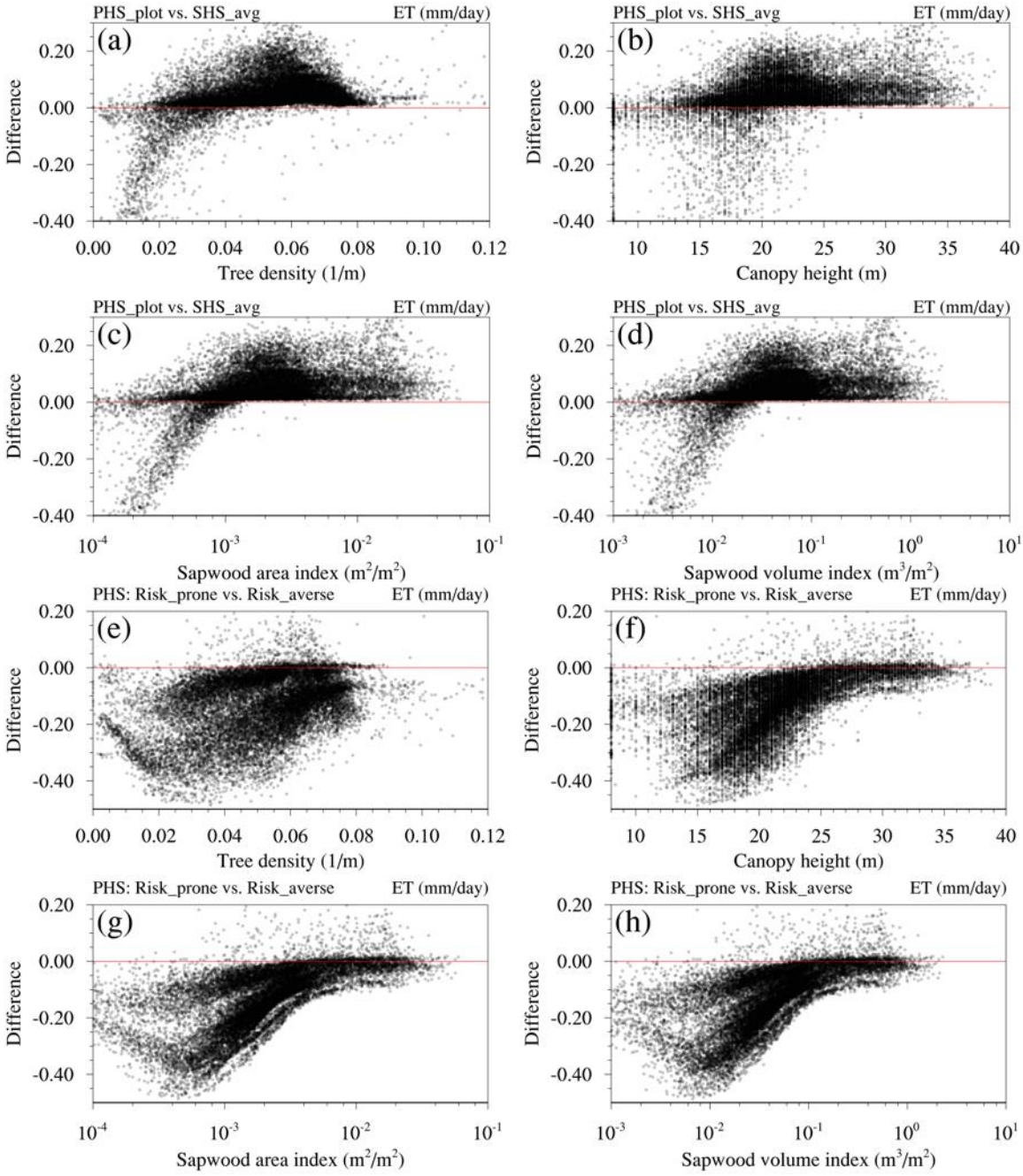

Figure 4.9: Similar to Figure 4.3 but for total evapotranspiration (ET).

4.3.3 TWS comparison

4.3.3.1 TWS amplitude

Figure 4.10 shows the TWS seasonal amplitudes of model simulations and the GRACE dataset. The simulated TWS is the sum of soil moisture, snow water equivalent (SWE), plant water storage, and canopy water content. Overall, model simulations show consistent spatial patterns with each other. The pixel averages of simulated TWS amplitudes (i.e., 18.51–20.29 cm) are slightly more than the GRACE dataset (i.e., 17.54 cm). Specifically, compared with GRACE TWS, model simulations overestimate the TWS amplitude over the western US, which is likely due to the large SWE amplitude (Figure 4.20). While for the central-southern regions, model simulations underestimate the TWS amplitude, which likely due to the omission of groundwater variations in the current experiments.

The overall difference of TWS amplitude between PHS_plot and SHS_avg experiments is 0.70 cm, which accounts for 4.24% of the GRACE TWS amplitude (Figures 4.10c and 4.10h). The PHS_plot experiment has a smaller soil moisture amplitude than the averages of default SHS experiments over forest regions with sparse trees (Figure 4.19 and Figure 4.1).

However, for PHS risk-averse and risk-prone experiments, their TWS amplitude difference is quite apparent with 5.94 cm, accounting for 37.57% of the GRACE TWS amplitude (Figures 4.10f and 4.10h). The risk-prone strategy tends to have smaller (larger) simulated TWS amplitudes in the central-western US (western and eastern US) than that of risk-averse strategy. The soil moisture amplitude of the risk-prone strategy simulation is larger than that of risk-averse strategy over the central-western US, while the SWE amplitude between these two experiments is much smaller (Figure 4.19).

As simulated TWS is dominated by soil moisture and SWE, why does the risk-prone strategy not have a larger TWS amplitude than risk-averse strategy over the central-western US region? We analyze the time series of the TWS anomaly (TWSA), soil moisture anomaly (SMA) for all soil layers, and SWE anomaly (SWEA) for the forest regions in HUC 14 watershed over the western US (Figure 4.21). The risk-prone experiment has different soil moisture amplitudes and notable timing differences compared with the SMA of the risk-averse experiment (Figure 4.22). There is an offset due to the timing difference between SWA and SMA for the risk-prone experiment, causing the risk-prone experiment to have a smaller overall TWS amplitude than that of the risk-averse experiment.

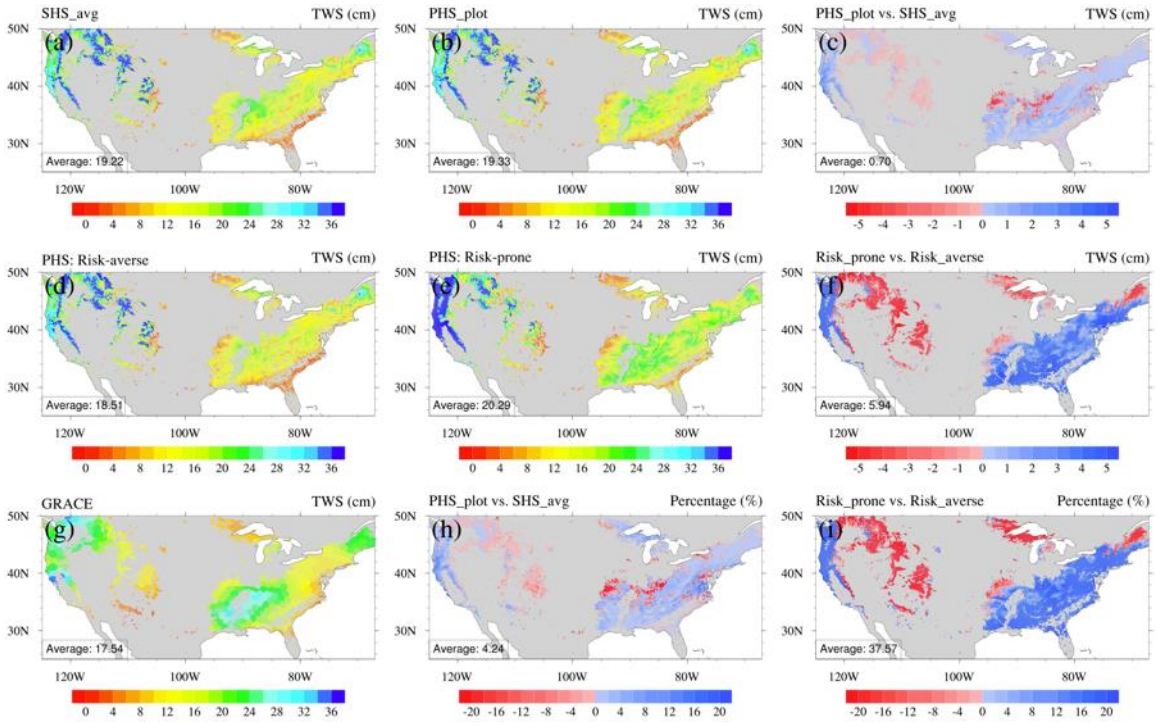

Figure 4.10: Comparison of seasonal TWS amplitudes (2004–2010) for different experiments. (a) – (c) TWS amplitudes for the averaged SHS experiments, the PHS_plot experiment, and their difference (i.e., PHS_plot – SHS_avg), respectively; (d) – (e) TWS amplitudes for the PHS risk-averse experiment, the PHS risk-prone experiment, and their difference (i.e., risk-prone – risk-averse), respectively. (g) GRACE TWS amplitude; (h) Ratio of the TWS amplitude difference between PHS_plot and SHS_avg to the GRACE TWS amplitude; (i) Ratio of TWS amplitude difference between risk-averse and risk-prone to the GRACE TWS amplitude. The average in each figure calculated as the average of the absolute value in each pixel.

4.3.3.2 Continental-scale TWS

Figure 4.11 shows the monthly averages of TWSA, SMA, SWEA over the CONUS forest regions during 2003–2016. Overall, the TWSA of the PHS_plot experiment shows slightly better agreement with GRACE TWSA than that of the SHS_avg experiment, with larger r and smaller RMSE (Table 4.3). For PHS experiments with different plant hydraulic strategies, TWSA of the risk-prone experiment is more consistent with GRACE TWSA than the TWS of the risk-averse experiment, with larger r and smaller RMSE (Table 4.3). As there is no difference of SWEA, the TWSA difference is determined by the SMA difference regarding the different SMA amplitude and/or timing.

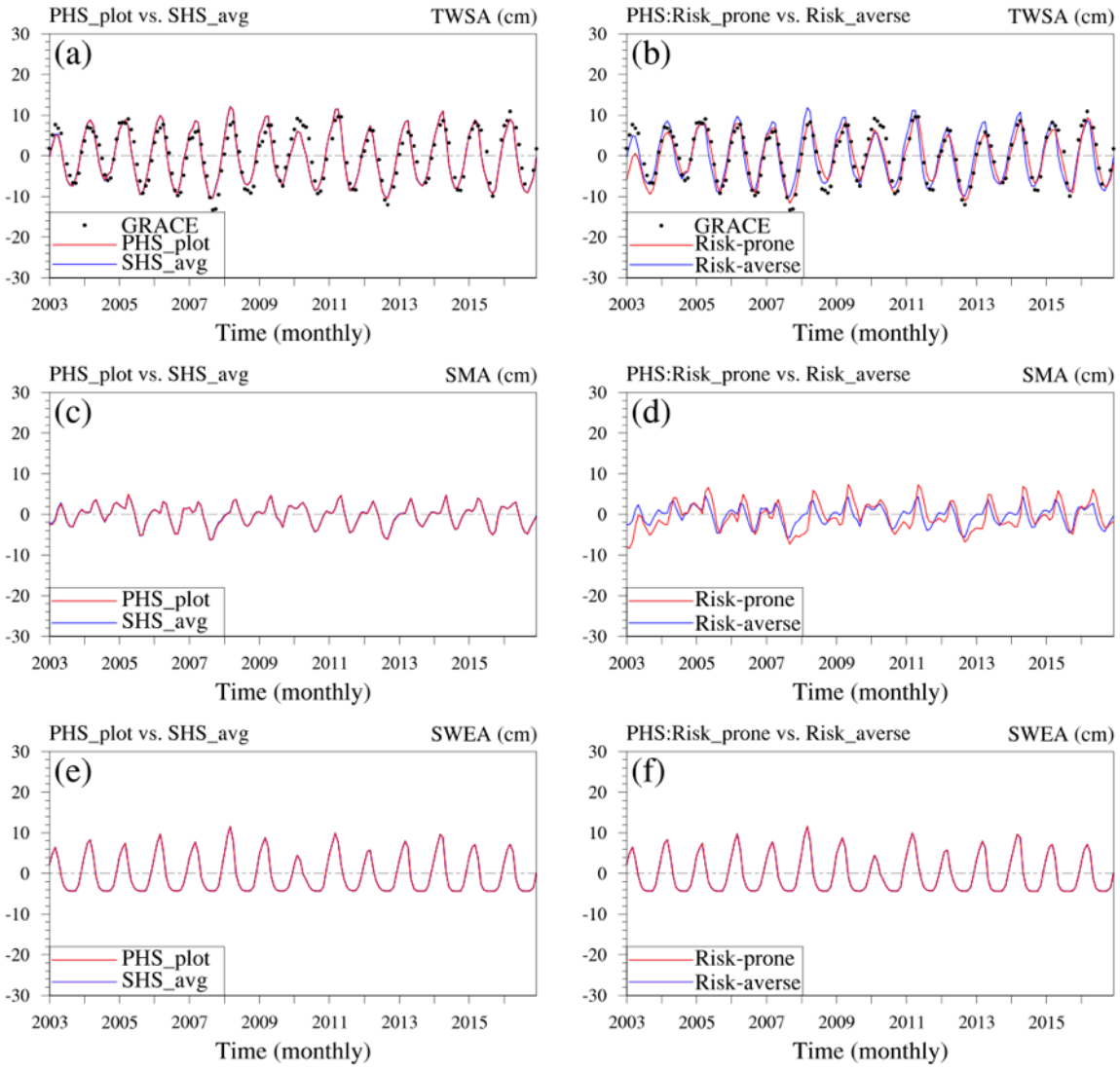

Figure 4.11: Monthly CONUS averages of TWSA, SMA, SWEA for the PHS_plot vs. SHS_avg experiments (Figures in the left column), and PHS risk-averse vs. PHS risk-prone experiments (Figures in the right column) during 2003–2016.

Experiments	r	RMSE (cm)
SHS_avg	0.89	2.91
PHS_plot	0.90	2.87
PHS risk-averse	0.89	2.90
PHS risk-prone	0.94	2.23

Table 4.3: Statistical summary of simulated TWSA for different experiments by comparing with GRACE TWSA during 2003–2016 over CONUS forest regions (r, correlation coefficient; RMSE, root-mean-square error).

Experiments	r	RMSE (cm)
SHS_avg	0.88	8.33
PHS_plot	0.90	7.68
PHS risk-averse	0.89	7.99
PHS risk-prone	0.91	5.90

Table 4.4: Statistical summary of simulated TWSA for different experiments by comparing with GRACE TWSA during 2009–2011 over eastern Texas regions.

4.3.3.3 TWS during drought

To analyze the simulations during drought years, we selected a forest region in eastern Texas and the adjacent area (Figure 4.23), and calculated regional averages for different experiments from 2009 to 2011 (Figures 4.12 and 4.13).

Compared with the TWSA of the default soil hydraulics schemes, the TWSA of PHS_plot shows a slight decrease during the dry-down period in 2010 and 2011 (Figure 4.12a), and hence is more consistent with GRACE TWSA with larger r and smaller RMSE (Table 4). The simulated TWSAs are primarily determined by the soil moisture anomalies (SMAs) (Figure 4.12h). In 2011, the PHS_plot experiment has larger transpiration and ES (and their sum of ET) than these of SHS_avg simulations (Figures 4.12b–12d). The plant hydraulics scheme tends to have larger β and top layer soil moisture, favoring larger TR and ES (Figures 4.12d and 4.12e). Compared with the SHS_avg experiments, the PHS experiment uses less soil moisture from the shallow 1st and 2nd layers, but more soil moisture from deeper 3rd and 4th layers (Figures 4.12g, 4.12h, 4.12j and 4.12k).

For the PHS experiments with different hydraulic strategies, the risk-prone experiment has larger TWSA decrease than the TWSA of the risk-averse experiment during the dry-down period of 2010 and 2011 (Figure 4.13a), which is more consistent with GRACE TWSA with larger r and much smaller RMSE (Table 4.4). The simulated TWSAs are also determined to a large degree by the SMA (Figure 4.13h). The TWSA of the risk-prone experiment shows enhanced consistency with the GRACE TWSA than that of the risk-averse experiment. The risk-prone experiment used more soil moisture from the 4th layer but less soil moisture from the 1st layer for transpiration (Figure 4.24), and had wetter 1st layer soil moisture and supporting larger ES losses in 2011.

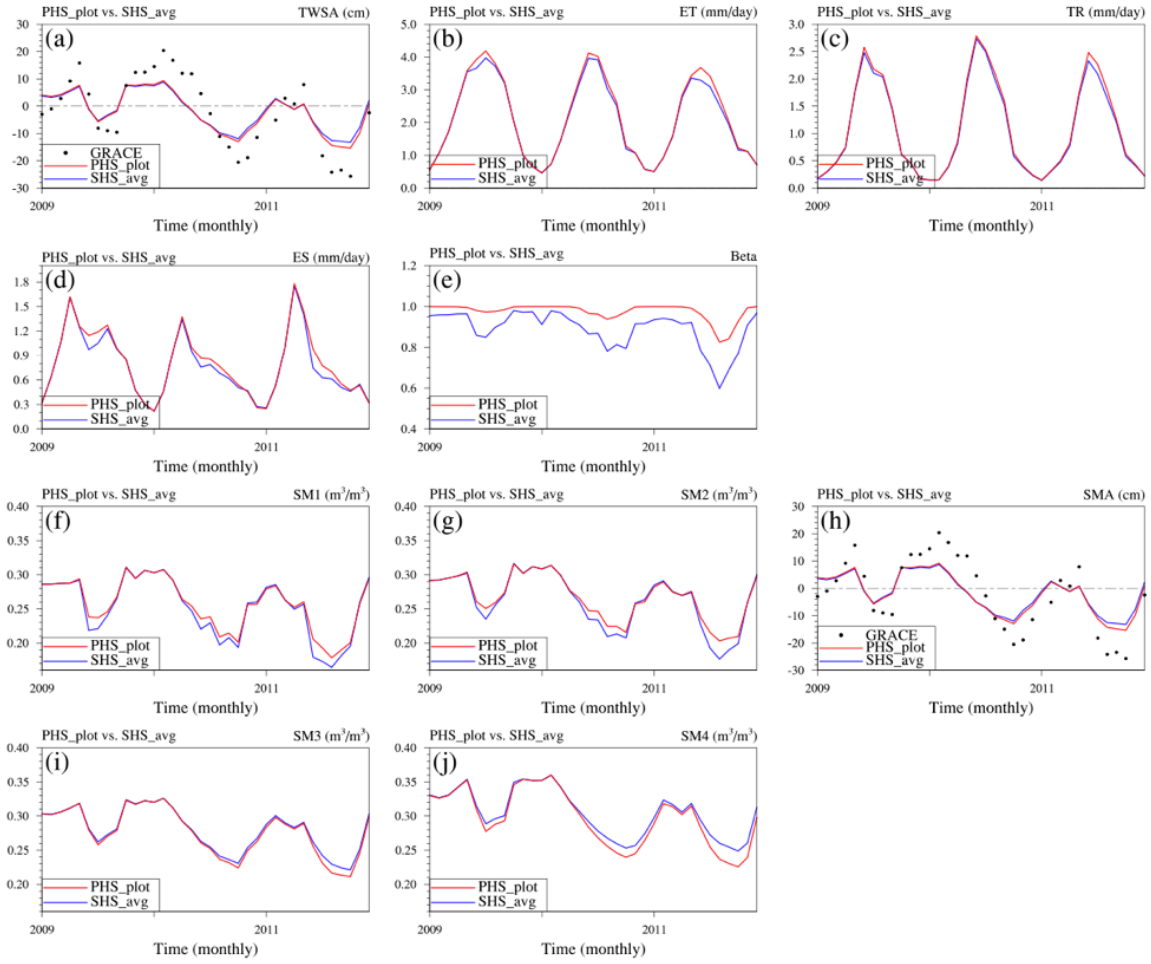

Figure 4.12: Monthly regional averages for the SHS_avg experiment and the PHS_plot experiment during 2009–2011. SMA, SM1, SM2, SM3, SM4 denote total soil moisture anomaly, and soil moisture at 1st, 2nd, 3rd, and 4th layer, respectively.

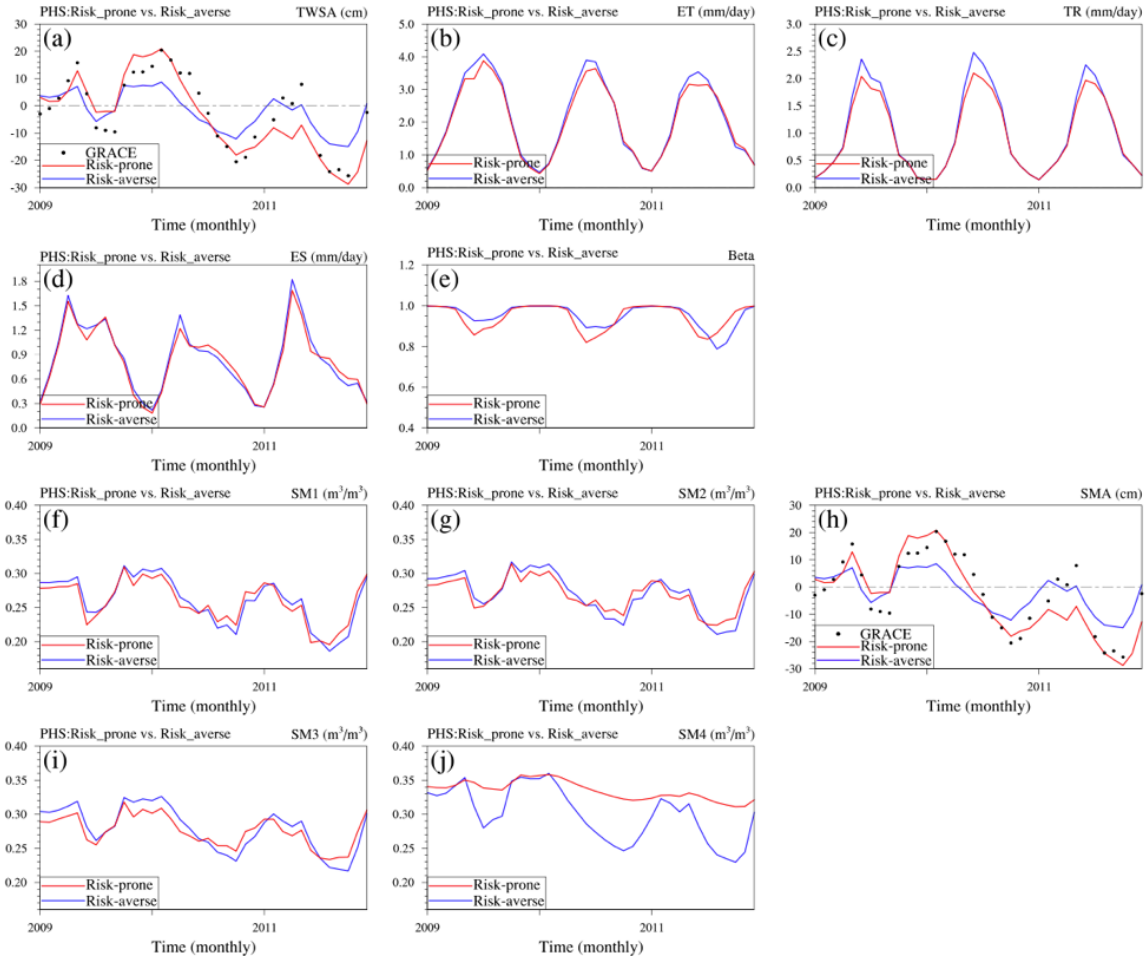

Figure 4.13: Similar to Figure 4.12 but for PHS risk-averse and PHS risk-prone experiments.

4.4 DISCUSSION AND CONCLUSIONS

In this study, we extended the plot-level and tree-level PHS experiments to larger spatial scales over the CONUS forest regions. To conduct PHS experiments, we first calculated the spatial sapwood area and volume indexes over CONUS forest regions based on a series of assumptions alongside datasets of forest canopy height and tree density. To the best of our knowledge, these indexes have not yet been used within land surface modeling. Therefore, in addition to the default three experiments, we designed three PHS experiments, including PHS_plot, PHS risk-averse, and risk-prone experiments based on the calibrated PHS parameters from UMBS plot-level, maple tree level and oak tree-level simulations, respectively (Li et al., 2020). We compared the model simulations between PHS_plot and SHS_avg experiments, and between PHS risk-averse and risk-prone experiments.

The CONUS TR/ET average of the PHS_plot experiment is roughly equal to that of the SHS_avg simulation. The spatial patterns of TR/ET differences between these two simulations are related to the plant traits of tree density and canopy height. The PHS_plot simulation shows a higher ratio of transpiration over forest regions with larger values of tree density and canopy height. It should be noted that the tree density dataset only included individual trees with woody stems larger than 10 cm in diameter at breast height (Crowther et al., 2015). The calculated sapwood area and volume indexes are likely underestimated via the exclusion of small trees, hence underestimating the transpiration and TR/ET of PHS experiments. Therefore, the consideration of smaller trees and potentially other non-tree plants, PHS experiments could produce larger TR/ET.

The overall averages of TR/ET climatology for PHS risk-averse and risk-prone experiments are similar, but slightly smaller than the PHS_plot experiment. The risk-averse and risk-prone experiments are based on the parameters calibrated from the maple or oak

tree-level experiments. The tree-level simulations represent the plant water transport for a given single tree over its crown area, without considering transpiration from overlapping neighbor trees. Therefore, the risk-averse and risk-prone simulations implicitly representing relatively sparse forests without tree overlapping. For the PHS_plot experiment, parameters were calibrated using plot-level observations representing all tree species over the flux footprint area, and implicitly considering canopy overlap. Therefore, the PHS_plot experiment has larger xylem hydraulic conductivity than risk-averse and risk-prone experiments (Table 4.2), and hence has larger TR and TR/ET. Plant traits (i.e., canopy height and tree density) also affect the TR/ET difference between risk-averse and risk-prone experiments. The risk-prone experiment has a smaller (larger) transpiration ratio than the risk-averse strategy with lower canopy height (taller) than about 25 m. Forests with larger values of tree density and canopy height have a larger sapwood area index, which likely affects the xylem hydraulic conductance for risk-averse and risk-prone strategies and hence the transpiration.

Plant hydraulics could improve the TR/ET simulations. Previous TR/ET climatology analysis was calculated over the growing season. We further calculated the TR/ET by annual climatology to compare with TR/ET of other studies (Table 4.5). In the CONUS, there are three major types of forests, including evergreen needleleaf forest (ENF), deciduous broadleaf forest (DBF) and mixed forest (MF). The simulated TR/ET of both SHS and PHS experiments are comparable with other studies for the DBF and MF. While for DBF, model simulations underestimate TR/ET compared with other studies (0.34–0.41 vs. 0.52–0.64, Table 4.5). Our analysis has shown that plant traits can affect TR/ET of PHS simulations over DBF regions (Figure 4.25 and Figure 4.26). Therefore, with more realistic representations of sapwood area and volume indexes, along with more

realistic representation plant hydraulics strategies, PHS has the potential to improve simulated TR/ET for the DBF.

Forest types	SHS_avg	PHS_plot	Risk-averse	Risk-prone	Study 1	Study 2	Study 3	Study 4
Evergreen needleleaf forest	0.57	0.58	0.57	0.56	0.55[a]	0.50	0.56	0.49
Deciduous broadleaf forest	0.41	0.39	0.36	0.34	0.61[b]	0.64	0.52	0.59
Mixed forest	0.57	0.58	0.55	0.53	0.55	0.57	--	0.59

Table 4.5: Comparison of TR/ET for three typical forest types among different studies. Study 1: Wei et al. (2017); Study 2: Wang-Erlandsson et al. (2014); Study 3: Zhou et al. (2016); Study 4: Gu et al (2018).
a: average of all needleleaf forest, including evergreen needleleaf forest and deciduous needleleaf forest.
b: average of all broadleaf forest, including evergreen broadleaf forest and deciduous broadleaf forest.

For the TWS amplitude, all experiments show consistent spatial patterns over CONUS forest regions and generally capture the GRACE TWS spatial patterns. Compared with the GRACE TWS, model simulations overestimate the TWS amplitude over the western US, probably due to the large simulated SWE amplitude. Over the central southern regions, model simulations underestimate the TWS amplitude, which perhaps is due to the omission of groundwater in current experiments. It should be noted that Noah-MP has options to consider a simple unconfined aquifer. Cai et al. (2014b) showed that groundwater is an essential contributor to simulated TWS. Other factors, including water fluctuations in rivers and lakes, could also influence the disagreement between simulated TWS and GRACE TWS (Cai et al., 2014b).

The PHS_plot experiment has slightly larger TWS amplitude than the SHS_avg experiments, accounting for 4.24% of the GRACE TWS on average over CONUS, mostly due to the difference between their SM amplitudes. Similarly, the monthly CONUS

averaged TWSA of the PHS_plot experiment is slightly better consistent with GRACE TWS than the SHS_avg experiment. Furthermore, during the 2011 drought period, PHS_plot slightly better captures the TWSA over the eastern Texas forest regions than SHS_avg simulations. Even though based on the parameters calibrated at one single site and used the sapwood area and volume indexes calculated from a series of assumptions, PHS_plot can capture consistent or better patterns of water simulations compared with default SHS experiments.

Different plant hydraulic strategies have considerable influence on the simulated TWS variation. The CONUS average of TWS amplitude difference between these two experiments accounts for overall 37.57% of the GRACE TWS variation. The risk-prone experiment tends to have smaller (larger) simulated TWS amplitude in central-western US (western and eastern US) than that of the risk-averse experiment, due to different timing and amplitude of their soil moisture variations. For the 2011 Texas drought analysis, the risk-prone experiment better captured the GRACE TWSA compared with the risk-averse experiment. It should be noted that the PHS_plot experiment implicitly represents a comprehensive hydraulic strategy of multiple species at the UMBS site. This site has red maple and red oak that the risk-averse and risk-prone experiments are based on, and also includes species such as bigtooth aspen, paper birch, sugar maple, white pine, and American beech (Matheny et al., 2014). Therefore, the PHS_plot experiment's comprehensive hydraulic strategy is intermediate to the risk-averse hydraulic strategy and risk-prone strategy. Thus, the PHS_plot experiment has the intermedium performance of TWSA simulations, which is between the model performance of risk-averse experiment and risk-prone experiment (Table 4.4).

4.5 SUPPLEMENTARY

Figure 4.14: Hydrologic unit code (USGS). USGS Watershed Boundary Dataset structure visualization (source: https://www.usgs.gov/media/images/watershed-boundary-dataset-structure-visualization).

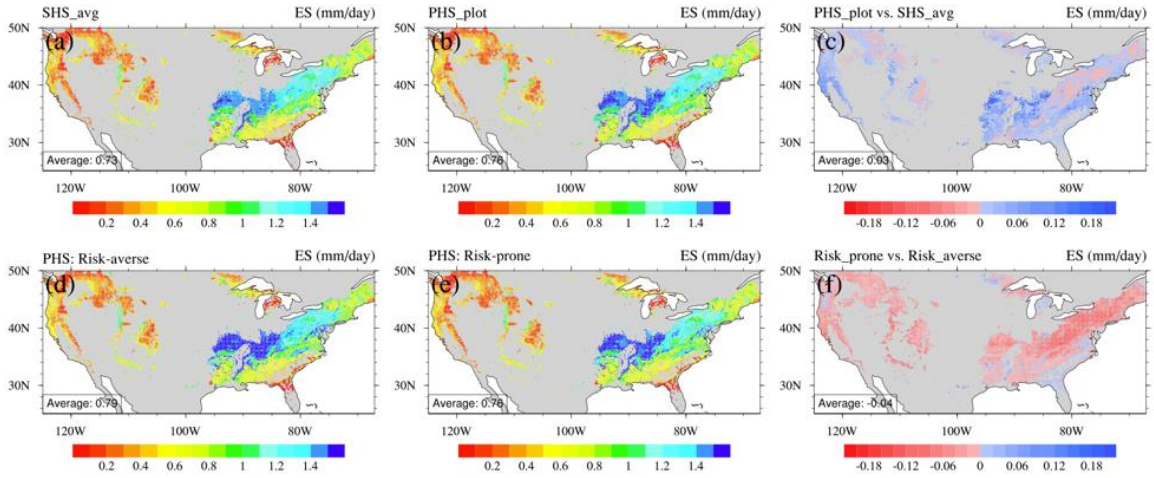

Figure 4.15: Similar to Figure 4.2 but for soil evaporation (ES).

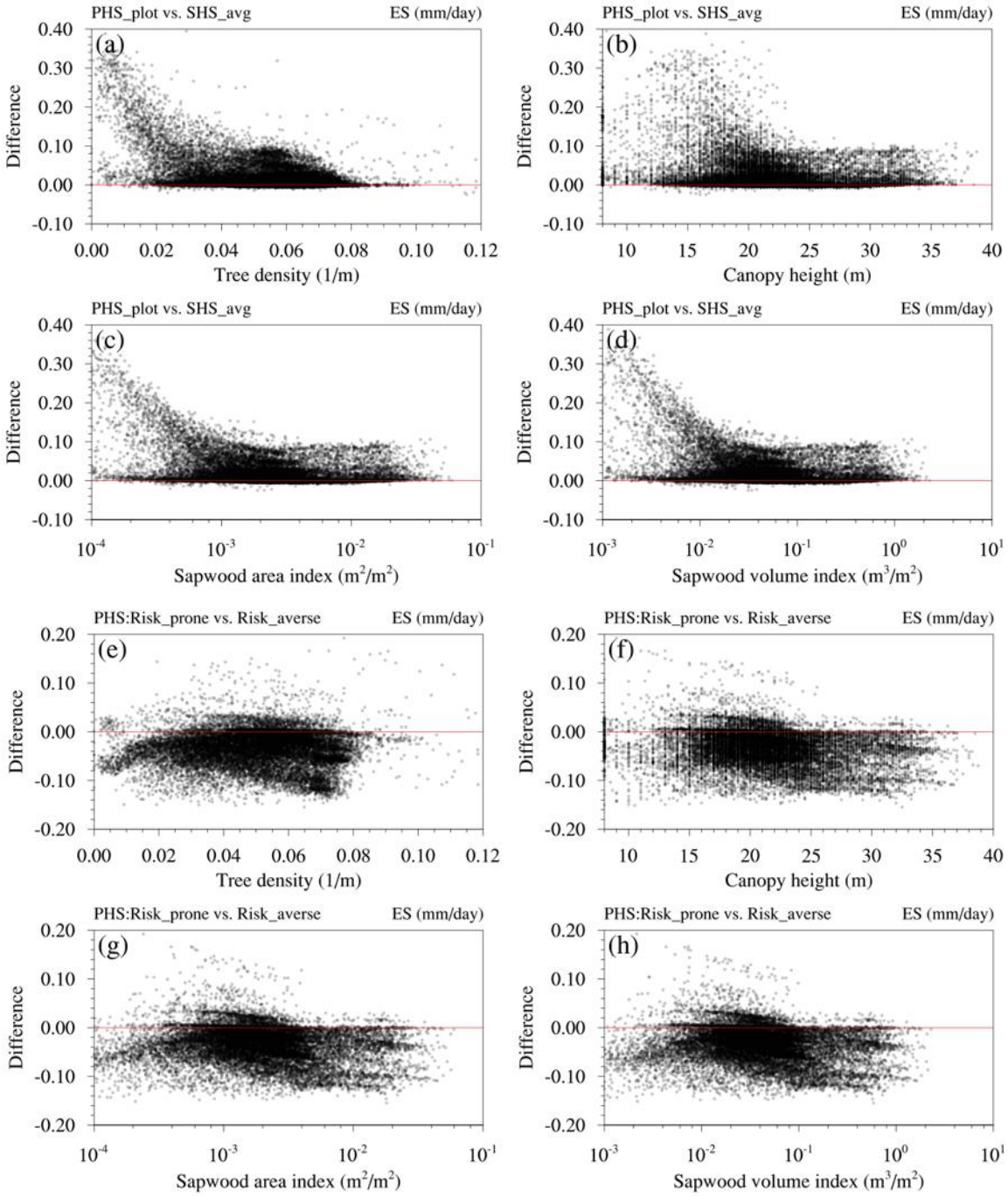

Figure 4.16: Similar to Figure 4.3 but for soil evaporation (ES).

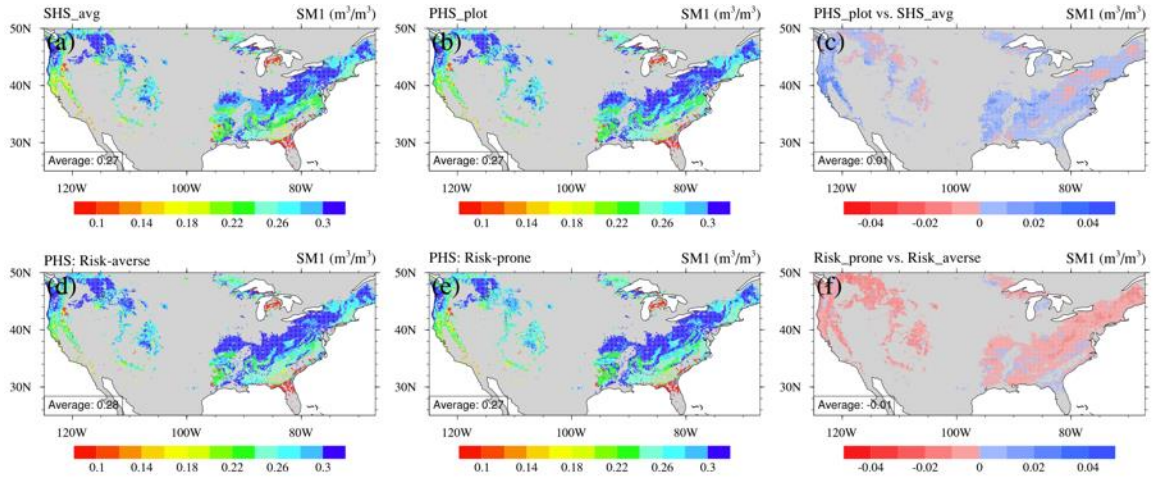

Figure 4.17: Similar to Figure 4.2 but for the 1st layer soil moisture (SM1).

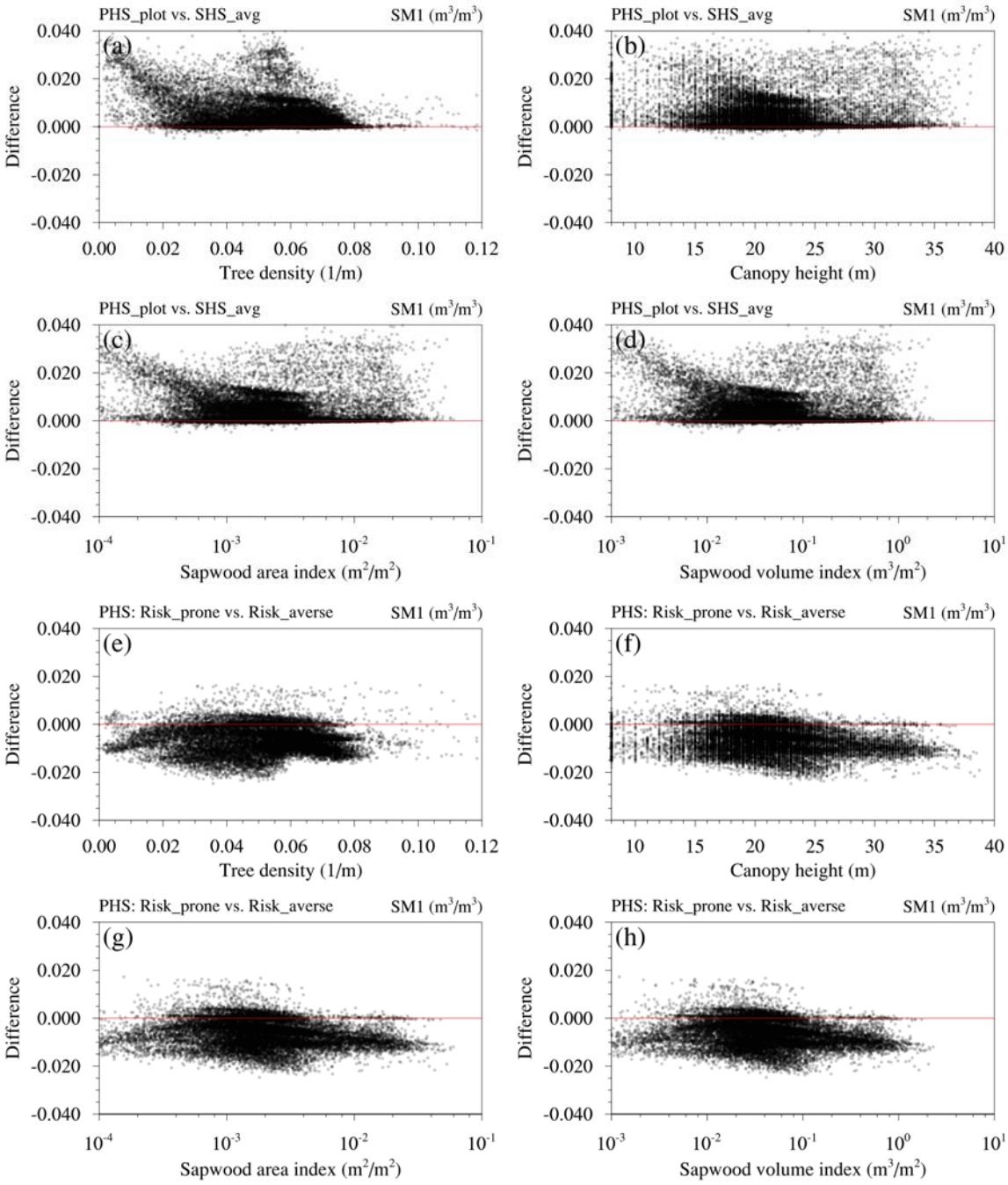

Figure 4.18: Similar to Figure 4.3 but for the 1st layer soil moisture (SM1).

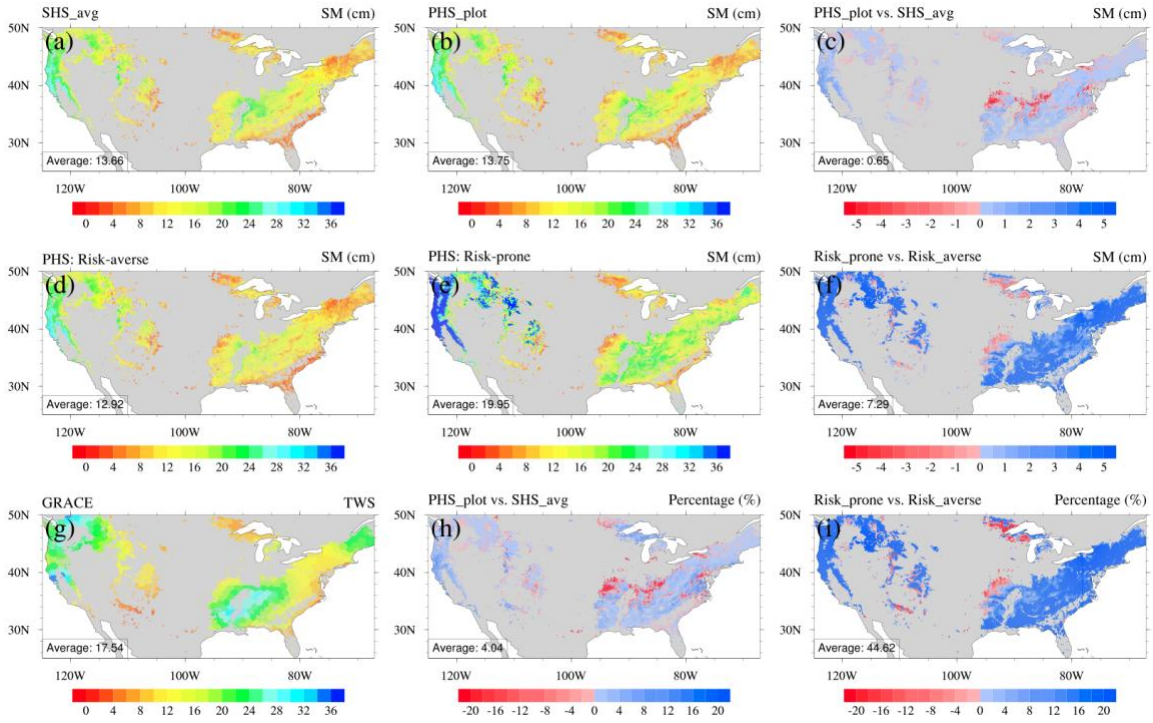

Figure 4.19: Similar to Figure 4.12 but for the soil moisture (SM), the sum of soil water from all four layers.

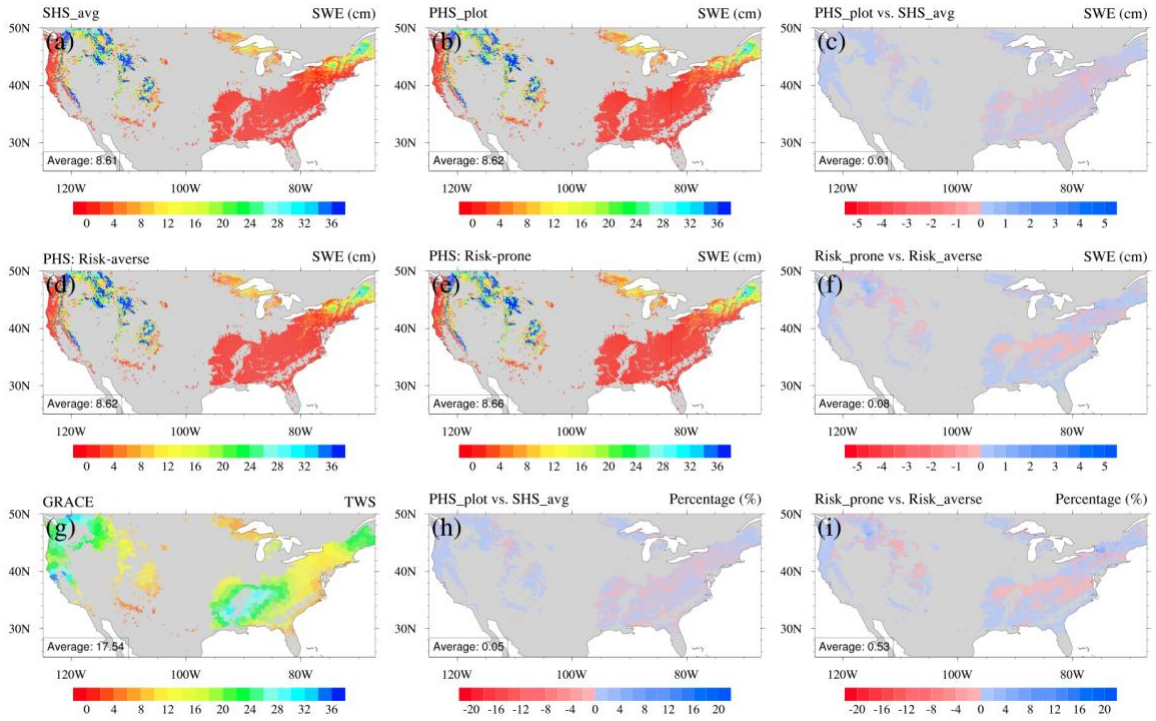

Figure 4.20: Similar to Figure 4.12 but for the snow water equivalent (SWE).

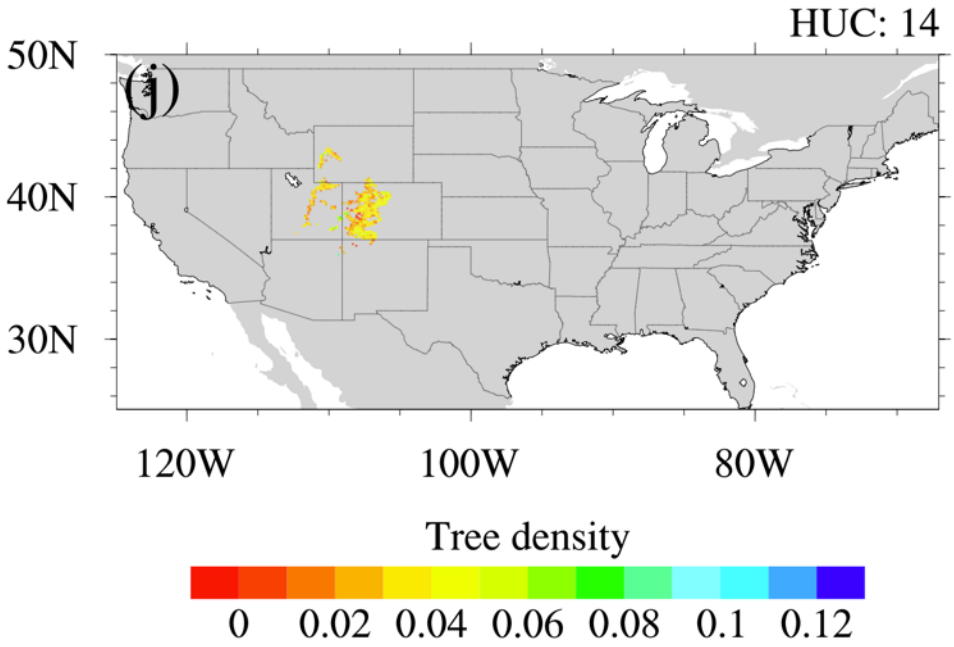

Figure 4.21: Forest regions in the No. 14 of HUC02 watershed (see Figure 4.14) over the central-western US.

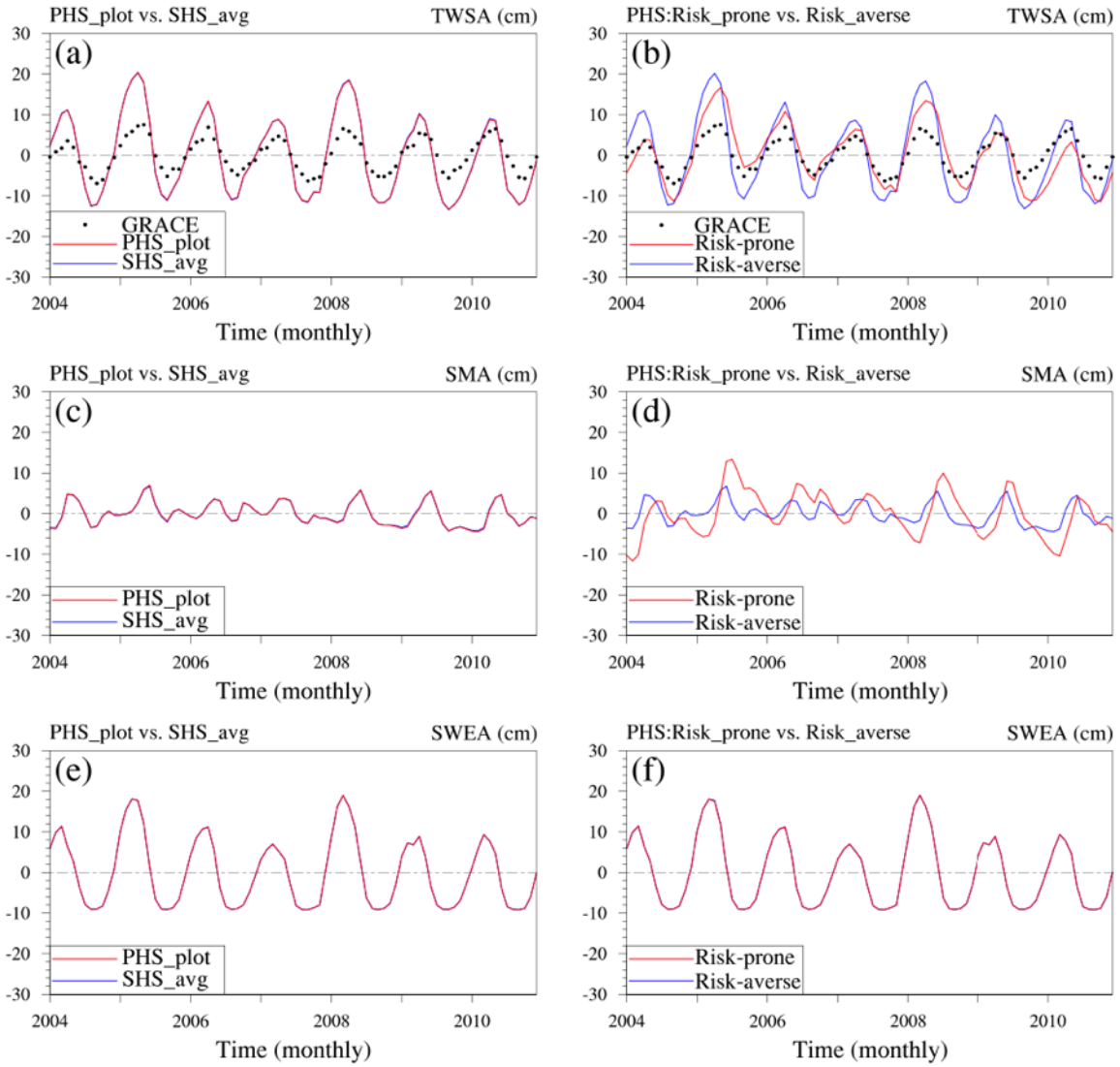

Figure 4.22: Monthly regional averages of TWSA, SMA, SWEA for the PHS_plot vs. SHS_avg experiments (Figures in the left column) and PHS risk-averse vs. PHS risk-prone experiments (Figures in the right column) during 2004–2010 over forest region in the No. 14 of HUC02.

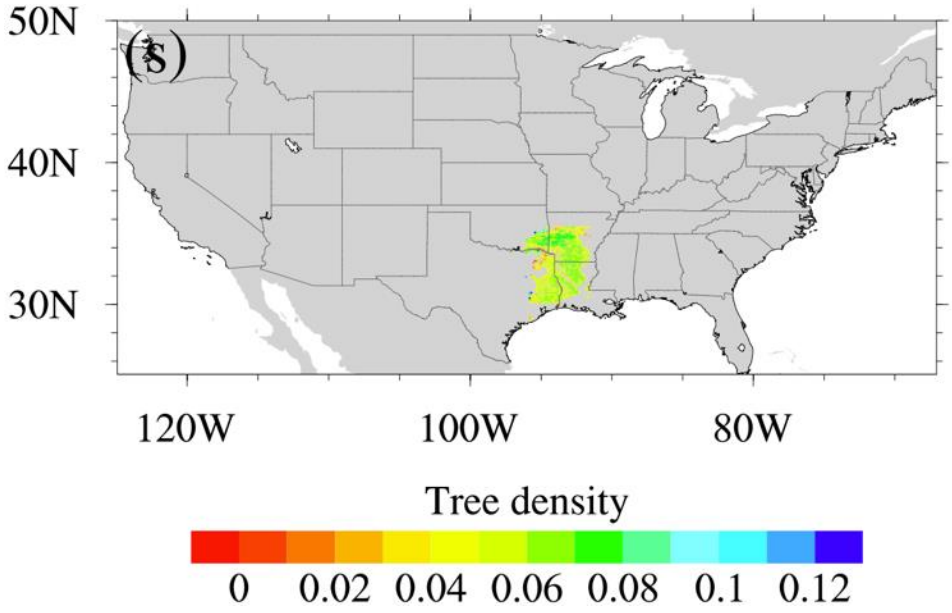

Figure 4.23: Forest regions over Eastern Texas and its adjacent area.

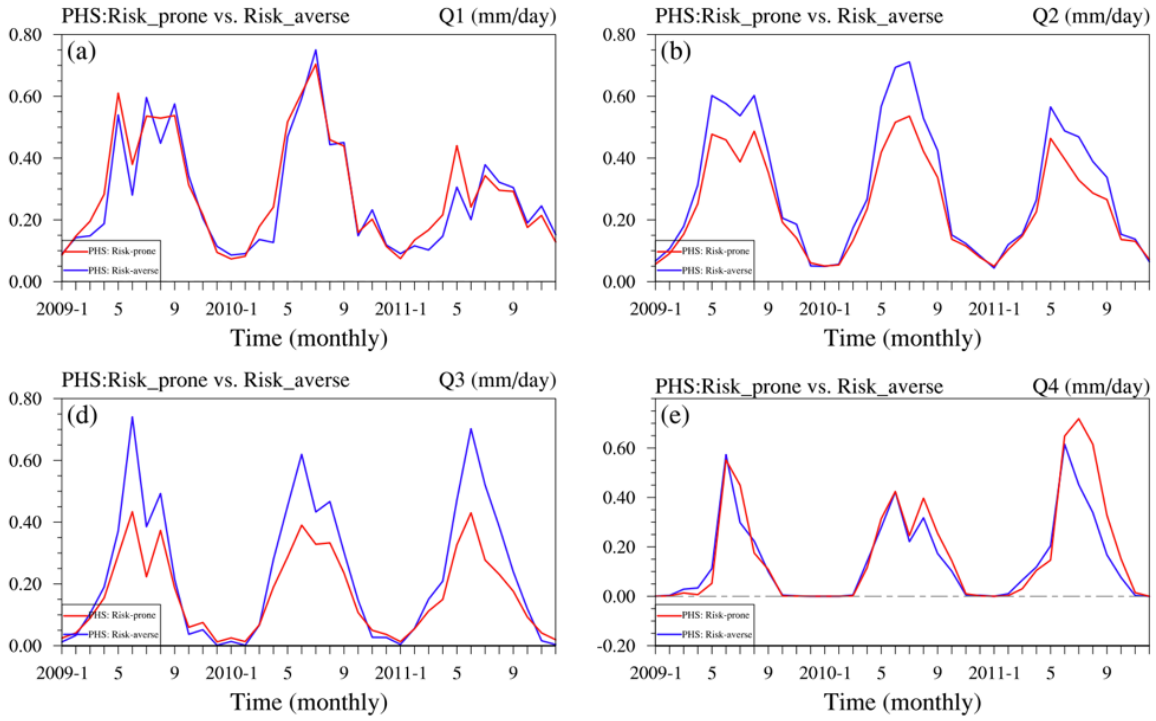

Figure 4.24: Monthly regional averages of root water uptake for PHS risk-averse and PHS risk-prone experiments during 2009–2011 over the eastern Texas forest.

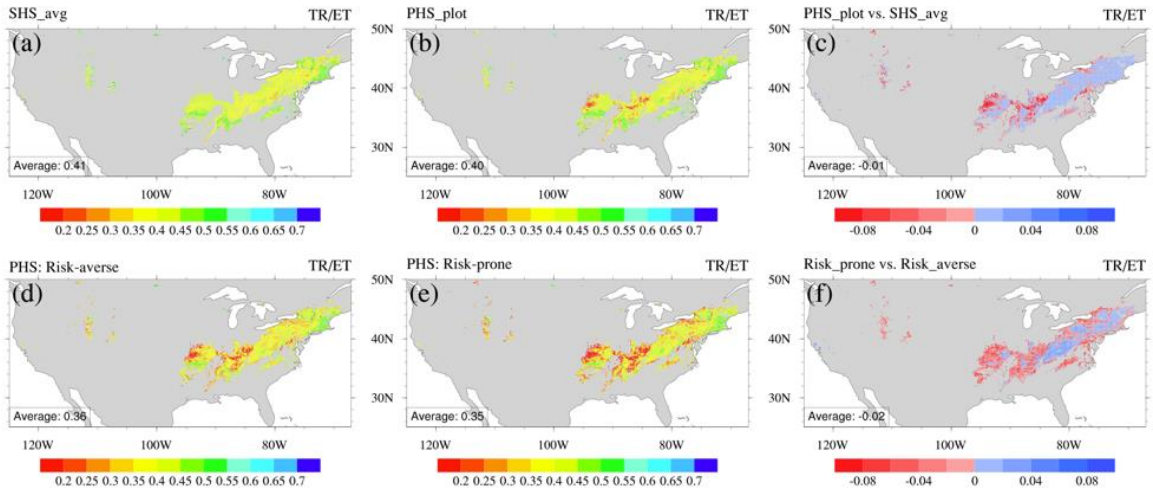

Figure 4.25: Similar to Figure 4.2 but for the TR/ET over DBF regions with all annual data during 1987–2016.

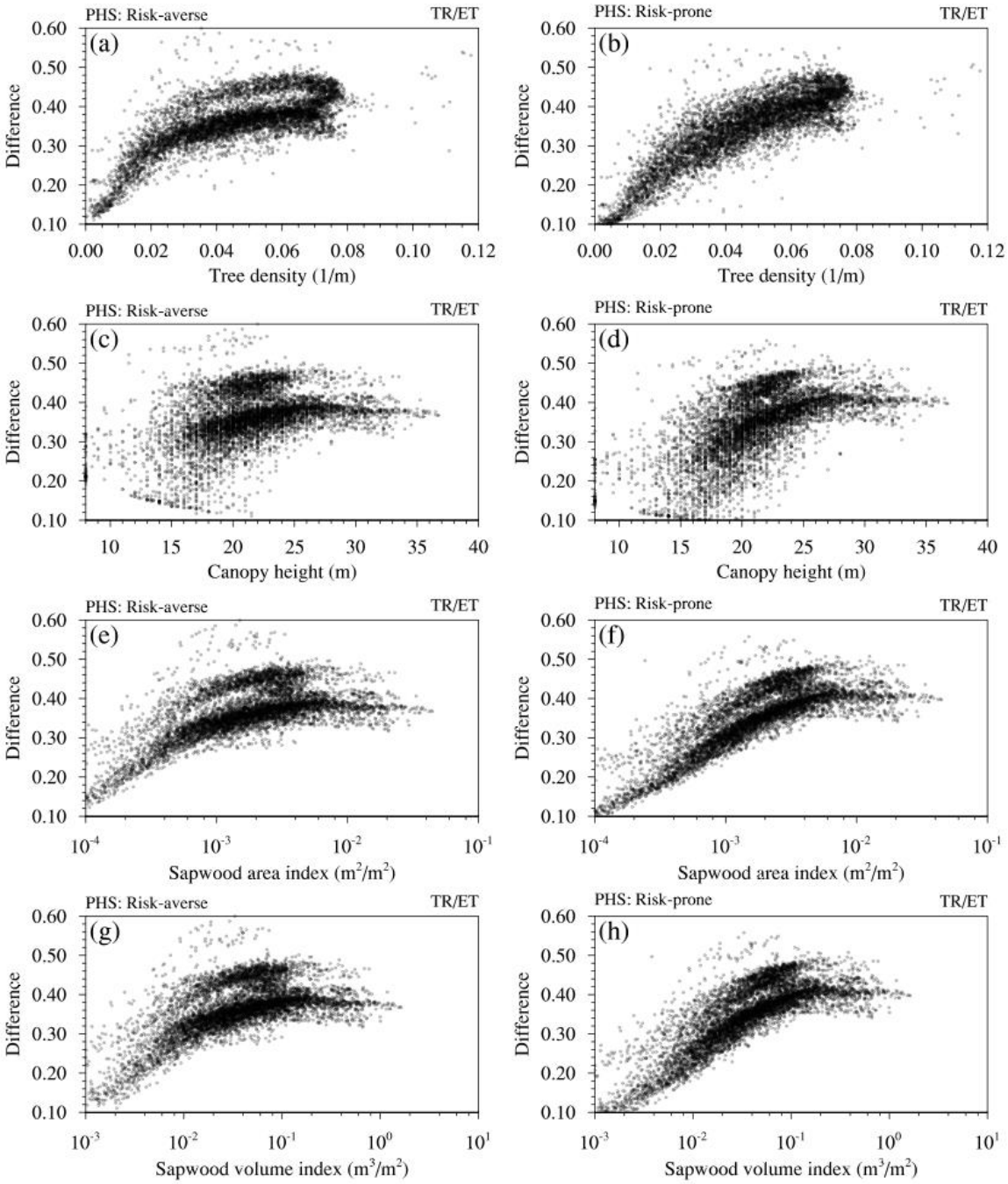

Figure 4.26: The relationships between TR/ET and plant traits for PHS experiments with different plant hydraulic strategies over DBF regions.

Chapter 5: Summary and Future Perspectives

5.1 DISSERTATION SUMMARY

Under climate change, terrestrial ecosystems are likely to face more hydroclimatic stress with decreasing water supply and increasing climatic water demand. Plant hydraulics describes the mechanism of plant water uptake from the soil, water transport to leaves, and water loss through stomata. This dissertation aims to better understand and simulate the role of plant hydraulics in regulating the terrestrial water and carbon cycles by observational data analysis and new model development and application at multi-spatial scales.

Chapter 2 focuses on the impacts of plant hydraulics-related properties on the sensitivity of vegetation interannual variability to hydroclimatic factors (i.e., precipitation and VPD) in North America. Precipitation has positive effects on vegetation for arid ecosystems (aridity index < 0.65; e.g., grassland) and negative effects on humid ecosystems (aridity index ≥ 0.65; e.g., forests). VPD has negative effects on vegetation greenness. Anisohydric plants are more sensitive to VPD than the relatively isohydric plants. Humid anisohydric ecosystems are more sensitive to VPD than precipitation, while arid anisohydric ecosystems are equally sensitive to precipitation and VPD. Given the projected rising VPD under climate change, it is expected that anisohydric plants could suffer more from atmospheric moisture stress. This analysis highlights the important role of plant hydraulics on the coupling strength between vegetation and hydroclimatic factors. Therefore, the implementation of plant hydraulics in Earth system models (ESMs) could better simulate vegetation response and carbon and water cycles, particularly under water stress conditions.

In Chapter 3, I implemented a novel plant hydraulics scheme into the Noah-MP land surface model. Most land surface models use empirical soil hydraulics schemes (SHSs), one of the primary uncertainties sources for carbon and water simulations. Therefore, I presented a novel plant hydraulics scheme (PHS) in Noah-MP (i.e., Noah-MP-PHS), which employs a big-tree rather than big-leaf concept, wherein the whole-plant hydraulic strategy is considered. Noah-MP-PHS was evaluated using plot-level observations from UMBS. Compared with default Noah-MP with SHS, Noah-MP-PHS better represents plant water stress and improves water and carbon simulations, especially during dry soil conditions. Additional improvements include the simulation of the asymmetrical diel cycles of transpiration and gross primary production under low soil moisture conditions, with higher fluxes in the morning than in the afternoon. Noah-MP-PHS can reproduce different transpiration patterns, stem water storage and root water uptake during the dry-down period for two species with contrasting plant hydraulic behaviors, i.e., the "cavitation risk-averse" red maple and the "cavitation risk-prone" red oak. Sensitivity experiments with plant hydraulic capacitance showed that stem water storage enables nocturnal plant water recharge and provides an important buffer to relieve xylem hydraulic stress during dry soil conditions.

In Chapter 4, I extended the plot-level and tree-level PHS experiments to CONUS forest regions. I conducted six experiments, including the three default experiments with SHS and three PHS experiments. PHS_plot, PHS risk-averse, and risk-prone experiments used calibrated PHS parameters from UMBS plot-level, maple tree-level, and oak tree-level simulations. I calculated the spatial sapwood area and volume indexes over CONUS forest regions, which have not yet been used within land surface modeling. I found that plant hydraulic traits affect the TR/ET of PHS experiments. Forests with larger tree density and canopy height, and hence larger sapwood area and volume indexes, tend to have larger

TR/ET. PHS with different hydraulic strategies have a tremendous difference in simulated TWS amplitude, accounting for an overall average of 37.57% of GRACE TWS over CONUS. For the overall CONUS TWSA from 2003–2016, PHS experiments are slightly better consistent with GRACE data than the SHS experiments, due to differences in amplitude and timing of soil moisture anomaly. In the 2011 Texas drought, PHS experiments, especially the risk-prone experiment, better capture the GRACE TWSA than the default SHS experiments. Our study highlights that plant hydraulics, with more realistic representations of plant traits and hydraulic strategies, could provide a vital link for reconciling observations and models of terrestrial water cycles.

5.2 CAVEATS AND FUTURE WORK

Further research is needed for Chapter 2. We only used one set of datasets, including one type of vegetation productivity (i.e., NDVI) and one set of forcing (i.e., NLDAS precipitation, VPD, TMP). Future study should include more parallel datasets, e.g., FLUXCOM GPP (Jung et al., 2020) and CRU TS (Climatic Research Unit gridded Time Series, Harris et al., 2020) data, to make conclusions more robust. Considering the increasing VPD in recent and potential future climate (Yuan et al., 2019), further analysis should be done to quantify the effects of VPD globally on vegetation, especially for the anisohydric ecosystems (Konings et al., 2017).

Further development of plant hydraulics scheme is warranted. The plant hydraulics scheme implemented in Noah-MP is based on a whole-plant hydraulic strategy concept, considering the hydraulic traits at leaves, stem (xylem), and roots. To balance the trade-off between model complexity and efficiency, some plant hydraulic mechanisms are not considered in this PHS. PHS is unable to capture well the gradual recharge of stem water during the rewetting period, missing the time lag associated with vessel refilling after

drought (Mrad et al., 2018). PHS does not explicitly invoke (Fatichi et al., 2016). Besides, hormone abscisic acid (ABA), dynamic root, and rhizosphere process have shown their importance for given ecosystems or environments (Tuzet et al., 2003; Christoffersen et al., 2016; Wang et al., 2018b). Therefore, the advancement of the PHS framework should further include these mechanisms.

Further experiments should be conducted for CONUS experiments. Our current simulations do not consider the groundwater process, which could induce the uncertainties of simulated TWS. Cai et al. (2014b) found that groundwater anomaly contributes about one-third of the correlation coefficient and RMSE on TWS anomaly average over the CONUS. Besides, the variation of surface water storage (e.g., reservoirs and lakes) could also dominate the TWS anomaly in given circumstances (Scanlon et al., 2015). Therefore, future experiments should include all these processes to represent TWS anomaly better.

The representation of plant hydraulic strategies on large spatial scale is required for large spatial scale modeling. In most LSMs, plants are grouped into broad plant functional types (PFTs). The PFT framework does not explicitly consider plant hydraulic strategies. Therefore, it is not an ideal way to incorporate plant hydraulic strategies into current PFT categories. Moving beyond the PFT paradigm, a promising solution is a fully trait-based approach instead of classifying plants into limited categories (Van Bodegom et al., 2014; Yang et al., 2015; Laughlin and Laughlin, 2013). The trait-based approach has shown encouraging improvements in model simulations (Verheijen et al., 2013; Scheiter et al., 2013; Van Bodegom et al., 2014). Together with the emerging multi-source observations, including in-situ (e.g., the TRY database, Kattge et al., 2011) and remote sensing (e.g., vegetation optical depth, Konings et al., 2019), and new technologies like machine learning (e.g., Verrelst et al., 2012; Moreno-Martínez et al., 2018), the trait-based approach provides

a promising future for the representation plant hydraulic and other functional traits in large spatial scale models.

Further applications of Noah-MP-PHS can be made. (1) The plant hydraulics scheme shows better performance of water and carbon simulations during dry soil periods. It is quite straightforward to apply Noah-MP-PHS for drought monitoring and forecasting. (2) Noah-MP-PHS simulated the plant water potential and water storage during the plant hydraulics process. Therefore, another exciting research is to assimilate the remote sensing data (e.g., vegetation optical depth) to improve model performance (Kumar et al., 2020). (3) Conducting further coupling experiments (e.g., within Weather Research and Forecasting Model) to understand the role plant hydraulics on weather predictions of precipitation and temperature.

Bibliography

Abatzoglou, J. T., & Williams A. P. (2016). Impact of anthropogenic climate change on wildfire across western US forests. Proceedings of the National Academy of Sciences, 113(42), 11770-11775. https://doi.org/10.1073/pnas.1607171113

Ahlstrom, A., Raupach, M. R., Schurgers, G., et al. (2015). The dominant role of semi-arid ecosystems in the trend and variability of the land CO2 sink. Science, 348(6237), 895–899. https://doi.org/10.1126/science.aaa1668

Allen, C. D., Macalady, A. K., Chenchouni, H., et al. (2010). A global overview of drought and heat-induced tree mortality reveals emerging climate change risks for forests. Forest ecology and management, 259(4), 660-684. HTTP://doi.ORG/10.1016/j.foreco.2009.09.001.

Allen, M.F. (2009). Water Relations in the Mycorrhizosphere. In: Lüttge U., Beyschlag W., Büdel B., Francis D. (eds) Progress in Botany. Progress in Botany, vol 70. Springer, Berlin, Heidelberg.

Anderegg, W. R., Berry, J. A., Smith, D. D., et al. (2012). The roles of hydraulic and carbon stress in a widespread climate-induced forest die-off. Proceedings of the National Academy of Sciences, 109(1), 233-237. http://doi.org/10.1073/pnas.1107891109.

Anderegg, W. R. (2015). Spatial and temporal variation in plant hydraulic traits and their relevance for climate change impacts on vegetation. New Phytologist, 205(3), 1008-1014. https://doi.org/10.1111/nph.12907

Anderegg, W. R. L. et al. (2017), Plant water potential improves prediction of empirical stomatal models, edited by R. Aroca, PLoS ONE, 12(10), e0185481, doi:10.1371/journal.pone.0185481.

Anderegg, W. R. L. et al. (2018). Hydraulic diversity of forests regulates ecosystem resilience during drought, Nature, 320, 1. http://doi.org/10.1038/s41586-018-0539-7

Anderegg, W. R. L., and M. D. Venturas. (2020), Plant hydraulics play a critical role in Earth system fluxes, New Phytologist, 226(6), 1535–1538. https://doi.org/10.1111/nph.16548.

Baldocchi, D., H. Chu, and M. Reichstein. (2018). Inter-annual variability of net and gross ecosystem carbon fluxes: A review, Agricultural and Forest Meteorology, 249, 520–533. https://doi.org/10.1016/j.agrformet.2017.05.015

Bittner, S., Janott, M., Ritter, D., Köcher, P., Beese, F., & Priesack, E. (2012). Functional–structural water flow model reveals differences between diffuse-and ring-porous tree species. Agricultural and forest meteorology, 158, 80-89. https://doi.org/10.1016/j.agrformet.2012.02.005

Blackman, C. J. (2018). Leaf turgor loss as a predictor of plant drought response strategies. Tree physiology, 38(5), 655-657. https://doi.org/10.1093/treephys/tpy047

Bohrer, G., Mourad, H., Laursen, T. A., et al. (2005). Finite element tree crown hydrodynamics model (FETCH) using porous media flow within branching elements: A new representation of tree hydrodynamics. Water Resources Research, 41(11). https://doi.org/10.1029/2005WR004181

Bonan, G. B. (2008), Forests and Climate Change: Forcings, Feedbacks, and the Climate Benefits of Forests, Science, 320(5882), 1444–1449. http://doi.org/10.1126/science.1155121.

Bonan, G. B., & Doney, S. C. (2018). Climate, ecosystems, and planetary futures: The challenge to predict life in Earth system models. Science, 359(6375), eaam8328. https://doi.org/10.1126/science.aam8328

Bousquet, P., Peylin, P., Ciais, P., et al. (2000). Regional changes in carbon dioxide fluxes of land and oceans since 1980. Science, 290(5495), 1342-1346. https://doi.org/10.1126/science.290.5495.1342

Bovard, B. D., Curtis, P. S., Vogel, C. S., Su, H. B., & Schmid, H. P. (2005). Environmental controls on sap flow in a northern hardwood forest. Tree physiology, 25(1), 31-38. https://doi.org/10.1093/treephys/25.1.31

Bréda, N., Granier, A., Barataud, F. et al. (1995). Soil water dynamics in an oak stand. Plant Soil 172, 17–27. https://doi.org/10.1007/BF00020856

Brodribb T. J. (2009). Xylem hydraulic physiology: the functional backbone of terrestrial plant productivity. Plant Science, 177(4), 245-251. https://doi.org/10.1016/j.plantsci.2009.06.001

Brodribb, T. J., Powers, J., Cochard, H., & Choat, B. (2020). Hanging by a thread? Forests and drought. Science, 368(6488), 261–266. http://doi.org/10.1126/science.aat7631

Buckley, T. N. (2005). The control of stomata by water balance, New Phytologist, 168(2), 275–292. http://doi.org/10.1111/j.1469-8137.2005.01543.x

Cai, X., Yang, Z. L., David, C. H., Niu, G. Y., & Rodell, M. (2014a). Hydrological evaluation of the Noah-MP land surface model for the Mississippi River Basin. Journal of Geophysical Research: Atmospheres, 119(1), 23–38. http://doi.org/10.1002/2013JD020792

Cai, X., Yang, Z. L., Xia, Y., Huang, M., Wei, H., Leung, L. R., & Ek, M. B. (2014b). Assessment of simulated water balance from Noah, Noah-MP, CLM, and VIC over CONUS using the NLDAS test bed. Journal of Geophysical Research: Atmospheres, 119(24), 13,751–13,770. http://doi.org/10.1002/2014JD022113

Calvet, J.C., Noilhan, J., Roujean, J.L., et al. (1998). An interactive vegetation SVAT model tested against data from six contrasting sites. Agricultural and Forest Meteorology, 92(2), pp.73-95. https://doi.org/10.1016/S0168-1923(98)00091-4

Canadell, J., Jackson, R. B., Ehleringer, J. B., Mooney, H. A., Sala, O. E., & Schulze, E. D. (1996). Maximum rooting depth of vegetation types at the global scale. Oecologia, 108(4), 583-595. https://doi.org/10.1007/BF00329030

Carrasco, L. O., Bucci, S. J., Francescantonio, D. D., et al. (2014). Water storage dynamics in the main stem of subtropical tree species differing in wood density, growth rate and life history traits. Tree Physiol. 35, 354–365. http:/doi.org/10.1093/treephys/tpu087

Chen, F., & Dudhia, J. (2001). Coupling an advanced land surface–hydrology model with the Penn State–NCAR MM5 modeling system. Part I: Model implementation and sensitivity. Monthly weather review, 129(4), 569-585. https://doi.org/10.1175/1520-0493(2001)129<0569:CAALSH>2.0.CO;2

Choat, B., Jansen, S., Brodribb, T. J., et al. (2012). Global convergence in the vulnerability of forests to drought. Nature, 491, 752–756. http://doi.org/10.1038/nature11688

Christoffersen, B.O., Gloor, M., Fauset, S., Fyllas, N.M., et al. (2016). Linking hydraulic traits to tropical forest function in a size-structured and trait-driven model (TFS v. 1-Hydro). http://doi.org/10.5194/gmd-9-4227-2016

Chuang, Y. L., Oren, R., Bertozzi, A. L., Phillips, N., & Katul, G. G. (2006). The porous media model for the hydraulic system of a conifer tree: linking sap flux data to transpiration rate. Ecological Modelling, 191(3-4), 447-468. http://doi.org/10.1016/j.ecolmodel.2005.03.027

Clapp, R. B., & Hornberger, G. M. (1978). Empirical equations for some soil hydraulic properties. Water resources research, 14(4), 601-604. https://doi.org/10.1029/WR014i004p00601

Cook, B. I., Ault, T. R., & Smerdon, J. E. (2015). Unprecedented 21st century drought risk in the American Southwest and Central Plains. Science Advances, 1(1), e1400082. https://doi.org/10.1126/sciadv.1400082

Cosgrove, B., Gochis, D., Clark, E.P., et al. (2016). December. An Overview of the National Weather Service National Water Model. In AGU Fall Meeting Abstracts

Cox, P. M., Pearson, D., Booth, B. B., et al. (2013). Sensitivity of tropical carbon to climate change constrained by carbon dioxide variability. Nature, 494(7437), 341-344. https://doi.org/10.1038/nature11882

Crowther, T., Glick, H., Covey, K. et al. 2015. Mapping tree density at a global scale. Nature 525, 201–205. https://doi.org/10.1038/nature14967

Dai, A. (2013). Increasing drought under global warming in observations and models, Nature Climate Change, 3(1), 52–58. http://doi.org/10.1038/nclimate1633

Daley, M. J., & Phillips, N. G. (2006). Interspecific variation in nighttime transpiration and stomatal conductance in a mixed New England deciduous forest. Tree physiology, 26(4), 411-419. https://doi.org/10.1093/treephys/26.4.411

Deans, R. M., Brodribb, T. J., & McAdam, S. A. (2017). An integrated hydraulic-hormonal model of conifer stomata predicts water stress dynamics. Plant physiology, 174(2), 478-486. https://doi.org/10.1104/pp.17.00150

Denmead O.T. & Shaw R.H. (1962). Availability of soil water to plants as affected by soil moisture content and meteorological conditions. Agronomy Journal 54, 385–390. https://doi.org/10.2134/agronj1962.00021962005400050005x

Dirmeyer, P. A., Gao, X., Zhao, M., et al. (2006). GSWP-2: Multimodel Analysis and Implications for Our Perception of the Land Surface, Bull. Amer. Meteor. Soc., 87(10), 1381–1398. http://doi.org/10.1175/BAMS-87-10-1381

Dixon, H. H., & Joly, J. (1895). On the ascent of sap. Philosophical Transactions of the Royal Society of London. B, 186, 563-576.

Egea, G., A. Verhoef, and P. L. Vidale, 2011. Towards an improved and more flexible representation of water stress in coupled photosynthesis–stomatal conductance models, Agricultural and Forest Meteorology, 151(10), 1370–1384. http://doi.org/10.1016/j.agrformet.2011.05.019.

Eller, C. B., Rowland, L., Mencuccini, M., et al. (2020). Stomatal optimisation based on xylem hydraulics (SOX) improves land surface model simulation of vegetation responses to climate. New Phytologist. https://doi.org/10.1111/nph.16419

Eller, C. B., Rowland, L., Oliveira, R. S., et al. (2018). Modelling tropical forest responses to drought and El Niño with a stomatal optimization model based on xylem hydraulics. Philosophical Transactions of the Royal Society B: Biological Sciences, 373(1760), 20170315. http://doi.org/10.1098/rstb.2017.0315

Fan, Y., Miguez-Macho, G., Jobbágy, E. G., Jackson, R. B., & Otero-Casal, C. (2017). Hydrologic regulation of plant rooting depth. Proceedings of the National Academy of Sciences, 114(40), 10572-10577. https://doi.org/10.1073/pnas.1712381114

Fang, W., Lu, N., Zhang, Y., Jiao, L., & Fu, B. (2018). Responses of nighttime sap flow to atmospheric and soil dryness and its potential roles for shrubs on the Loess Plateau of China. Journal of Plant Ecology, 11(5), 717-729. https://doi.org/10.1093/jpe/rtx042

Fatichi, S., Pappas, C., & Ivanov, V. Y. (2016). Modeling plant–water interactions: an ecohydrological overview from the cell to the global scale. Wiley Interdisciplinary Reviews: Water, 3(3), 327-368. https://doi.org/10.1002/wat2.1125

Feng, X., Ackerly, D. D., Dawson, T. E., et al. (2019). Beyond isohydricity: The role of environmental variability in determining plant drought responses. Plant, cell & environment, 42(4), 1104-1111. https://doi.org/10.1111/pce.13486

Fisher, R. A., Williams, M., Do Vale, R. L., Da Costa, A. L., & Meir, P. (2006). Evidence from Amazonian forests is consistent with isohydric control of leaf water potential.

Plant, Cell & Environment, 29(2), 151–165. https://doi.org/10.1111/j.1365-3040.2005.01407.x

Friedl, M. A., Sulla-Menashe, D., Tan, B., et al. (2010). MODIS Collection 5 global land cover: Algorithm refinements and characterization of new datasets. Remote sensing of Environment, 114(1), 168-182. https://doi.org/10.1016/j.rse.2009.08.016

Friedl, M., & Sulla-Menashe, D. (2015). MCD12C1 MODIS/Terra+Aqua Land Cover Type Yearly L3 Global 0.05Deg CMG V006 [Data set]. NASA EOSDIS Land Processes DAAC. Accessed 2020-07-04 from https://doi.org/10.5067/MODIS/MCD12C1.006

Fyllas, N. M., Gloor, E., Mercado, L. M., Sitch, S., et al. (2014). Analysing Amazonian forest productivity using a new individual and trait-based model (TFS v. 1). Geoscientific Model Development, 7, 1251–1269. https://doi.org/10.5194/gmd-7-1251-2014

Garrity, S. R., K. Meyer, K. D. Maurer, B. Hardiman, and G. Bohrer (2011), Estimating plot-level tree structure in a deciduous forest by combining allometric equations, spatial wavelet analysis and airborne LiDAR, Remote Sensing Letters, 3(5), 443–451. https://doi.org/10.1080/01431161.2011.618814.

Gentine, P., Guérin, M., Uriarte, M., McDowell, N. G., & Pockman, W. T. (2016). An allometry-based model of the survival strategies of hydraulic failure and carbon starvation. Ecohydrology, 9(3), 529-546. https://doi.org/10.1002/eco.1654

Giardina, F., A. G. Konings, D. Kennedy, S. H. Alemohammad, R. S. Oliveira, M. Uriarte, and P. Gentine. (2018). Tall Amazonian forests are less sensitive to precipitation variability, Nature Geosci, 11(6), 405–409. https://doi.org/10.1038/s41561-018-0133-5.

Gentine, P., Green, J. K., Guérin, M., et al. (2019). Coupling between the terrestrial carbon and water cycles—a review. Environmental Research Letters, 14(8), 083003. https://doi.org/10.1088/1748-9326/ab22d6

Goldstein, G., Andrade, J. L., Meinzer, F. C., et al. (1998). Stem water storage and diurnal patterns of water use in tropical forest canopy trees. Plant, Cell & Environment, 21(4), 397-406. https://doi.org/10.1046/j.1365-3040.1998.00273.x

Good, S. P., Noone, D., & Bowen, G. (2015). Hydrologic connectivity constrains partitioning of global terrestrial water fluxes. Science, 349(6244), 175-177. http://doi.org/10.1126/science.aaa5931

Grant, R.F., Wall, G.W., Kimball, B.A., et al. (1999). Crop water relations under different CO2 and irrigation: testing of ecosys with the free air CO2 enrichment (FACE) experiment. Agricultural and Forest Meteorology, 95(1), pp.27-51. https://doi.org/10.1016/S0168-1923(99)00017-9

Green, J. K., Seneviratne, S. I., Berg, A. M., et al. (2019). Large influence of soil moisture on long-term terrestrial carbon uptake. Nature, 565(7740), 476-479. https://doi.org/10.1038/s41586-018-0848-x

Grossiord, C., T. N. Buckley, L. A. Cernusak, K. A. Novick, B. Poulter, R. T. W. Siegwolf, J. S. Sperry, and N. G. McDowell. (2020), Plant responses to rising vapor pressure deficit, New Phytologist, 59, 531632. https://doi.org/10.1111/nph.16485

Gu, C., Ma, J., Zhu, G., Yang, H., Zhang, K., Wang, Y., & Gu, C. (2018). Partitioning evapotranspiration using an optimized satellite-based ET model across biomes. Agricultural and Forest Meteorology, 259, 355–363. http://doi.org/10.1016/j.agrformet.2018.05.023

Gupta, H. V., Kling, H., Yilmaz, K. K., & Martinez, G. F. (2009). Decomposition of the mean squared error and NSE performance criteria: Implications for improving hydrological modelling. Journal of Hydrology, 377(1-2), 80–91. https://doi.org/10.1016/j.jhydrol.2009.08.003

Gutschick, V. P., & Simonneau, T. (2002). Modelling stomatal conductanceof field-grown sunflower under varying soil water content and leafenvironment: comparison of three models of stomatal response toleaf environment and coupling with an abscisic acid-based modelof stomatal response to soil drying. Plant, Cell & Environment, 25(11), 1423-1434. https://doi.org/10.1046/j.1365-3040.2002.00937.x

Hacke, U. G., & Sperry, J. S. (2003). Limits to xylem refilling under negative pressure in Laurus nobilis and Acer negundo. Plant, Cell & Environment, 26(2), 303-311. https://doi.org/10.1046/j.1365-3040.2003.00962.x

Harris, I., Osborn, T.J., Jones, P., et al. (2020). Version 4 of the CRU TS monthly high-resolution gridded multivariate climate dataset. Scientific Data, 7(1), 1-18. https://doi.org/10.1038/s41597-020-0453-3

He, L., Ivanov, V. Y., Bohrer, G., et al. (2013). Temporal dynamics of soil moisture in a northern temperate mixed successional forest after a prescribed intermediate disturbance. Agricultural and forest meteorology, 180, 22-33. https://doi.org/10.1016/j.agrformet.2013.04.014

Hickler, T., Prentice, I. C., Smith, B., Sykes, M. T., & Zaehle, S. (2006). Implementing plant hydraulic architecture within the LPJ Dynamic Global Vegetation Model. Global Ecology and Biogeography, 15(6), 567-577. https://doi.org/10.1111/j.1466-8238.2006.00254.x

Huang, C. W., Domec, J. C., Ward, E. J., et al. (2017). The effect of plant water storage on water fluxes within the coupled soil–plant system. New Phytologist, 213(3), 1093-1106. https://doi.org/10.1111/nph.14273

Huang, M., Piao, S., Ciais, P., et al. (2019). Air temperature optima of vegetation productivity across global biomes. Nature ecology & evolution, 3(5), 772-779. https://doi.org/10.1038/s41559-019-0838-x

Hunt Jr, E. R., Running, S. W., & Federer, C. A. (1991). Extrapolating plant water flow resistances and capacitances to regional scales. Agricultural and Forest Meteorology, 54(2-4), 169-195. https://doi.org/10.1016/0168-1923(91)90005-B

IPCC 2013 Climate Change 2013: The Physical Science Basis. Working Group I Contribution to the IPCC 5th Assessment Report (Final Draft. Co-Chairs of Working Group I)

Janott, M., Gayler, S., Gessler, A. et al. (2011). A one-dimensional model of water flow in soil-plant systems based on plant architecture. Plant Soil 341, 233–256. https://doi.org/10.1007/s11104-010-0639-0

Jasechko, S., Sharp, Z., Gibson, J. et al. Terrestrial water fluxes dominated by transpiration. Nature 496, 347–350 (2013). https://doi.org/10.1038/nature11983

Jung, M., Reichstein, M., Schwalm, C. R., Huntingford, C., Sitch, S., Ahlström, A., et al. (2017). Compensatory water effects link yearly global land CO2 sink changes to temperature. Nature, 541(7638), 516–520. http://doi.org/10.1038/nature20780

Jung, M., Schwalm, C., Migliavacca, M., Walther, S., Camps-Valls, G., Koirala, S., et al. (2020). Scaling carbon fluxes from eddy covariance sites to globe: synthesis and evaluation of the FLUXCOM approach. Biogeosciences, 17(5), 1343–1365. http://hdl.handle.net/21.11116/0000-0004-CDE4-4

Kattge, J., Diaz, S., Lavorel, S., et al. (2011). TRY–a global database of plant traits. Global change biology, 17(9), 2905-2935. https://dx.doi.org/10.1111%2Fj.1365-2486.2011.02451.x

Katul, G., Leuning, R., & Oren, R. (2003). Relationship between plant hydraulic and biochemical properties derived from a steady-state coupled water and carbon transport model. Plant, Cell & Environment, 26(3), 339-350. https://doi.org/10.1046/j.1365-3040.2003.00965.x

Keeling, C. D., Piper, S. C. & Heimann, M. in Aspects of Climate Variability in the Pacific and Western Americas (ed. Peterson, D. H.) 305–363 (Washington, D.C., 1989).

Kennedy, D. (2020). Implementing plant hydraulics in an Earth System Model and the implications for the global carbon and water cycles. Doctoral dissertation, Columbia University. https://doi.org/10.7916/d8-9cfn-nc45

Kennedy, D., Swenson, S., Oleson, K. W., Lawrence, D. M., et al. (2019). Implementing plant hydraulics in the community land model, version 5. Journal of Advances in Modeling Earth Systems, 11(2), 485-513. http://doi.org/10.1029/2018MS001500

Kindermann, J., Wurth, G., Kohlmaier, G. H., et al. (1996). Interannual variation of carbon exchange fluxes in terrestrial ecosystems. Global Biogeochemical Cycles, 10(4), 737-755. https://doi.org/10.1029/96GB02349

Kling, H., Fuchs, M., & Paulin, M. (2012). Runoff conditions in the upper Danube basin under an ensemble of climate change scenarios. Journal of Hydrology, 424-425, 264–277. https://doi.org/10.1016/j.jhydrol.2012.01.011

Konings, A. G., Williams, A. P., & Gentine, P. (2017a). Sensitivity of grassland productivity to aridity controlled by stomatal and xylem regulation. Nature Geoscience, 10(4), 284-288. https://doi.org/10.1038/ngeo2903

Konings, A. G. & Gentine, P. (2017b). Global variations in ecosystem-scale isohydricity. Global chang biology, 23(2), 891-905. https://doi.org/10.1111/gcb.13389

Konings, A. G., Rao, K., & Steele-Dunne, S. C. (2019). Macro to micro: microwave remote sensing of plant water content for physiology and ecology. New Phytologist, 223(3), 1166-1172. https://doi.org/10.1111/nph.15808

Kottek, M., Grieser, J., Beck, C., et al. (2006). World map of the Köppen-Geiger climate classification updated. Meteorologische Zeitschrift, 15(3), 259-263. https://doi.org/10.1127/0941-2948/2006/0130

Kumar, S. V., Peters-Lidard, C. D., Tian, Y., et al. (2006). Land information system: An interoperable framework for high resolution land surface modeling. Environmental modelling & software, 21(10), 1402-1415. http://doi.org/10.1016/j.envsoft.2005.07.004

Kumar, S. V., Holmes, T. R., Bindlish, R., Jeu, R. de, & Peters-Lidard, C. (2020). Assimilation of vegetation optical depth retrievals from passive microwave radiometry. Hydrology and Earth System Sciences, 24(7), 3431–3450. http://doi.org/10.5194/hess-24-3431-2020

Laughlin, D. C., & Laughlin, D. E. (2013). Advances in modeling trait-based plant community assembly. Trends in Plant Science, 18(10), 584-593. https://doi.org/10.1016/j.tplants.2013.04.012

Le Quéré, C., Andres, R. J., Boden, T., et al. (2013). The global carbon budget 1959–2011. Earth System science data, 5, 165-185. http://hdl.handle.net/11858/00-001M-0000-0013-780C-3

Lehnebach, R., Beyer, R., Letort, V., & Heuret, P. (2018). The pipe model theory half a century on: a review. Annals of botany, 121(5), 773-795. http://doi.org/10.1093/aob/mcx194

Li, L.C., Yang, Z-L, Matheny, A., et al. (2020). Development of Plant Hydraulics in the Noah-MP Land Surface Model. Submitted to Journal of Advances in Modeling Earth Systems.

Li, Y., Guan, K., Gentine, P., et al. (2017). Estimating Global Ecosystem Isohydry/Anisohydry Using Active and Passive Microwave Satellite Data. Journal of Geophysical Research: Biogeosciences, 122(12), 3306-3321. https://doi.org/10.1002/2017JG003958

Liang, J., Yang, Z., & Lin, P. (2019). Systematic Hydrological Evaluation of the Noah-MP Land Surface Model over China. Advances in Atmospheric Sciences, 36(11), 1171-1187. https://doi.org/10.1007/s00376-019-9016-y

Liu, Y., M. Kumar, G. G. Katul, X. Feng, and A. G. Konings. (2020). Plant hydraulics accentuates the effect of atmospheric moisture stress on transpiration, Nature Climate Change, 313, 1–5. http://doi.org/10.1038/s41558-020-0781-5.

Luo, X., Chen, J. M., Liu, J., et al. (2018). Comparison of big-leaf, two-big-leaf, and two-leaf upscaling schemes for evapotranspiration estimation using coupled carbon-water modeling. Journal of Geophysical Research: Biogeosciences, 123(1), 207-225. https://doi.org/10.1002/2017JG003978

Luo, X., Liang, X., & McCarthy, H. R. (2013). VIC+ for water-limited conditions: A study of biological and hydrological processes and their interactions in soil-plant-atmosphere continuum. Water Resources Research, 49(11), 7711-7732. http://doi.org/10.1002/2012WR012851

Luo, X., Liang, X., & Lin, J. S. (2016). Plant transpiration and groundwater dynamics in water-limited climates: Impacts of hydraulic redistribution. Water Resources Research, 52(6), 4416-4437. https://doi.org/10.1002/2015WR017316

Mackay, D. S., Roberts, D. E., Ewers, B. E., et al. (2015). Interdependence of chronic hydraulic dysfunction and canopy processes can improve integrated models of tree response to drought. Water Resources Research, 51(8), 6156-6176. https://doi.org/10.1002/2015WR017244

Maherali, H., Pockman, W. T., & Jackson, R. B. (2004). Adaptive variation in the vulnerability of woody plants to xylem cavitation. Ecology, 85(8), 2184-2199. https://doi.org/10.1890/02-0538

Maherali, H., Moura, C. F., Caldeira, M. C., et al. (2006). Functional coordination between leaf gas exchange and vulnerability to xylem cavitation in temperate forest trees. Plant, Cell & Environment, 29(4), 571-583. https://doi.org/10.1111/j.1365-3040.2005.01433.x

Manzoni, S. (2014). Integrating plant hydraulics and gas exchange along the drought-response trait spectrum. Tree physiology, 34(10), 1031-1034. https://doi.org/10.1093/treephys/tpu088

Martens, B., Miralles, D. G., Lievens, H., et al. (2017). GLEAM v3: satellite-based land evaporation and root-zone soil moisture. Geoscientific Model Development, 10(5), 1903-1925. https://doi.org/10.5194/gmd-10-1903-2017

Matheny, A. M., Bohrer, G., Garrity, S. R., Morin, T. H., Howard, C. J., & Vogel, C. S. (2015). Observations of stem water storage in trees of opposing hydraulic strategies. Ecosphere, 6(9), 1–13. http://doi.org/10.1890/ES15-00170.1

Matheny, A. M., Bohrer, G., Stoy, P. C., Baker, I. T., et al. (2014a). Characterizing the diurnal patterns of errors in the prediction of evapotranspiration by several land-surface models: An NACP analysis, Journal of Geophysical Research: Biogeosciences, 119(7), 1458–1473. http://doi.org/10.1002/2014JG002623

Matheny, A. M., Bohrer, G., Vogel, C. S., et al. (2014b). Species-specific transpiration responses to intermediate disturbance in a northern hardwood forest. Journal of Geophysical Research, 119, 2292–2311. http://doi.org/10.1002/2014JG002804

Matheny, A. M., Fiorella, R. P., Bohrer, G., et al. (2016). Contrasting strategies of hydraulic control in two codominant temperate tree species. Ecohydrology, 10(3), e1815. https://doi.org/10.1002/eco.1815

Matheny, A. M., Fiorella, R. P., Bohrer, G., et al. (2017a). Contrasting strategies of hydraulic control in two codominant temperate tree species. Ecohydrology, 10(3), e1815. https://doi.org/10.1002/eco.1815

Matheny, A. M., G. Mirfenderesgi, & G. Bohrer. (2017b). Trait-based representation of hydrological functional properties of plants in weather and ecosystem models, Plant Diversity, 39(1), 1–12. http://doi.org/10.1016/j.pld.2016.10.001

Matthes, J. H., Goring, S., Williams, J. W., & Dietze, M. C. (2016). Benchmarking historical CMIP5 plant functional types across the Upper Midwest and Northeastern United States. Journal of Geophysical Research: Biogeosciences, 121(2), 523-535. https://doi.org/10.1002/2015JG003175

McCulloh, K., Sperry, J. & Adler, F. (2003). Water transport in plants obeys Murray's law. Nature 421, 939–942. https://doi.org/10.1038/nature01444

McCulloh, K. A., J.-C. Domec, D. M. Johnson, D. D. Smith, & F. C. Meinzer (2019), A dynamic yet vulnerable pipeline: Integration and coordination of hydraulic traits across whole plants, Plant, Cell & Environment, 42(10), 2789–2807. http://doi.org/10.1111/pce.13607

McDonald, E. P., Erickson, J. E., & Kruger, E. L. (2002). Research note: Can decreased transpiration limit plant nitrogen acquisition in elevated CO2? Functional Plant Biology, 29(9), 1115-1120. https://doi.org/10.1071/FP02007

McDowell, N. G., Brodribb, T. J., & Nardini, A. (2019). Hydraulics in the 21st century, New Phytologist, 224(2), 537–542. http://doi.org/10.1111/nph.16151

McDowell, N., Pockman, W. T., Allen, C. D., et al. (2008). Mechanisms of plant survival and mor- tality during drought: Why do some plants survive while others succumb to drought? The New Phytologist, 178, 719–739. http://doi.org/10.1111/j.1469-8137.2008.02436.x

Meinzer, F. C., James, S. A., Goldstein, G., & Woodruff, D. (2003). Whole-tree water transport scales with sapwood capacitance in tropical forest canopy trees. Plant,

Cell & Environment, 26(7), 1147-1155. https://doi.org/10.1046/j.1365-3040.2003.01039.x

Mirfenderesgi, G., G. Bohrer, A. M. Matheny, et al. (2016). Tree level hydrodynamic approach for resolving aboveground water storage and stomatal conductance and modeling the effects of tree hydraulic strategy, Journal of Geophysical Research: Biogeosciences, 121(7), 1792–1813, doi:10.1002/2016JG003467

Mencuccini, M., Manzoni, S., & Christoffersen, B. (2019). Modelling water fluxes in plants: from tissues to biosphere, New Phytologist, 8, 367. http://doi.org/10.1111/nph.15681

Mirfenderesgi, G., Matheny, A. M., & Bohrer, G. (2019). Hydrodynamic trait coordination and cost–benefit trade-offs throughout the isohydric–anisohydric continuum in trees, Ecohydrology, 12(1), e2041. http://doi.org/10.1002/eco.2041

Mitchell, K. E., Lohmann, D., Houser, P. R., et al. (2004). The multi-institution North American Land Data Assimilation System (NLDAS): Utilizing multiple GCIP products and partners in a continental distributed hydrological modeling system. Journal of Geophysical Research: Atmospheres, 109(D7). https://doi.org/10.1029/2003JD003823

Mitchell, P. J., Veneklaas, E. J., Lambers, H., & Burgess, S. S. (2008). Using multiple trait associations to define hydraulic functional types in plant communities of south-western Australia. Oecologia, 158(3), 385-397. https://doi.org/10.1007/s00442-008-1152-5

Moreno-Martínez, Á., Camps-Valls, G., Kattge, J., et al. (2018). A methodology to derive global maps of leaf traits using remote sensing and climate data. Remote sensing of environment, 218, 69-88. https://doi.org/10.1016/j.rse.2018.09.006

Mrad, A., Domec, J. C., Huang, C. W., Lens, F., & Katul, G. (2018). A network model links wood anatomy to xylem tissue hydraulic behaviour and vulnerability to cavitation. Plant, cell & environment, 41(12), 2718-2730. http://doi.org/10.1111/pce.13415

Nemani, R.R., Keeling, C.D., Hashimoto, H., et al. (2003). Climate-driven increases in global terrestrial net primary production from 1982 to 1999. Science, 300(5625), 1560-1563. https://doi.org/10.1126/science.1082750

Niu, G.-Y., Yang, Z.-Y., et al. (2011). The community Noah land surface model with multiparameterization options (Noah-MP): 1. Model description and evaluation with local-scale measurements, Journal of Geophysical Research: Atmospheres, 116(D12), D12109. http://doi.org/10.1029/2010JD015139

Novick, K. A., Ficklin, D. L., Stoy, P. C., Williams, C. A., et al. (2016). The increasing importance of atmospheric demand for ecosystem water and carbon fluxes. Nature climate change, 6(11), 1023-1027. https://doi.org/10.1038/nclimate3114

Oleson, K., Dai, Y., Bonan, G. B., Bosilovichm, M., et al. (2004). Technical Description of the Community Land Model (CLM) (No. NCAR/TN-461+STR). University Corporation for Atmospheric Research. https://doi.org/10.5065/D6N877R0

Oren, R., Sperry, J. S., Katul, G. G., et al. (1999). Survey and synthesis of intra-and interspecific variation in stomatal sensitivity to vapour pressure deficit. Plant, Cell & Environment, 22(12), 1515-1526. https://doi.org/10.1046/j.1365-3040.1999.00513.x

Pappas, C., Fatichi, S., & P. Burlando (2016). Modeling terrestrial carbon and water dynamics across climatic gradients: does plant trait diversity matter? New Phytologist, 209(1), 137–151, http://doi.org/10.1111/nph.13590

Pavlick, R., Drewry, D. T., Bohn, K., Reu, B., & Kleidon, A. (2013). The Jena Diversity-Dynamic Global Vegetation Model (JeDi-DGVM): a diverse approach to representing terrestrial biogeography and biogeochemistry based on plant functional trade-offs. Biogeosciences, 10, 4137-4177. http://hdl.handle.net/11858/00-001M-0000-0013-F551-6

Piao, S. et al. (2014). Evidence for a weakening relationship between interannual temperature variability and northern vegetation activity, Nature Communications, 5, 5018. https://doi.org/10.1038/ncomms6018.

Piao, S., Wang, X., Wang, K., et al. (2020). Interannual variation of terrestrial carbon cycle: Issues and perspectives, Global Change Biology, 26(1), 300–318. https://doi.org/10.1111/gcb.14884.

Pinzon, J., & Tucker, C. (2014). A Non-Stationary 1981–2012 AVHRR NDVI3 g Time Series. Remote Sensing, 6, 6929–6960. https://doi.org/10.3390/rs6086929

Pockman, W. T., & Sperry, J. S. (2000). Vulnerability to xylem cavitation and the distribution of Sonoran desert vegetation. American Journal of Bot- any, 87, 1287–1299. http://doi.org/10.2307/2656722

Poulter, B., Ciais, P., Hodson, E., Lischke, H., et al. (2011). Plant functional type mapping for earth system models. Geoscientific Model Development, 4(4), 993-1010. https://doi.org/10.5194/gmd-4-993-2011

Poulter, B., Frank, D., Ciais, P., et al. (2014). Contribution of semi-arid ecosystems to interannual variability of the global carbon cycle. Nature, 509(7502), 600-603. https://doi.org/10.1038/nature13376

Powell, T.L., Galbraith, D.R., Christoffersen, B.O., et al. (2013). Confronting model predictions of carbon fluxes with measurements of Amazon forests subjected to experimental drought. New Phytologist, 200(2), pp.350-365. http://doi.org/10.1111/nph.12390

Rawson, H. M., Begg, J. E., & Woodward, R. G. (1977). The effect of atmospheric humidity on photosynthesis, transpiration and water use efficiency of leaves of several plant species. Planta, 134(1), 5-10. https://doi.org/10.1007/BF00390086

Reichstein, M., Bahn, M., Mahecha, M. D., Kattge, J., & Baldocchi, D. D. (2014). Linking plant and ecosystem functional biogeography. Proceedings of the National Academy of Sciences, 111(38), 13697-13702. https://doi.org/10.1073/pnas.1216065111

Reid, D. E., Silins, U., Mendoza, C., & Lieffers, V. J. (2005). A unified nomenclature for quantification and description of water conducting properties of sapwood xylem based on Darcy's law. Tree physiology, 25(8), 993-1000. https://doi.org/10.1093/treephys/25.8.993

Richardson, A. D., Hufkens, K., Milliman, T., et al. (2018). Ecosystem warming extends vegetation activity but heightens vulnerability to cold temperatures. Nature, 560(7718), 368-371. https://doi.org/10.1038/s41586-018-0399-1

Rigden, A. J., Mueller, N. D., et al. (2020). Combined influence of soil moisture and atmospheric evaporative demand is important for accurately predicting US maize yields, Nat Food, 1(2), 127–133. https://doi.org/10.1038/s43016-020-0028-7.

Roderick, M. L., & Berry, S. L. (2001). Linking wood density with tree growth and environment: a theoretical analysis based on the motion of water. New Phytologist, 149(3), 473-485. http://doi.org/10.1046/j.1469-8137.2001.00054.x

Running, S. W., Loveland, T. R., & Pierce, L. L. (1994). A vegetation classification logic-based on remote-sensing for use in global biogeochemical models. Ambio, 23(1), 77-81.

Ryel, R., Caldwell, M., Yoder, C., Or, D., & Leffler, A. (2002). Hydraulic redistribution in a stand of Artemisia tridentata: evaluation of benefits to transpiration assessed with a simulation model. Oecologia, 130(2), 173-184. https://doi.org/10.1007/s004420100794

Sabot, M. E. B., M. G. De Kauwe, A. J. Pitman, B. E. Medlyn, A. Verhoef, A. M. Ukkola, and G. Abramowitz. (2020). Plant profit maximization improves predictions of European forest responses to drought, New Phytol., 226(6), 1638–1655. https://doi.org/10.1111/nph.16376

Savage, V. M., Deeds, E. J., & Fontana, W. (2008), Sizing Up Allometric Scaling Theory, edited by B. J. Enquist, PLOS Computational Biology, 4(9), e1000171. http://doi.org/10.1371/journal.pcbi.1000171

Savage, V. M., Bentley, L. P., Enquist, B. J., et al. (2010). Hydraulic trade-offs and space filling enable better predictions of vascular structure and function in plants. Proceedings of the National Academy of Sciences, 107(52), 22722-22727. https://doi.org/10.1073/pnas.1012194108

Save, H., Bettadpur, S., & Tapley, B. D. (2016). High-resolution CSR GRACE RL05 mascons. Journal of Geophysical Research: Solid Earth, 121(10), 7547–7569. http://doi.org/10.1002/2016JB013007

Saxton, K. E., Rawls, W., Romberger, J. S., & Papendick, R. I. (1986). Estimating generalized soil-water characteristics from texture 1. Soil science society of America Journal, 50(4), 1031-1036. https://doi.org/10.2136/sssaj1986.03615995005000040039x

Scanlon, B. R., Zhang, Z., Reedy, R. C., Pool, D. R., Save, H., Di Long, et al. (2015). Hydrologic implications of GRACE satellite data in the Colorado River Basin. Water Resources Research, 51(12), 9891–9903. http://doi.org/10.1002/2015WR018090

Scheiter, S., Langan, L., & Higgins, S. I. (2013). Next-generation dynamic global vegetation models: learning from community ecology. New Phytologist, 198(3), 957-969. https://doi.org/10.1111/nph.12210

Schlesinger, W. H., & Jasechko, S. (2014), Transpiration in the global water cycle, Agricultural and Forest Meteorology, 189-190, 115–117, doi:10.1016/j.agrformet.2014.01.011

Scholz, F. G., Bucci, S. J., Goldstein, G., et al. (2007). Removal of nutrient limitations by long-term fertilization decreases nocturnal water loss in savanna trees. Tree Physiology, 27(4), 551-559. https://doi.org/10.1093/treephys/27.4.551

Scholz, F. C., Bucci, S. J., Goldstein, G., et al. (2008). Temporal dynamics of stem expansion and contraction in savanna trees: withdrawal and recharge of stored water. Tree Physiology, 28(3), 469-480. https://doi.org/10.1093/treephys/28.3.469

Sellers, P. J., Mintz, Y. C. S. Y., Sud, Y. E. A., & Dalcher, A. (1986). A simple biosphere model (SiB) for use within general circulation models. Journal of the Atmospheric Sciences, 43(6), 505-531. https://doi.org/10.1175/1520-0469(1986)043<0505:ASBMFU>2.0.CO;2

Shevliakova, E., Stouffer, R. J., Malyshev, S., et al. (2013). Historical warming reduced due to enhanced land carbon uptake. Proceedings of the National Academy of Sciences, 110(42), 16730–16735. https://doi.org/10.1073/pnas.1314047110

Shiga, Y. P., Michalak, A. M., Fang, Y., et al. (2018). Forests dominate the interannual variability of the North American carbon sink. Environmental Research Letters, 13(8), 084015. https://doi.org/10.1088/1748-9326/aad505

Shinozaki, K., Yoda, K., Hozumi, K., & Kira, T. (1964a). A quantitative analysis of plant form-the pipe model theory: I. Basic analyses. Japanese Journal of ecology, 14(3), 97-105. https://doi.org/10.18960/seitai.14.3_97

Shinozaki K, Yoda K, Hozumi K, Kira T. (1964b). A quantitative analysis of plant form–the pipe model theory. II. Further evidence of the theory and its application in forest

ecology. Japanese Journal of Ecology 14: 133–139. https://doi.org/10.18960/seitai.14.4_133

Simard, M., N. Pinto, J. B. Fisher, and A. Baccini (2011), Mapping forest canopy height globally with spaceborne lidar, Journal of Geophysical Research: Biogeosciences, 116(G4), G04021, doi:10.1029/2011JG001708

Sitch, S., Friedlingstein, P., Gruber, N., Jones, S.D., et al. (2015). Recent trends and drivers of regional sources and sinks of carbon dioxide. Biogeosciences, 12(3), pp.653-679. http://doi.org/10.5194/bg-12- 653-2015

Skamarock, W. C., Klemp, J. B., Dudhia, J., et al (2019). A Description of the Advanced Research WRF Model Version 4 (No. NCAR/TN-556+STR). http://doi.org/10.5065/1dfh-6p97

Skelton, R. P., West, A. G., & Dawson, T. E. (2015). Predicting plant vulner- ability to drought in biodiverse regions using functional traits. Proceedings of the National Academy of Sciences, 112, 5744–5749. http://doi.org/10.1073/pnas.1503376112

Snyder, K. A., Richards, J. H., & Donovan, L. A. (2003). Night-time conductance in C3 and C4 species: do plants lose water at night? Journal of Experimental Botany, 54(383), 861-865. https://doi.org/10.1093/jxb/erg082

Spawn, S.A., Sullivan, C.C., Lark, T.J., et al. (2020). Harmonized global maps of above and belowground biomass carbon density in the year 2010. Scientific Data, 7(1), 1-12. https://doi.org/10.1038/s41597-020-0444-4

Sperry, J. S., Adler, F. R., Campbell, G. S., & Comstock, J. P. (1998). Limitation of plant water use by rhizosphere and xylem conductance: results from a model. Plant, Cell & Environment, 21(4), 347-359. https://doi.org/10.1046/j.1365-3040.1998.00287.x

Sperry, J. S. (2000). Hydraulic constraints on plant gas exchange. Agricultural and forest meteorology, 104(1), 13-23. https://doi.org/10.1016/S0168-1923(00)00144-1

Sperry, J. S., Stiller, V., & Hacke, U. G. (2003). Xylem hydraulics and the soil–plant–atmosphere continuum. Agronomy Journal, 95(6), 1362-1370. https://doi.org/10.2134/agronj2003.1362

Sperry, J. S., Wang, Y., Wolfe, B. T., et al. (2016). Pragmatic hydraulic theory predicts stomatal responses to climatic water deficits. New Phytologist, 212(3), 577-589. https://doi.org/10.1111/nph.14059

Sperry, J. S., Venturas, M. D., Anderegg, W. R., Mencuccini, M., et al. (2017). Predicting stomatal responses to the environment from the optimization of photosynthetic gain and hydraulic cost. Plant, cell & environment, 40(6), 816-830. https://doi.org/10.1111/pce.12852

Steppe, K., De Pauw, D. J., Lemeur, R., & Vanrolleghem, P. A. (2006). A mathematical model linking tree sap flow dynamics to daily stem diameter fluctuations and radial

stem growth. Tree physiology, 26(3), 257-273. https://doi.org/10.1093/treephys/26.3.257

Sulla-Menashe, D., & Friedl, M. A. (2018). User Guide to Collection 6 MODIS Land Cover (MCD12Q1 and MCD12C1) Product. USGS: Reston, VA, USA, 1-18

Thomsen, J., Bohrer, G., Matheny, A. M., Ivanov, V. Y., et al. (2013). Contrasting hydraulic strategies during dry soil conditions in Quercus rubra and Acer rubrum in a sandy site in Michigan. Forests, 4, 1106–1120. https://doi.org/10.3390/f4041106

Trugman, A. T., D. Medvigy, J. S. Mankin, and W. R. L. Anderegg. (2018). Soil Moisture Stress as a Major Driver of Carbon Cycle Uncertainty, Geophysical Research Letters, 45(13), 6495–6503. https://doi.org/10.1029/2018GL078131.

Trugman, A. T., L. Anderegg, D. L., Sperry, J. S., et al. (2019a). Leveraging plant hydraulics to yield predictive and dynamic plant leaf allocation in vegetation models with climate change, Global Change Biology, 25(12), 4008–4021. http://doi.org/10.1111/gcb.14814

Trugman, A. T., Anderegg, L. D., Wolfe, B. T., et al. (2019b). Climate and plant trait strategies determine tree carbon allocation to leaves and mediate future forest productivity. Global change biology, 25(10), 3395-3405. https://doi.org/10.1111/gcb.14680

Tuzet, A., Perrier, A., & Leuning, R. (2003). A coupled model of stomatal conductance, photosynthesis and transpiration. Plant, Cell & Environment, 26(7), 1097-1116. http://doi.org/10.1046/j.1365-3040.2003.01035.x

Tyree, M. T., & Sperry, J. S. (1989). Vulnerability of xylem to cavitation and embolism. Annual review of plant biology, 40(1), 19-36. https://doi.org/10.1146/annurev.pp.40.060189.000315

Ukkola, A. M., De Kauwe, M. G., Roderick, M. L., et al. (2020). Robust future changes in meteorological drought in CMIP6 projections despite uncertainty in precipitation. Geophysical Research Letters, e2020GL087820. https://doi.org/10.1029/2020GL087820

UNEP (United Nations Environment Programme). (1997). World atlas of desertification 2ED.

Van Bodegom, P. M., Douma, J. C., & Verheijen, L. M. (2014). A fully traits-based approach to modeling global vegetation distribution. Proceedings of the National Academy of Sciences, 111(38), 13733-13738. https://doi.org/10.1073/pnas.1304551110

Van Bodegom, P. M., Douma, J. C., Witte, J. P. M., et al. (2012). Going beyond limitations of plant functional types when predicting global ecosystem–atmosphere fluxes:

exploring the merits of traits-based approaches. Global Ecology and Biogeography, 21(6), 625-636. https://doi.org/10.1111/j.1466-8238.2011.00717.x

Verheijen, L. M., Brövkin, V., Aerts, R., Bonisch, G., et al. (2013). Impacts of trait variation through observed trait-climate relationships on performance of an Earth system model: a conceptual analysis. https://doi.org/10.5194/bg-10-5497-2013

Verhoef, A., & G. Egea (2014). Modeling plant transpiration under limited soil water: Comparison of different plant and soil hydraulic parameterizations and preliminary implications for their use in land surface models, Agricultural and Forest Meteorology, 191, 22–32. http://doi.org/10.1016/j.agrformet.2014.02.009

Verrelst, J., Muñoz, J., Alonso, L., et al. (2012). Machine learning regression algorithms for biophysical parameter retrieval: Opportunities for Sentinel-2 and-3. Remote Sensing of Environment, 118, 127-139. https://doi.org/10.1016/j.rse.2011.11.002

Wang-Erlandsson, L., Van Der Ent, R. J., Gordon, L. J., & Savenije, H. H. G. (2014). Contrasting roles of interception and transpiration in the hydrological cycle–Part 1: Temporal characteristics over land. Earth System Dynamics, 5(2), 441. https://doi.org/10.5194/esd-5-441-2014

Wang, H., Zhao, P., Wang, Q., Cai, X., Ma, L., Rao, X., & Zeng, X. (2008). Nocturnal sap flow characteristics and stem water recharge of Acacia mangium. Frontiers of Forestry in China, 3(1), 72-78. https://doi.org/10.1007/s11461-008-0005-z

Wang, H., Zhao, P., Hölscher, D., et al. (2012). Nighttime sap flow of Acacia mangium and its implications for nighttime transpiration and stem water storage. Journal of Plant Ecology, 5(3), 294-304. https://doi.org/10.1093/jpe/rtr025

Wang, J., Zeng, N., & Wang, M. (2016). Interannual variability of theatmospheric CO2 growth rate: roles of precipitation and temperature. Biogeosciences, 13(8), 2339–2352. https://doi.org/10.5194/bg-13-2339-2016

Wang, P., Niu, G. Y., Fang, Y. H., Wu, R. J., Yu, J. J., Yuan, G. F., et al. (2018b). Implementing Dynamic Root Optimization in Noah-MP for Simulating Phreatophytic Root Water Uptake. Water Resources Research, 54(3), 1560–1575. http://doi.org/10.1002/2017WR021061

Wang, X., Ciais, P., Wang, Y., et al. (2018a). Divergent response of seasonally dry tropical vegetation to climatic variations in dry and wet seasons. Global Change Biology, 24(10), 4709-4717. https://doi.org/10.1111/gcb.14335

Wang, X., Piao, S., Ciais, P., et al. (2014). A two-fold increase of carbon cycle sensitivity to tropical temperature variations. Nature, 506(7487), 212-215. https://doi.org/10.1038/nature12915

Wang, X., Wang, T., Liu, D., Guo, H., Huang, H., & Zhao, Y. (2017). Moisture-induced greening of the South Asia over the past three decades. Global Change Biology, 23(11), 4995–5005. http://doi.org/10.1111/gcb.13762

Wei, Z., Yoshimura, K., Wang, L., Miralles, D. G., Jasechko, S., & Lee, X. (2017). Revisiting the contribution of transpiration to global terrestrial evapotranspiration. Geophysical Research Letters, 44(6), 2792–2801. http://doi.org/10.1002/2016GL072235

West, G. B., Brown, J. H., & Enquist, B. J. (1999). A general model for the structure and allometry of plant vascular systems. Nature, 400(6745), 664-667. https://doi.org/10.1038/23251

Williams, A. P., Cook, E. R., Smerdon, J. E., et al. (2020). Large contribution from anthropogenic warming to an emerging North American megadrought. Science, 368(6488), 314-318. https://doi.org/10.1126/science.aaz9600

Williams, M., Rastetter, E. B., Fernandes, D. N., et al. (1996). Modelling the soil-plant-atmosphere continuum in a Quercus–Acer stand at Harvard Forest: the regulation of stomatal conductance by light, nitrogen and soil/plant hydraulic properties. Plant, Cell & Environment, 19(8), 911-927. https://doi.org/10.1111/j.1365-3040.1996.tb00456.x

Wright, I. J., Reich, P. B., Cornelissen, J. H., et al. (2005). Assessing the generality of global leaf trait relationships. New phytologist, 166(2), 485-496. https://doi.org/10.1111/j.1469-8137.2005.01349.x

Wullschleger, S.D., Epstein, H.E., Box, E.O., et al. (2014). Plant functional types in Earth system models: past experiences and future directions for application of dynamic vegetation models in high-latitude ecosystems. Annals of botany, 114(1), 1-16. https://doi.org/10.1093/aob/mcu077

Xia, Y., Mitchell, K., Ek, M., Sheffield, J., et al. (2012). Continental-scale water and energy flux analysis and validation for the North American Land Data Assimilation System project phase 2 (NLDAS-2): 1. Intercomparison and application of model products. Journal of Geophysical Research: Atmospheres, 117(D3). https://doi.org/10.1029/2011JD016048

Xu, X., Medvigy, D., Powers, J. S., et al. (2016). Diversity in plant hydraulic traits explains seasonal and inter-annual variations of vegetation dynamics in seasonally dry tropical forests. New Phytologist, 212(1), 80-95. https://doi.org/10.1111/nph.14009

Xue, Y., Sellers, P. J., Kinter, J. L., & Shukla, J. (1991). A simplified biosphere model for global climate studies. Journal of Climate, 4(3), 345-364. https://doi.org/10.1175/1520-0442(1991)004<0345:ASBMFG>2.0.CO;2

Yan, B., Mao, J., Dickinson, R. E., Thornton, P. E., Shi, X., Ricciuto, D. M., et al. (2020). Modelling tree stem-water dynamics over an Amazonian rainforest. Ecohydrology, 13(1). http://doi.org/10.1002/eco.2180

Yang, Y., Zhu, Q., Peng, C., Wang, H., & Chen, H. (2015). From plant functional types to plant functional traits: A new paradigm in modelling global vegetation dynamics.

Progress in Physical Geography, 39(4), 514-535. https://doi.org/10.1177%2F0309133315582018

Yang, Z.-L., & Dickinson, R. E. (1996). Description of the Biosphere-Atmosphere Transfer Scheme (BATS) for the Soil Moisture Workshop and evaluation of its performance. Global and Planetary Change, 13(1-4), 117-134. https://doi.org/10.1016/0921-8181(95)00041-0

Yang, Z.-L., Niu, G.-Y., Mitchell, K. E., et al. (2011), The community Noah land surface model with multiparameterization options (Noah-MP): 2. Evaluation over global river basins, Journal of Geophysical Research: Atmospheres, 116(D12), D12110. http://doi.org/10.1029/2010JD015140

Yuan, H., Dai, Y., Xiao, Z., Ji, D., & Shangguan, W. (2011). Reprocessing the MODIS Leaf Area Index products for land surface and climate modelling. Remote Sensing of Environment, 115(5), 1171-1187. http:/doi.org/10.1016/j.rse.2011.01.001

Yuan, W., Zheng, Y., Piao, S., et al. (2019). Increased atmospheric vapor pressure deficit reduces global vegetation growth. Science advances, 5(8), eaax1396. https://doi.org/10.1126/sciadv.aax1396

Zeng, N., Mariotti, A., & Wetzel, P. (2005). Terrestrial mechanisms of interannual CO2 variability. Global Biogeochemical Cycles, 19(1). https://doi.org/10.1029/2004GB002273

Zhang, Y., Commane, R., Zhou, S., et al. (2020). Light limitation regulates the response of autumn terrestrial carbon uptake to warming. Nature Climate Change, 1-5. https://doi.org/10.1038/s41558-020-0806-0

Zhao, X., Zhao, P., Zhang, Z., et al. (2017). Culm age and rhizome affects night-time water recharge in the bamboo Phyllostachys pubescens. Frontiers in plant science, 8, 1928. https://doi.org/10.3389/fpls.2017.01928

Zheng, H., Yang, Z. L., Lin, P., et al. (2019). On the sensitivity of the precipitation partitioning into evapotranspiration and runoff in land surface parameterizations. Water Resources Research, 55(1), 95-111. https://doi.org/10.1029/2017WR022236

Zhou, S., Yu, B., Zhang, Y., Huang, Y., & Wang, G. (2016). Partitioning evapotranspiration based on the concept of underlying water use efficiency. Water Resources Research, 52(2), 1160–1175. http://doi.org/10.1002/2015WR017766

Zhu, S. D., Chen, Y. J., & Cao, K. F. (2018). Leaf turgor loss point is correlated with drought tolerance and leaf carbon economics traits. Tree physiology, 38(5), 658-663. https://doi.org/10.1093/treephys/tpy013

Zhuang, J., Yu, G. R., & Nakayama, K. (2014). A Series RCL Circuit Theory for Analyzing Non-Steady-State Water Uptake of Maize Plants, Sci Rep, 4(1), 482. https://doi.org/10.1038/srep06720

Vita

Lingcheng Li was born in Hunan Province, China. After finishing high school in 2008, he entered Wuhan University with one of the most beautiful campuses in China. He had a seven-year wonderful life at Wuhan University, where he earned his B.Eng. in Hydrology and Water Resources Engineering in 2012 and his M.Sc. in Hydrology and Water Resources in 2015. With tremendous encouragement and support from his family, he then joined the Jackson School of Geological Sciences at The University of Texas at Austin to pursue a Ph.D. degree during 2015 – 2020.

Permanent email: lingchengliwhu@gmail.com.

This dissertation was typed by Lingcheng Li.